From peak to planet: advancing multi-scale detection of snowmelt timing with satellite radar

Eric Gagliano

A dissertation

submitted in partial fulfillment of the

requirements for the degree of

Doctor of Philosophy

University of Washington

2025

Reading Committee:

David Shean, Chair

Scott Henderson

Jessica Lundquist

Program Authorized to Offer Degree:

Civil & Environmental Engineering

University of Washington

Abstract

From peak to planet: advancing multi-scale detection of snowmelt timing with satellite radar

Eric Gagliano

Chair of the Supervisory Committee:
David Shean
Department of Civil & Environmental Engineering

Snowmelt runoff onset represents a critical parameter in mountain hydrology, marking the beginning of increased water availability for over a billion people who depend on seasonal snowmelt, as well as being a key indicator of climate change. Despite its importance, systematic high-resolution observations of snowmelt timing across the Earth's diverse mountain regions are limited with current monitoring approaches: sparse in-situ networks, cloud-obscured optical remote sensing, and coarse passive microwave observations.

This dissertation advances the detection of snowmelt runoff onset from local to global scales using Synthetic Aperture Radar (SAR) observations from the European Space Agency Sentinel-1 mission. SAR overcomes key limitations of other snow monitoring approaches through its ability

to observe through clouds and in darkness, high spatial resolution, and sensitivity to liquid water content changes in snowpack that coincide with snowmelt runoff onset.

Chapter 2 establishes the methodological foundation of this work by demonstrating scalable detection of snowmelt runoff onset using Sentinel-1 backscatter time-series analysis over stratovolcanoes in the Cascade Range of North America. By integrating multiple orbital geometries, the approach achieves a median temporal resolution of 3.9 days at 10-meter spatial resolution. Validation with in-situ snow pillow measurements shows a median offset of 1 day and median absolute offset of 10 days for the SAR snowmelt runoff onset timing estimates. Analysis across elevation gradients reveals strong topographic control, with median delays of 4.9 days per 100 meter elevation gain, as well as dramatic interannual variability including 25-day early runoff onset during the 2015 snow drought.

Chapter 3 scales this methodology, processing over 3.9 million Sentinel-1 images to create a global snowmelt runoff onset dataset spanning the 10-year period from 2015 through 2024. To enable robust detection of snowmelt runoff onset across diverse environments, we develop a custom MODIS-derived snow phenology dataset that provides spatial and temporal constraints for runoff onset identification. Systematic analysis establishes empirically-derived recommendations for snowmelt runoff onset dataset application based on forest cover, snow accumulation, and observation frequency. Validation against runoff onset estimates from over 900 in-situ snow pillows across the Western U.S. demonstrates robust dataset performance across different mountain environments. This dataset provides an unprecedented look at annual snowmelt runoff onset on a global scale, with 80-meter spatial resolution and 9.3-day average temporal resolution.

Chapter 4 presents the first comprehensive global analysis of snowmelt timing patterns and controls across 150 major mountain ranges. Continental-scale analysis reveals systemic weakening

of elevation gradients from mid-latitudes toward polar regions, as well as snowmelt runoff onset timing differences between sunny and shaded areas that varies seasonally but reaches maximum values of 20-60 days around early- to mid-spring. Mountain range-scale aggregation reveals a median runoff onset delay of 3.5 days per 100 meters of elevation gain, but with substantial variability, reflecting differences in climate, topography, and snowpack characteristics. Individual mountain ranges show variable aspect differences in runoff onset timing depending on local climate and topography, with some clear-sky continental ranges exhibiting differences exceeding 40 days while nearby cloudier ranges show minimal aspect differences. The tropical Andes and Tibetan Plateau mountain ranges display the highest interannual variability of snowmelt runoff onset timing, often exceeding 30 days. Temperature sensitivity analysis reveals that 72% of mountain ranges show correlations between spring (March-May) temperature anomaly and runoff onset timing, with most mid-latitude mountain ranges exhibiting runoff onset 8 to 13 days early for every 1°C warmer spring average temperature.

Chapter 5 synthesizes these findings and examines implications for water-dependent populations through basin-scale analysis in High-Mountain Asia and western North America. The analysis reveals coherent regional patterns in snowmelt runoff onset during documented anomalous weather events, including the 2015 western North American “snow drought” and 2022 High-Mountain Asia “mega-heatwave”, demonstrating how synoptic-scale weather events can produce spatially coherent 20-40 day shifts in snowmelt runoff onset timing across entire regions. Preliminary vulnerability assessment identifies high-population basins with high interannual variability in snowmelt runoff onset timing, with implications for water security.

This dissertation establishes the first systematic framework for observing snowmelt runoff onset at high resolution across global mountain regions. The decade-long record provides

unprecedented detail of snowmelt timing patterns, quantifies fundamental physical controls operating across diverse environments, and documents substantial interannual variability linked to average spring air temperature. The methodology, open-source tools, and open datasets from this dissertation will enable improved understanding of snow hydrology and support more effective water resource management in an era of increasing environmental change.

TABLE OF CONTENTS

LIST OF FIGURES

LIST OF TABLES

ACKNOWLEDGEMENTS

This work would not have been possible without the support, guidance, and friendship of many people. I would like to first acknowledge and thank my committee members: David Shean, Scott Henderson, Jessica Lundquist, H.P. Marshall, and Mia Bennett.

David brought me to UW and gave me the opportunity to work on exciting research with an amazing group of wonderful people. His academic rigor, background knowledge, and keen attention to detail have helped me become a more thorough scientist, and his support and flexibility made it easy to continue my research despite health challenges. I'm especially grateful for the teaching opportunities he provided, including allowing me to serve as the instructor of record for the Geospatial Data Analysis class for two quarters, an experience that important to my career goals.

Scott Henderson's support has been unwavering even through the toughest of times. Besides his friendliness and desire to help supercharge everyone else's work, Scott's deep expertise in cutting-edge geospatial workflows made my global-scale work possible. I am so lucky to have learned from and worked with someone who gives so generously his time and support. The progress of our research community is only possible because of people like Scott who dedicate themselves to lifting up the work of their peers.

Jessica Lundquist is probably the most knowledgeable person in snow hydrology I've ever met. Jessica's intuition for snow and physical processes is so impressive, and her curiosity and approach to problem solving have had a huge impact on how I approach snow research. It's been

an honor to learn from you. Beyond this, Jessica's encouragement through the most stressful parts of this PhD played a large role in me seeing it through to the end.

I've always admired H.P. Marshall for his deep knowledge of all things snow and radar, but also for his tireless work making the snow community what it is. H.P. recognizes the importance of community and inclusion, and he also "walks the walk", building our snow community brick by brick with intentionality and care. Importantly, H.P. does this all while never overlooking even the newest of newcomers. I am so thankful to have such a pillar of the community on my committee—I look up to H.P. in so many ways.

Mia Bennett's academic work I first appreciated from afar, but now I'm lucky enough to have learned from her through conversation and her time on my committee. Mia's application of critical theory to remote sensing and the cryosphere is something our field desperately needs. While many in our field pursue a seemingly "non-political" status quo, her research reminds us how political our work, tools, and methodologies truly are, which forces us to engage with our own positionality and responsibilities within systems of power. I'm grateful to Mia for being on my committee and for expanding how I think about the context of my work.

I am so lucky to have the members of the Terrain Analysis and Cryosphere Observation lab, both past and present, as such an important part of my academic and social support system. Michelle, Friedrich, Shashank, you made me feel at home as soon as I got to Seattle. Y'all made the lab environment collaborative and supportive instead of competitive, and y'all's friendship got me through it all. Y'all are my day ones. Thank y'all for everything you've done for me, you've each left a lasting impact on me in such special and unique ways. I'm looking forward to many more years of friendship. Seth, I am lucky we started together—it was such a joy getting to know you, work with you, and play intramural sports with you. This dissertation is heavily inspired by

our early work and conversations together, and I am so grateful for your academic support, humor, and friendship. Greg and Romain, y'all came in at the perfect time—your humor and expertise brought so much knowledge and much needed energy to our lab, and your support and friendship helped me power through some of the more difficult portions of the PhD. Alan, getting to work on the social media / website stuff with you was always so much fun, thank you for all the laughs. Karthik, the warmth and sincerity you brought to the lab was unmatched—thank you for being such a genuine beacon of light. Jack and Ayush, I am so glad y'all joined—Quinn and I were starting to get lonely! Getting to know y'all, becoming good friends, and watching y'all tackle large research problems in such a short time has been a joy. I know y'all will carry on the tradition of making this lab a welcoming place. Last but not least, Quinn, getting to be the most senior in the lab together these past few years and finish our journeys together has been such a special experience. I'm glad we've spent more time together—I've learned so much from you, and I really admire the care you pour into everything you do.

The wonderful UW CEE folks, especially all of my friends in the treehouse and in the fishbowl, were essential to completing this PhD. Chatting with (bothering) y'all was always such a highlight of my day, I realize I was so lucky to be surrounded by such amazing (and silly) scientists and friends. Special thanks to the Mountain Hydrology lab, SASWE group, and AIMS lab for your friendship and for entertaining my endless distractions. Thank you to the CEE community for always humoring me by joining intramurals. Thank you to UAW 4121 for fighting for graduate students, to adi for inspiring me to become a steward, and to Alanna for stewarding with me!

The wider snow research community has become so important to me. Getting to spend time together at AGU, Western Snow Conference, SnowEx hackweeks, and more, I've come to really appreciate how special our community is. Our community thrives because of the folks that make

an intentional effort to include and uplift others, and I am so thankful for those in our community who exemplify this. Just to name a small fraction that have had an impact on me—Carrie Vuyovich, H.P. Marshall, Michelle Hu, Megan Mason, Bareerah Mirza, Anthony Arendt, Charley Haley, Emma Marshall, Joe Meyer, Hannah Besso, Dylan Boyd, Mark Raleigh, Nicoleta Cristea, Steven Pestana, and Naomi Alterman.

Thank you to all of the friends who I've gotten to collaborate with on SAR snowmelt research, like Mira Khadka, Lila Rickenbaugh, Seth Vanderwilt, Smriti Srivastava, Ally Detre, Preetika Kaur, Avina Khatri, Mary O'Flaherty, Marin MacDonald, Kyla Christopher-Moody, Bareerah Mirza, and Ross Mower. Y'all's input and advice have heavily shaped this dissertation.

I am deeply grateful to my mentors back at UT Austin who've helped to get me to where I am now—Ann Chen, Scott Staniewicz, Ginny Catania, and Sophie Goliber.

To my friends back home (and those now scattered to the winds!), knowing y'all were rooting for me from afar made the more overwhelming days a bit easier to bear.

So much love to the multitudes of peer role models I've been lucky enough to have in my life. Michelle Hu, Parisa Mahmud, Richard Mathison, Evin George, Kristine Chen, Max Gray, Shashank Bhushan, Jaymie Gagliano, just to name a few. Thank you for inspiring me.

Thank you to my diabetes doctors and the Benaroya research team, your care and expertise made this silly mid-PhD T1D diagnosis manageable.

Special shoutout to UW Concert Chorale and the UW Gospel Choir—making music with y'all sustained me throughout the PhD.

My Camp Kesem family, both at UT Austin and now here at UW, has shaped who I am in profound ways. Being a counselor has been transformative, and knowing that I am loved and

supported by y'all grounded me. Thank you especially to my campers—it has been one of the greatest honors of my life to watch y'all grow to care for and love each other so deeply.

To all the (f)roommates I've had here in Seattle—coming home to y'all's warmth, humor, and care after a long day in the office always lifted my spirits. And more broadly, thank you to all of the wonderful friends I've made on this journey! I love y'all so much. Thank you for all your support through the ups and downs of this silly adventure. We are friends forever now, no takebacks, sorry!

Finally, to my amazing family—Mom, Dad, and Jaymie. I cannot describe in words how thankful I am for all of your constant support, from childhood to now. Just know I am only here because of y'all's love and encouragement. Thank you to Garfield for 17 wonderful years of love. Thank you to both Little Cat and Maizy for keeping us all comforted and sane. Thank you to my extended family—Aunt Janice, Uncle Marty, Joanna, Sam, Uncle Gerry, Aunt Barbara, Gerard, Kara, Aunt Jane, Uncle Wally, Lindsy, Paige, Aunt Beth, Uncle Gregg, Gillian, Aunt Ellen, Uncle Doug, Aunt Myra, Mrs. Vanessa, Mr. Jeremy, Kaeman, Ryan, and Clay. Thank you to Uncle Eddie, Uncle Steve, Aunt Ruthie, Aunt Pearlie, and Nana, we all miss you very much. Thank you to grandma and grandpa—I am who I am because of you. Your memory inspires me every day. No matter where I go, y'all will always be in my heart.

DEDICATION

To my grandma and grandpa,

who taught me curiosity, service, and love

And to the people of Palestine,

whose liberation is bound with our own

Chapter 1. INTRODUCTION

1.1 MOTIVATION

1.1.1 *Seasonal snow and the global water cycle*

Seasonal snow plays a crucial role in the Earth system. More than a billion people rely on meltwater from seasonal snow and glaciers for agriculture, hydropower, and municipal use (Barnett et al., 2005; Immerzeel et al., 2020). This dependence is particularly pronounced in mountain regions where seasonal snowpacks function as natural reservoirs, storing water as snow during the winter and gradually releasing it during spring and summer. In this way, mountain regions serve as natural water towers: higher elevations receive enhanced snowfall through orographic lift and cold temperatures preserve the snowpack until spring conditions trigger melt. Snowmelt runoff onset—when liquid water begins to leave the snowpack—marks the beginning of increased water availability, initiating the annual hydrologic pulse that sustains downstream ecosystems and human water needs (Dingman, 2015). Knowledge of when and where snowmelt occurs enables accurate streamflow predictions essential for flood forecasting, reservoir operations, agricultural planning, and municipal water supply management (Lundquist & Dettinger, 2005).

1.1.2 *Snowmelt timing as a climate change indicator*

Snowmelt timing serves as a sensitive indicator of regional climate change (Dudley et al., 2017). As a process highly responsive to temperature and precipitation, shifts in snowmelt patterns provide tangible evidence of changing climate conditions. Recent decades have shown significant impacts on global snowmelt patterns (Ismail et al., 2023; Royer et al., 2021; T. Yang et al., 2022).

Satellite observations from 1979-2018 found northern hemisphere melt onset occurring 4 days earlier per decade (Zheng et al., 2022). In the western U.S., peak snow water equivalent timing shifted 7 days earlier between 1982 and 2023 (Evan, 2019; US EPA, 2021). Projections suggest snowmelt timing in the western U.S. will shift earlier by up to one month by 2050 (Barnett et al., 2005; Stewart, 2009).

These trends, however, are neither uniform nor simple. Regional patterns vary substantially with latitude, elevation, and climate. In western North America, trends toward more frequent winter melt occurred most often at middle to high elevations (Musselman et al., 2021). In Kyrgyzstan, earlier snowmelt occurred primarily below 3400 m with a strong longitudinal gradient (Tomaszewska & Henebry, 2018).

The implications extend beyond timing shifts--changes in western U.S. snowmelt timing will lead to snowpack loss equivalent of a 25% decrease in streamflow from snowmelt by 2050 (Siirila-Woodburn et al., 2021). As snowmelt magnitudes decrease and timing shifts earlier, populations dependent on mountain snowmelt face increasing vulnerability to water shortages, particular during peak summer demand (Livneh & Badger, 2020).

1.1.3 *The need for systematic global observations*

Despite its importance, our understanding of the global spatial and temporal variability of snowmelt remains limited by observational constraints. Most studies focus on individual mountain ranges using diverse data sources and methodologies that prevent systematic comparison. While valuable locally, these region-specific studies cannot answer fundamental interregional questions about how snowmelt timing and its controls vary across the Earth. This observational gap limits water resource management in data-scare regions, limits our understanding of comparative mountain hydrology, and impedes anticipation to water security threats.

1.2 BACKGROUND

1.2.1 *Snowmelt processes and timing controls*

Snowmelt proceeds through three phases: warming (bringing the snowpack to 0°C), ripening (providing latent heat for phase change), and output (sustained water release). This transition to sustained output represents snowmelt runoff onset, though cycles of melt and refreeze complicate this progression (DeBeer & Pomeroy, 2017).

Snowmelt timing is determined by the energy balance at the snow surface through radiative fluxes (solar and longwave) and turbulent fluxes (sensible and latent heat) (Male & Granger, 1981; Marks & Dozier, 1992). The relative importance of these components varies with geography, topography, meteorology, and snowpack properties, creating substantial spatial and interannual variability in snowmelt timing (Kattelmann & Dozier, 1999; Mote, 2006).

Spatial controls operate across multiple scales. Latitude influences temperature, hours of sunlight, and sun angle (Pohl et al., 2006). Regional climate represents typical meteorological conditions modulating melt energy (Lisi et al., 2015). Topography exerts strong control through elevation-dependent temperature gradients and differential solar radiation on different slopes and aspects (Garnier & Ohmura, 1968; Lundquist & Flint, 2006). Forest cover can intercept falling snow and modifies the energy balance through reduced solar radiation, increased longwave radiation, and decreased wind speeds, with complex climate-dependent effects on melt timing (Lundquist et al., 2013; Varhola et al., 2010).

Interannual variability in snowmelt timing is driven by synoptic-scale winter and spring weather (Stewart, 2009; Zhang et al., 1996). Winter weather patterns shape antecedent snowpack properties that influence spring melt response (Warren, 1982; Yamaguchi et al., 2004). Spring weather patterns, particularly warm air mass advection, can substantially accelerate melt and overwhelm geographic controls (Cayan et al., 1993; Lundquist et al., 2004). Earlier melting snowpacks at lower latitude and elevations exhibit greater sensitivity to variable synoptic forcing, while later-melting high-elevation snowpacks show more consistent influence from annual solar cycles (Mioduszewski et al., 2015; Zhang et al., 2001).

1.2.2 *Traditional approaches to snowmelt monitoring*

In-situ measurements from snow courses and automated weather stations provide valuable point observations of snow properties. Networks like SNOTEL offer temporally dense measurements enabling detailed process characterization (Fleming et al., 2023). However, these networks are spatially sparse, typically concentrated at accessible mid-elevations, and under-sample high-elevation areas (Gleason et al., 2017). These point measurements cannot capture fine-scale spatial variability from local topography and vegetation, and many snow-dependent regions worldwide lack monitoring infrastructure.

Optical remote sensing maps snow cover using snow's distinct spectral characteristics. Multi-spectral instruments like MODIS provide global coverage at moderate resolution (~500 m) with daily revisit (Hall & Riggs, 2021). However, persistent cloud cover during spring melt significantly limits observations, especially in maritime mountain environments (Parajka & Blöschl, 2008). Additionally, optical sensors detect snow presence but cannot directly observe subsurface liquid warmer changes characterizing runoff onset.

Passive microwave remote sensing offers weather-independent observations by detecting natural microwave emissions. These sensors detect hemi-spheric scale melt timing through brightness temperature changes when snow becomes wet (Mioduszewski et al., 2015). However, coarse spatial resolution (typically ~25 km) cannot resolve mountain topography and associated snowmelt spatial variability.

1.2.3 *Synthetic aperture radar for snowmelt detection*

Synthetic aperture radar (SAR) overcomes key limitations of traditional approaches. SAR systems actively transmit microwave pulses and measure backscattered energy, enabling all-weather, day-or-night imaging at high resolution. Critically, SAR backscatter is highly sensitive to liquid water content due to dramatic changes in the dielectric properties of snow when water is present (Nagler et al., 2016).

When snow is dry, C-band radar penetrates the entire snowpack with backscatter dominated by the snow-ground interface. Liquid water dramatically increases absorption, limiting penetration to ~5-10 cm and causing substantial backscatter decrease. This produces a characteristic seasonal backscatter minimum coinciding with maximum liquid water content during ripening, followed by an increase in surface roughness evolves during runoff (Carletti et al., 2025).

Multiple studies validated that this backscatter minimum corresponds to runoff onset using in-situ snow pillow measurements (Darychuk et al., 2023; Gagliano et al., 2023; Gao & Ma, 2024; Marin et al., 2020), snow pit observations (Lund et al., 2022), and streamflow data (Gagliano et al., 2023; Lund et al., 2022).

The Sentinel-1 mission provides particularly valuable SAR data. Launched in 2014 (1A), 2016 (1B, failed 2021), and 2024 (1C), the constellation acquired C-band SAR imagery with 6-12 day revisit, global systematic coverage, and ~10-20 m resolution analysis (Bauer-Marschallinger et al., 2021). Sentinel-1 data is freely available as radiometrically terrain-corrected products suitable for time-series analysis (Small, 2011). This combination—weather independent observations, runoff onset sensitivity, frequent revisit, and long temporal record—make Sentinel-1 uniquely suited for systematic snowmelt monitoring.

1.3 RESEARCH OBJECTIVES AND DISSERTATION OVERVIEW

This dissertation develops and validates methodology for detecting snowmelt runoff onset using Sentinel-1 SAR, scales the approach to global coverage, and conducts the first high-resolution comprehensive analysis of snowmelt runoff onset patterns and controls across the Earth's mountain regions.

Chapter 2 establishes the methodological foundation through validation over Cascade Range stratovolcanoes. By integrating multiple Sentinel-1 orbits, our method improves temporal resolution and estimate robustness. Validation across snow pillows confirms accuracy, and systematic analysis quantifier topographic controls, documents interannual variability including the 2015 snow drought.

Chapter 3 improves and scales this methodology globally by processing ~3.9 million Sentinel-1 scenes to create a comprehensive dataset for water years 2015-2024. In doing so, we also develop a custom MODIS-derived snow phenology dataset providing spatial and temporal constraints for runoff onset detection. Systematic analysis establishes empirically derived recommendations for dataset application, based on forest cover, snow accumulation, and observation frequency. Validation against over 900 automatic weather stations in the western U.S. demonstrates accuracy. The dataset provides unprecedented global coverage at 80-meter resolution with 9.3 day average temporal resolution.

Chapter 4 presents the first comprehensive global analysis of snowmelt runoff onset across 150 major mountain ranges. Continental-scale analysis reveals systematic patterns in elevation, latitude, and aspect influence. Mountain range-scale quantification establishes how controls vary across different geographic and climactic settings. Interannual variability analysis identifies regions with consistent versus highly variable year-to-year runoff onset timing and documents regional anomalies during major weather events. Spring temperature sensitivity analysis quantifies empirical relationships between spring temperature and runoff onset, revealing systematic geographic patterns. These analyses demonstrate that snowmelt runoff onset timing displays broad spatially-coherent geographic controls but with important local nuances.

Chapter 5 synthesizes findings and examines implications for water-dependent populations through basin-scale analysis in High-Mountain Asia and western North America. Basin aggregation demonstrates how high-resolution patterns translate to water resource implications, and a preliminary vulnerability assessment identifies high-population basins with the greatest interannual variability and largest runoff onset timing anomaly. The chapter concludes with priorities for future research and applications.

This dissertation advances our ability to observe and understand snowmelt timing across global mountain regions, and we are excited to share this dataset, methodology, findings, and tools with the snow community to collectively advance our understanding of snowmelt timing.

Chapter 2. CAPTURING THE ONSET OF MOUNTAIN SNOWMELT RUNOFF USING SATELLITE SYNTHETIC APERTURE RADAR

This chapter has been published as: Gagliano, E., Shean, D., Henderson, S., & Vanderwilt, S. (2023). Capturing the onset of mountain snowmelt runoff using satellite synthetic aperture radar. *Geophysical Research Letters*, 50, e2023GL105303. **https://doi.org/10.1029/2023GL105303**

2.1 ABSTRACT

The timing of snowmelt runoff is critical for water resource applications, but its spatiotemporal evolution remains poorly understood. We present a scalable approach to map snowmelt runoff onset using Sentinel-1 SAR data for the past 8 years with 10 m spatial resolution and a median temporal resolution of 3.9 days. A systematic analysis of stratovolcanoes in the Western U.S. showed that snowmelt runoff onset is strongly dependent on elevation (r=0.81) with a median runoff onset lapse rate of 4.9 days per 100 m of elevation gain. During the 2015 snow drought, we observed snowmelt runoff onset 25 days early relative to the 2015-2022 median. We document a median shift in snowmelt runoff onset of +2.0 days later in the year per year between 2016 and 2022. Our open-source tools can be used to create snowmelt runoff onset maps anywhere on Earth.

2.2 INTRODUCTION

2.2.1 *Seasonal snow and snowmelt timing*

Seasonal snow plays an essential role in the Earth system and more than 1/6th of the world's population relies on seasonal snow and glaciers for agricultural and domestic water supply (Barnett

et al., 2005). For example, meltwater from snowpack in the Cascade Range of the Western United States (U.S.) provides 78% of the total annual average runoff to downstream rivers, lakes, and groundwater networks (Li et al., 2017). This water abundance is essential to the region's ecosystems and human populations, and understanding the timing of this meltwater release is critical for downstream water resource applications, groundwater storage, flood risk management, and ecosystem maintenance.

Additionally, snowmelt timing is an indicator of regional climate change (Dudley et al., 2017). For example, an observational study of weather stations in the Western U.S. found a trend towards earlier peak snow water equivalent (SWE) timing, which coincides with snowmelt runoff onset, with an average shift of 8 days earlier in the year between 1982 and 2021 (Evan, 2019; US EPA, 2021). Looking to the future, the snowmelt timing of the Western U.S. is projected to shift earlier in the year by up to one month by 2050 (Barnett et al., 2005; Stewart, 2009), with a corresponding snowpack loss equivalent to a 25% decrease in streamflow from snowmelt (Siirila-Woodburn et al., 2021). As snowmelt magnitude decreases and occurs earlier in the year, populations reliant on meltwater from snowpack may become more vulnerable to reduced water availability and droughts, especially during the summer months (Livneh & Badger, 2020).

Snowmelt runoff onset occurs after the moistening and ripening phases of snowmelt, when the snowpack is ripe and meltwater release begins (Dingman, 2015). This process is particularly important because it indicates the beginning of increased water availability and dictates the rate of spring flow (Ramage et al., 2006).

The spatiotemporal distribution of snowmelt runoff onset can be mapped with synthetic aperture radar (SAR). When the snow is dry, the SAR backscatter signal received is generally strong and dominated by surface scattering at the snow-ground interface. When the snow is wet, the backscatter signal is much weaker due to absorption by liquid water, and is dominated by surface scattering at the air-snow interface (Nagler et al., 2016; Shi & Dozier, 1995). Due to this high sensitivity of microwave radiation to liquid water in the snowpack, radar remote sensing has proven useful to delineate between different snowmelt phases (Marin et al., 2020).

Recent studies used SAR data from the Sentinel-1 mission to estimate snowmelt timing (Lund et al., 2022), glacier melt (Scher et al., 2021), and runoff onset (Darychuk et al., 2023; Marin et al., 2020) with validation from both simulated SWE and in-situ SWE from snow pits. Here, we improve upon these approaches by combining multiple viewing geometries from all available Sentinel-1 orbits and all available polarizations, and we use this improved approach to quantify snowmelt runoff onset for the Cascade stratovolcanoes for the period from 2015 to 2022.

2.2.2 *Study area: The Cascade Range*

The Cascade Range in the Pacific Northwest region of North America stretches from Lassen Peak in Northern California to Mount Lytton in Southern British Columbia. The climate of the Cascades is primarily maritime, characterized by moderate, dry summers and mild winters with high precipitation (Rasmussen & Tangborn, 1976). Due to orographic effects, the west side of the Cascade Range receives high annual precipitation and some of the highest annual snowfall in the U.S., including the world record for highest seasonal snowfall of ~29 m recorded at Mt. Baker during the 1998-99 season (Leffler et al., 2001). The climate of the Cascade Range is modulated by variations in sea surface temperatures due to both the El Niño Southern Oscillation (ENSO)

and the Pacific Decadal Oscillation (PDO) (Frans et al., 2018; Mantua et al., 1997). The snow in the Cascade Range is mostly classified as maritime snow on the west side of the range, and montane forest snow on the east side of the range (Sturm & Liston, 2021). Snowfall typically occurs from October to May, with the greatest snowfall occurring during December and January. Generally, snowmelt begins in March and April at most elevations in the Cascades, with snowmelt progressing to higher elevations in late summer.

In this study, we focus on the stratovolcanoes of the Cascade Range because they span a broad range of elevations, and their roughly conical shape enables systematic analysis of aspect and slope dependence. We highlight Mt. Rainier because it spans the largest elevation range and has the largest annual average snow accumulation. Consequently, we expect Mt. Rainier to have the greatest range of snowmelt runoff onset dates in the Cascade Range.

2.3 DATA

2.3.1 *Sentinel-1 RTC backscatter images*

The European Space Agency (ESA) Sentinel-1 mission consists of multiple C-band radar satellites in a near-polar, sun-synchronous orbit that each acquire high-resolution SAR images at ~06:00 and 18:00 local time with an orbital repeat period of 12 days, a swath width of 250 km, and a spatial resolution of 5x20 m in Interferometric Wide Swath mode. The Sentinel-1 mission began with the launch of Sentinel-1A in April 2014. Between April 2016 and December 2021, the Sentinel-1A and Sentinel-1B satellites offered a 6-day repeat interval from the same orbital plane. Sentinel-1B experienced a power issue in December 2021 and was decommissioned in August 2022, leaving only one operational satellite in the Sentinel-1 constellation until the planned launches of Sentinel-1C and 1D.

Many locations are covered by multiple overlapping scenes with different acquisition time and observational geometry for each relative orbit (Figure A.1), as well as different combinations of transmitted and received polarizations. We used all available Sentinel-1 Radiometrically Terrain Corrected (RTC) products from January 2015 to January 2023. These products have undergone multi-looking (5 looks in range direction, 1 look in azimuth direction), as well as radiometric and terrain correction (Small, 2011) using the 30 m PlanetDEM digital elevation model (Planet Observer, 2017), with final posting at 10 m (Catalyst & Microsoft, 2022). They are hosted as 32-bit cloud-optimized geotiffs on Microsoft Planetary Computer and publicly accessible through a STAC API (Microsoft Open Source et al., 2022).

2.3.2 *ESA Worldcover land cover*

The ESA WorldCover product (v100) is a global land cover classification map for the year 2020 with 11 classes, posted at 10 m (Zanaga et al., 2021). It is derived from combined Sentinel-1 SAR and Sentinel-2 multispectral data. We used this product to mask dense tree cover, which C-band radar cannot reliably penetrate.

2.3.3 *SNOTEL*

The SNOwpack TELemetry (SNOTEL) network includes over 800 automated weather stations in the Western U.S. for mountain snowpack observation (Fleming et al., 2023; USDA Natural Resources Conservation Service, 2022). We used SWE data derived from snow pillow sensors to compare the timing of maximum seasonal SWE with our annual snowmelt runoff onset maps.

2.4 METHODS

2.4.1 *Snowmelt runoff onset retrieval*

We estimated the day of snowmelt runoff onset by identifying the backscatter minima for each pixel in a time series stack of SAR images, following the methodology outlined by Marin et al., (2020). At the backscatter minimum, the snowpack is ripe and runoff begins.

Previous studies of runoff onset primarily use backscatter with VV polarization due to higher signal to noise ratio for wet snow (Naderpour et al., 2022). However, in areas of steep topography, VV is less sensitive to changes in snow wetness (Nagler et al., 2016). In areas with tree cover, VH is preferred due to increased sensitivity below the canopy (Manickam & Barros, 2020). Previous studies have also focused on a subset of available orbits, either one relative orbit with the most ideal incidence angle (~45°) for wet snow separability (Guneriussen et al., 2001; Karbou et al., 2021), a descending orbit (local dawn acquisitions) to remove potential diurnal melt signals (Lund et al., 2022), or multiple ascending or descending relative orbits with full site coverage aggregated into one continuous backscatter time series (Darychuk et al., 2023).

Our workflow uses all available independent measurements of RTC backscatter from different relative orbits (incidence angles 29.1° to 46.0°) and polarizations (VV and VH), which increases temporal sampling while preserving the unique information offered by the different viewing geometries for each relative orbit (Figure 2.1). For a typical mid- to high-latitude location in the Western U.S. covered by 4 relative orbits, our approach effectively improves the temporal resolution from 12 to 3 days, though this depends on the mission observation plan and the number of active Sentinel-1 satellites. For our mid-latitude sites, the median observation interval was 7.8

and 3.2 days for periods with one and two operational satellites, respectively, and 3.9 days for the full 2015 to 2022 period.

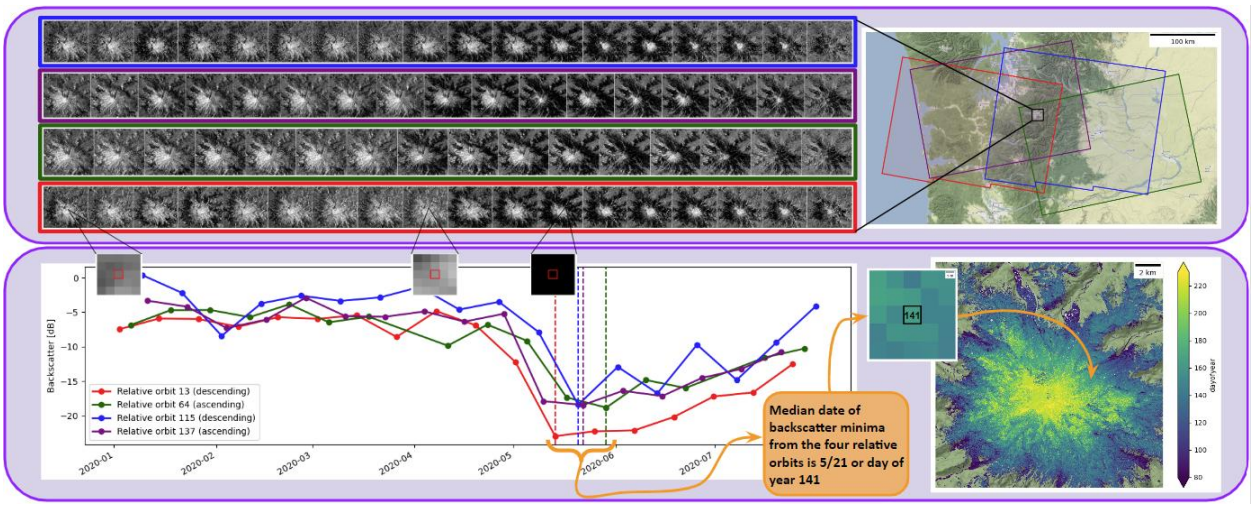

Figure 2.1. Workflow to prepare annual snowmelt runoff onset maps using Sentinel-1 SAR images from all relative orbits. This figure includes only VV images for simplicity, see Figure A.2 for a similar plot with both VV and VH.

We queried the entire archive of Sentinel-1 RTC data for a given area of interest, and analyzed each year separately. For each year, we identified all relative orbits that have at least six observations between February 1st and August 1st, and then for each viable relative orbit and polarization, we identified the date of the backscatter minimum to produce a constituent runoff onset estimate. The number of constituent runoff onset estimates at each pixel ranged from 2-8, based on the number of viable orbits and the available polarizations. We then computed the median of these constituent runoff onset estimates to reduce the effect of outliers, including known RTC processing artifacts near the edges of some scenes (Liang et al., 2021). The final product is an annual snowmelt runoff onset map: a single composite raster for each year, with values corresponding to the estimated day of year for snowmelt runoff onset at each 10 m pixel. We also

computed an 8-year median snowmelt runoff onset map from the individual annual runoff onset maps.

We expected a strong elevation dependence for the snowmelt runoff onset date, with later melt and runoff at higher elevations. To assess the spatiotemporal variability of this elevation dependence across the Cascade Range, we computed a linear fit between all pixels in the 8-year median snowmelt runoff onset maps and elevation, effectively determining the "runoff onset timing lapse rate" for each site. To visualize this relationship, we aggregated the annual runoff onset date estimates over 100 m elevation bins for each year, and created profiles using the median of each bin with over 1000 samples.

We then repeated these calculations with the diurnal anisotropic heating index (DAH), which combines aspect and slope information to quantify the amount of solar radiation that a surface receives (Böhner & Antonić, 2009). This index ranges from -1 to 1 for the relative minimum and maximum cumulative solar radiation. In the northern hemisphere, steep slopes with a south-southwest aspect typically have DAH values close to 1. The DAH has been used to understand snowmelt timing and disappearance (Cristea et al., 2017), and we used a DAH map with 10 m resolution to interpret observed snowmelt runoff onset.

To study the interannual spatiotemporal variability from 2015 to 2022, we computed the median and standard deviation of annual snowmelt runoff onset date for each pixel. We also performed a linear regression of annual snowmelt runoff onset date vs. year at each pixel to assess any apparent trends during this period.

For scalable, reproducible processing and analysis, we developed a suite of open-source tools (Gagliano, 2022) to process and analyze large volumes of publicly available RTC SAR data using these methods. These tools are intended for scalable cloud computing platforms, enabling snowmelt product generation at scale.

2.4.2 *Comparison with in-situ data*

To assess the accuracy of our snowmelt runoff onset timing estimates, we analyzed SWE data from five SNOTEL stations within our study areas (Figure A.2). We identified the day of year corresponding to the maximum measured SWE for each year during the 2015-2022 period. We then computed the median of runoff onset date estimates from the annual maps within a 500 meter buffer around each station. We expected the timing of maximum SWE at the SNOTEL stations to occur around the same time as our snowmelt runoff onset estimates, since SWE begins to decrease from its maximum when the runoff phase begins (Fassnacht et al., 2014).

2.5 RESULTS

From 2015 to 2022, we observe good agreement between the SNOTEL-derived timing of maximum SWE and our annual runoff onset maps with median signed offset of +1 day and median absolute offset of 10 days (Figure A.2). This offset is likely due to some combination of true differences in the timing of maximum SWE (including the influence of sublimation) and runoff onset, sampling rate differences, local snow spatial variability, SNOTEL site geolocation error,

pooling on SNOTEL snow pillows (e.g. Webb et al., 2017), and local tree cover near the SNOTEL stations.

2.5.1 *Mt. Rainier study site*

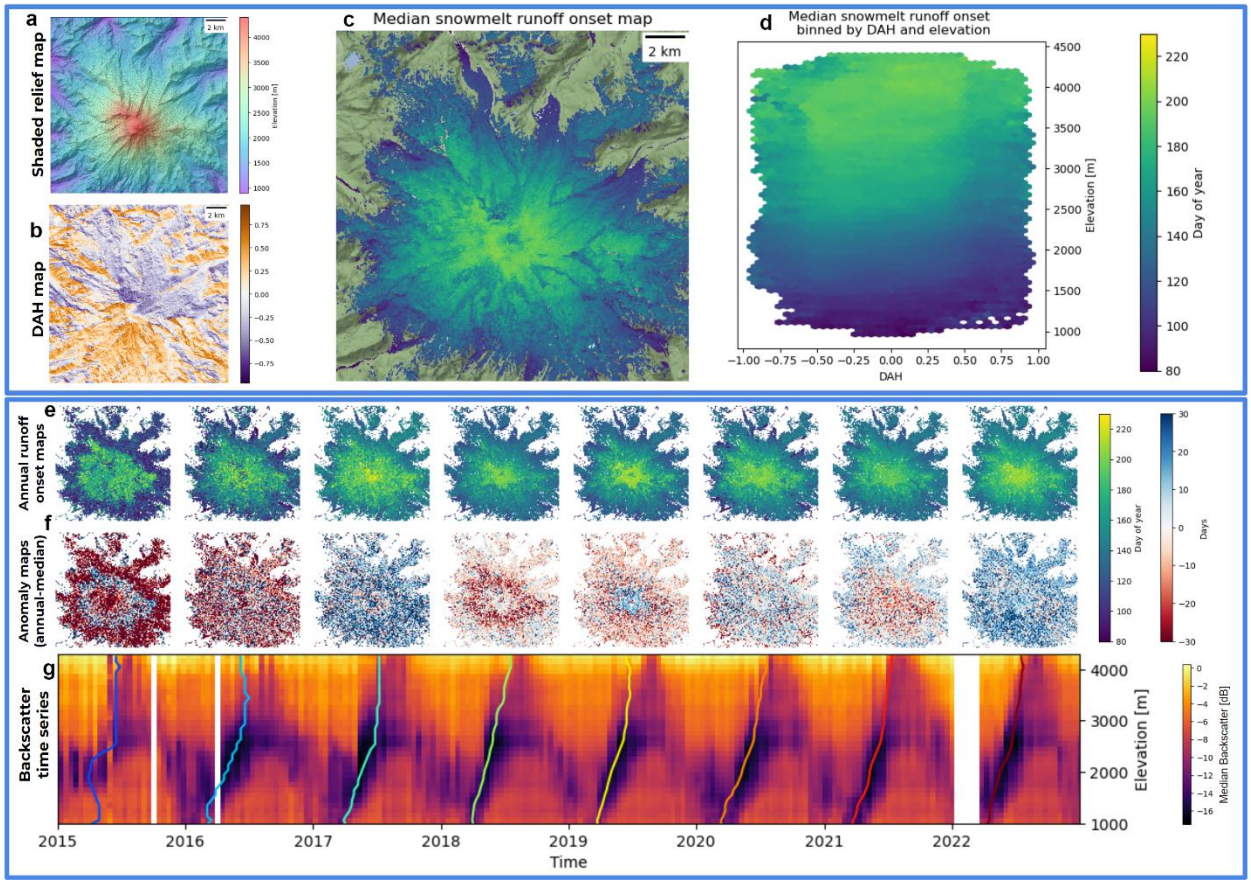

Figure 2.2. (a) Shaded relief map for Mt. Rainier, WA. (b) Diurnal anisotropic heating (DAH) index map. (c) 2015-2022 median day of year snowmelt runoff onset map. (d) Median snowmelt runoff onset date binned by elevation and DAH. (e) Annual snowmelt runoff onset maps. (f) Annual anomaly maps, calculated by subtracting the 8-year median from the annual maps. (g) Time series of median VV backscatter within 100 m bins for each Sentinel-1 acquisition. Colored lines represent the median snowmelt runoff onset for each elevation bin.

The snowmelt runoff onset date depends on elevation, with later runoff onset at higher elevations (Figure 2.2c, 2.2d, 2.2g). In general, the spread between the constituent runoff onset estimates from different relative orbits and polarizations is lowest over relatively smooth surfaces, sparsely vegetated areas, and glaciers, and highest over steep topography, vegetated areas, and lower elevations (Figure A.3). The annual and anomaly maps (Figure 2.2e & 2.2f) show an apparent positive shift towards later annual runoff onset for the period from 2015 to 2022. The backscatter time series shows clear elevation-dependent seasonal patterns (Figure 2.2g). Low elevations have annual backscatter minima in early spring, and the highest elevations have backscatter minima in late summer. Within each season, we observe variable backscatter amplitude for ascending and descending orbits, as well as melt, refreeze, and rain-on-snow events (Figure A.4).

2.5.2 *Topographic and geographic control on the 8-year median snowmelt runoff onset maps*

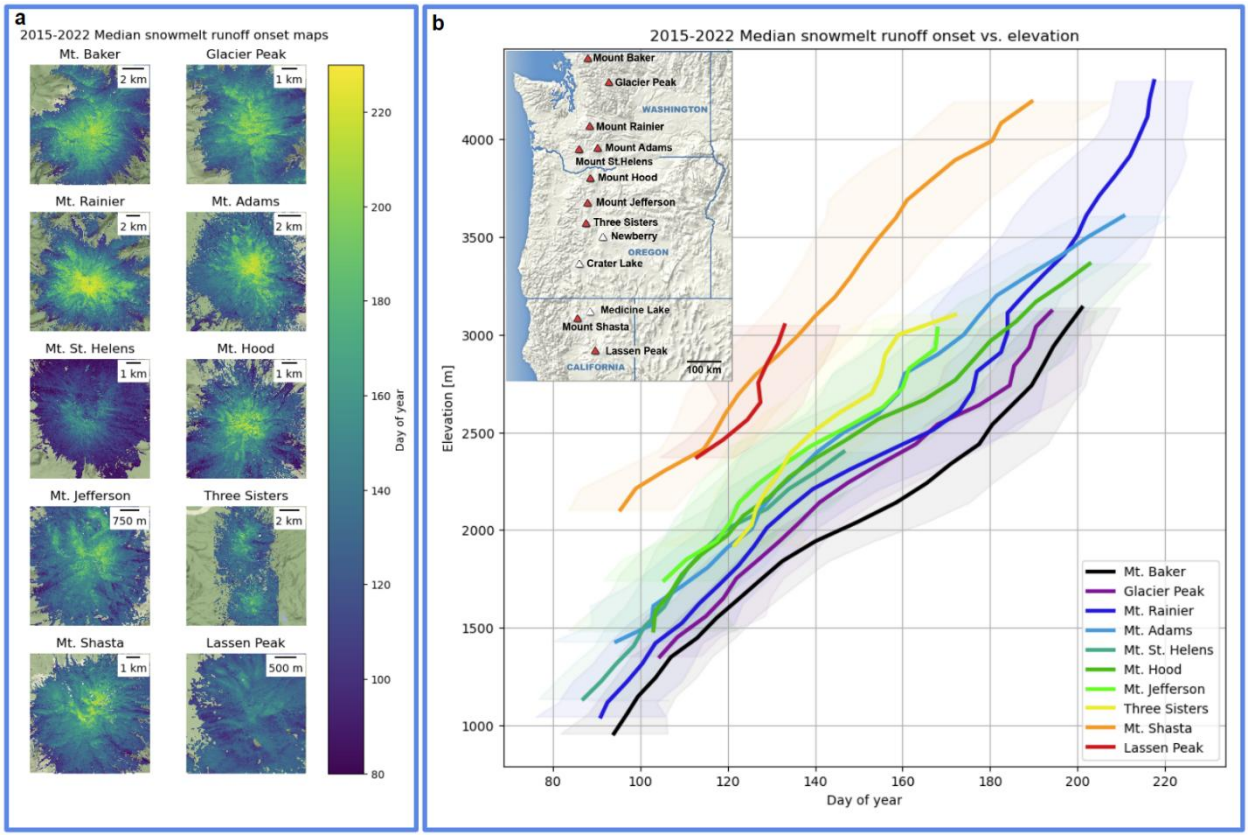

Figure 2.3. (a) 8-year median snowmelt runoff onset maps for the Cascade stratovolcanoes for the period from 2015 to 2022. (b) Median snowmelt runoff onset vs. elevation for each site, with shading showing the standard deviation in each 100 m elevation bin. Note similar runoff onset timing lapse rate for all sites, and later runoff onset for higher latitude sites (see inset map, USGS, Public Domain).

The 8-year median snowmelt runoff onset maps (Figure 2.3a) allow us to better understand the controls on snowmelt by reducing the influence of anomalous years. Across all stratovolcanoes, we observe later snowmelt runoff onset dates at higher elevations (Figure 2.3b). Almost all of the stratovolcanoes show strong elevation dependence with pearson correlation coefficients ranging from r=0.42-0.89, and a median of r=0.81 (Table S1). The runoff onset timing lapse rate was 2.5-6.0 days per 100 m of elevation gain with a median of 4.9 days per 100 m of elevation gain.

Correlation coefficients for DAH were r=0.05-0.45, with a median of r=0.22. Only Lassen Peak shows a stronger apparent dependence on DAH than elevation.

2.5.3 *Interannual snowmelt runoff onset variability*

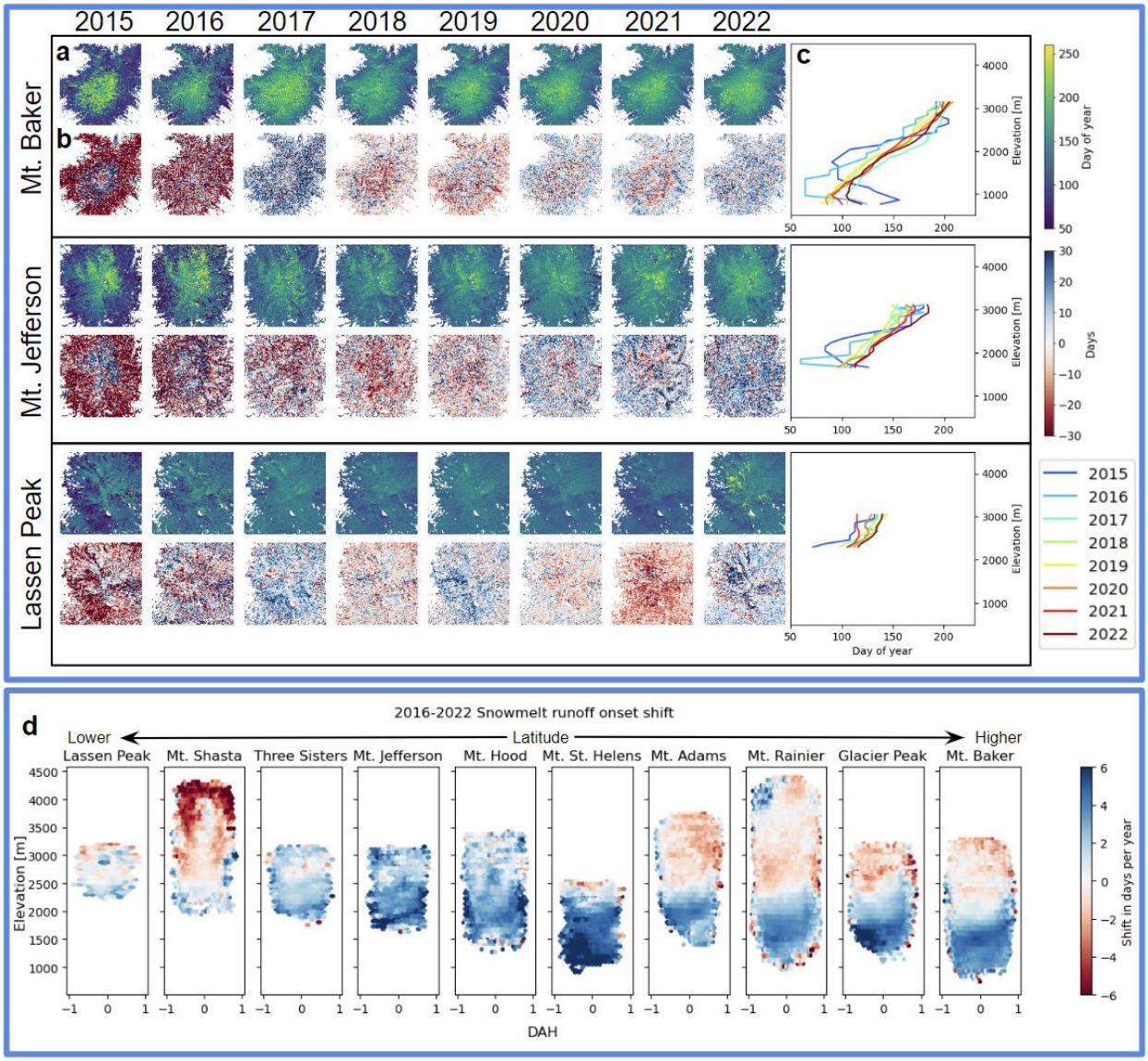

Figure 2.4. (a) Annual snowmelt runoff onset maps. (b) Annual anomaly maps. (c) Runoff onset vs elevation profiles for select sites spanning a range of latitudes (see Figure A.5 for all sites).

Note anomalous values at all sites in 2015. (d) Aggregated linear regression results for 2016-2022 showing apparent shift in snowmelt runoff onset as a function of site latitude, elevation and DAH (see Figure A.8 for original maps). Negative values indicate runoff onset occurring earlier in the year, and positive values indicate runoff onset occurring later in the year.

We observe radially symmetric runoff onset patterns from year to year, and similar runoff onset timing lapse rates with elevation for all sites (Figure 2.4 & Figure A.5). The runoff onset date vs. elevation analysis shows early runoff onset in 2015 and to a lesser extent 2016, especially at lower elevations. When compared to the 8-year median snowmelt runoff onset maps, the 2015 snowmelt runoff onset occurred an average of 25 days early. While the observational period is too short for statistically significant trend analysis, we observe a median shift of +4.3 days per year between 2015 and 2022. If we exclude the anomalous 2015 season, we observe a median shift of +2.0 days per year between 2016 and 2022, though we notice a change in sign around ~2400 m at most stratovolcanoes (Figure 2.4d).

2.6 DISCUSSION

2.6.1 *Mt. Rainier study site*

Our results show repeated, seasonal backscatter cycles due to snowmelt at all elevations (Figure 2.2g). This seasonal signal and subsequent drop in backscatter allow for confident identification of snowmelt runoff onset at most pixels (Figure 2.2c). Generally, we are more confident in estimates of snowmelt runoff onset that show lower spread between the constituent estimates from different relative orbits and polarizations. Higher spread is likely due to some combination of rain-

on-snow events (Figure A.4), vegetation, sub-pixel aspect and slope variability, variable acquisition geometry, layover, and other radar artifacts.

2.6.2 *Topographic and geographic controls on the 8-year median snowmelt runoff onset maps*

The 8-year median snowmelt runoff onset maps show later snowmelt runoff onset at all elevations for higher latitude stratovolcanoes (Figure 2.3b). Elevation was the primary control on snowmelt runoff onset, which is likely related to adiabatic lapse rate. This relationship held for all sites except Lassen Peak, which showed weak elevation control, possibly due to its limited elevation range. The runoff onset timing lapse rate results show a median delay in snowmelt runoff onset of 4.9 days per 100 m of elevation gain, and we found that the magnitude of this delay shows a correlation with latitude. Sites at higher latitudes have not only later snowmelt runoff dates, but also higher runoff onset timing lapse rates. For each 1 degree increase in latitude, the runoff onset date is 7.5 days later in the year ($r=0.95$), and the runoff onset lapse rate increases in magnitude by 0.3 days per 100 m of elevation gain ($r=0.75$).

Interestingly, the snowmelt runoff onset does not strongly depend on DAH, though there appears to be moderate correlation at mid to high elevations (Figure A.6). This is likely due to the fact that at lower elevations, snowmelt runoff onset is more strongly controlled by meteorological variables like air temperature. However, the proportion of melt due to shortwave radiation increases at higher elevations due to colder temperatures and less liquid precipitation (Garvelmann et al., 2014; Mazurkiewicz et al., 2008; Stigter et al., 2021). Cloud cover could also play a role, with a

continuous cloud layer present around the stratovolcanoes during most of winter and spring. Solar radiation is unobstructed at elevations above the cloud layer, and below the cloud layer, solar radiation is both reduced and has a relatively uniform distribution across different slopes and aspects, which could lead to a weaker dependence on DAH at lower elevations during the early melt season.

2.6.3 *Interannual snowmelt runoff onset variability*

We observed a 2015 snowmelt runoff onset 25 days earlier than the 2015-2022 median. This coincides with the 2015 snow drought, as well as a warmer than usual early spring (Mote et al., 2016). The 2015 maps also display atypical runoff onset estimates for the lowest elevation bins, often below ~2000 m (Figure A.5), suggesting that limited or no snow was present at these elevations and the timing of the observed backscatter minimum may not represent a snowmelt signal. This ambiguity could be eliminated with near-daily, high-resolution binary snow mask products. While ongoing efforts using PlanetScope images are promising (K. Yang et al., 2023), operational products with broad coverage are not currently available.

In general, glaciers and relatively smooth slopes tend to have lower interannual variability of snowmelt runoff onset estimates when compared to surrounding exposed cliffs and ridges. Besides these areas of complex topography, we notice relatively uniform spatial interannual variability (Figure A.7), indicating that while runoff onset may have an absolute shift from year to year at all elevations, the runoff onset lapse rate remains somewhat constant.

We identified repeated annulus patterns between approximately ~2300-2800 m in the anomaly maps (Figure A.5), especially those of the northernmost stratovolcanoes: Mt. Baker, Glacier Peak, Mt. Rainier, and Mt. Adams. These features suggest that different mechanisms influence snowmelt runoff onset timing at these elevations, such as mid-season rain events.

We observed a median runoff onset shift of +2.0 days per year between 2016 and 2022, though there is significant variability across elevations. Specifically, there is an apparent trend towards later snowmelt runoff onset below ~2400 m, and a weaker trend towards earlier snowmelt runoff onset above ~2400 m (Figure 2.4d). With only 8 years of data, these short-term trends are likely not representative of longer-term climate trends. In fact, most literature suggests that the beginning of snowmelt is shifting earlier in the year for the Western U.S. (Evan, 2019; Hale et al., 2023; Stewart, 2009; US EPA, 2021). The apparent short term trend could be explained by regional climate oscillations: since 2015, the ENSO and PDO indices both generally shifted from El Niño and warm-PDO states to La Niña and cold-PDO states (Huang et al., 2017). When ENSO and PDO are in phase, the ENSO climate signal is stronger, bringing colder temperatures and more winter precipitation to the region (Gershunov & Barnett, 1998), which should result in later snowmelt runoff onset.

2.6.4 *Future work*

We are scaling our processing and analysis to study snowmelt runoff globally. This will reveal the spatiotemporal variability of global snowmelt runoff and provide another metric to assess the impacts of ongoing climate change. We also plan to integrate SAR backscatter data from the upcoming NISAR mission and the growing constellations of commercial SAR satellites. With

global L-band coverage and a 12-day repeat interval, NISAR will allow for improved results for seasonal snow beneath the canopy. With hourly to daily revisit times, commercial X-band SAR satellites (e.g., Capella, ICEYE) can potentially capture diurnal snowmelt evolution.

Though we are limited by the current revisit time (~6 or 12 days) and latency of Sentinel-1 data availability (~24 hours), future adaptation of our work can provide an operational framework for near-real-time and predictive methods which have the potential to improve sub-daily streamflow forecasting. To explore this potential, we compared the timing of snowmelt runoff offset and streamflow for one of the watersheds in our study area (Figure A.9), and we are now expanding this analysis across a large sample of watersheds in the Western U.S.

2.7 CONCLUSION

We developed a scalable pipeline to generate annual snowmelt runoff onset maps utilizing all relative orbits and polarizations from Sentinel-1 RTC SAR backscatter data products. We used these tools to create and analyze snowmelt maps over stratovolcanoes in the Cascade Range. We found strong elevation and latitude controls on snowmelt timing. We observed apparent trends in snowmelt runoff onset date over the available 8-year record and documented early snowmelt runoff onset for 2015, an anomalously low snow year. Our open-source tools will enable scientists and operational users with limited SAR and/or cloud computing experience to quickly build snowmelt runoff onset maps anywhere on Earth.

Chapter 3. A GLOBAL HIGH-RESOLUTION DATASET OF SNOWMELT RUNOFF ONSET TIMING FROM SENTINEL-1 SAR, 2015-2024

This chapter is in preparation for submission to Earth System Science Data.

3.1 ABSTRACT

Snowmelt runoff onset timing represents a critical hydrological parameter, particularly in mountainous regions where seasonal snow serves as a natural reservoir for downstream water resources. Despite this importance, high-resolution observational data of snowmelt runoff onset across complex terrain has been limited by the challenges of sparse in-situ monitoring networks, intermittent optical remote sensing data, and coarse passive microwave remote sensing data. To address this gap, we present a global dataset of snowmelt runoff onset timing for 2015-2024, covering nearly all seasonal snow on Earth with 80-meter spatial resolution and 9.3 day average temporal resolution. We created this dataset using Sentinel-1 C-band SAR to detect backscatter minima indicative of runoff onset, with a custom MODIS-derived snow phenology dataset defining where and when to search for these signals. Validation against over 900 automated weather stations in the Western United States demonstrated strong agreement between our dataset and in-situ snow pillow estimates of runoff onset, with a median timing difference of -1.0 days and a median absolute deviation of 9.0 days. Systematic analysis of environmental controls on dataset performance identified forest cover fraction, SWE accumulation, and temporal resolution as critical factors affecting dataset performance. The dataset includes global annual runoff onset

products for each water year, annual local temporal resolution products for each water year, and 10-year composites of median runoff onset, median absolute deviation, and local temporal resolution. This unique combination of high spatial resolution, global coverage, decade-long temporal coverage, and empirically-validated performance recommendations provides unprecedented detail of snowmelt runoff onset patterns across seasonal snow-covered regions. Our snowmelt runoff onset dataset will enable improved understanding of mountain hydrological processes, climate change impacts on the cryosphere, and inform water resource management in snow-dominated watersheds.

3.2 INTRODUCTION

Snow plays a crucial role in the global water cycle and climate system, and more than one-sixth of the world's population relies on meltwater from seasonal snow and glaciers (Barnett et al., 2005). This dependence is particularly pronounced in mountainous regions, where seasonal snowpacks act as a natural reservoir, storing water as snow in the winter and gradually releasing it during spring and summer months. Critically, snowmelt runoff onset marks the beginning of increased water availability, initiating the annual hydrologic pulse that sustains downstream ecosystems and human water needs during the warmer months (Dingman, 2015). This snowpack-scale process is distinct from basin-scale streamflow generation, which typically lags by days to weeks depending on basin characteristics such as basin topography, vegetation, bedrock permeability, groundwater storage capacity, soil moisture conditions, and hillslope and groundwater travel times (Brooks et al., 2025; Lowry et al., 2010).

Beyond its hydrological significance, snowmelt timing also serves as a key indicator of regional climate change (Dudley et al., 2017). As a process highly sensitive to temperature and precipitation

variations, shifts in snowmelt patterns provide tangible evidence of changing climate conditions, often manifesting before other environmental indicators become apparent. In recent decades, climate change has significantly impacted global snow accumulation and snowmelt patterns (Ismail et al., 2023; Royer et al., 2021; Yang et al., 2022). Though these specific patterns are non-uniform and vary regionally, they have far-reaching consequences for water security, agricultural productivity, and ecosystem health in snow dominated regions and beyond (Qin et al., 2022).

Traditional methods for monitoring snowmelt, such as in-situ measurements from snow courses and snow pillows, provide valuable point data but require labor-intensive collection that prohibits the spatial coverage necessary for regional and global analysis. While these measurements can indirectly indicate melt occurrence based on decreases in SWE, they do not directly measure liquid water content of the snowpack. Optical remote sensing data from platforms like Landsat, Sentinel-2, and MODIS, can provide observations of fractional snow-covered area with broad spatial coverage, but these remote sensing approaches only indirectly indicate melt occurrence through decreases in snow cover, and additionally suffer from persistent cloud cover during critical melt periods (Awasthi & Varade, 2021). Passive microwave sensors have been used for large scale snowmelt detection (Mioduszewski et al., 2015; Zheng et al., 2022), but are limited by very coarse spatial resolution (typically 25 km) which fails to capture snowmelt variability in the characteristically complex terrain of snow-dominated regions.

Synthetic Aperture Radar (SAR) overcomes many of these limitations due to its all-weather imaging capability, high spatial resolution, and sensitivity to liquid water content in snowpack (Rott & Nagler, 1995; Tsai et al., 2019). The European Space Agency's Sentinel-1 C-band SAR

mission is particularly useful for snowmelt monitoring due to its global coverage and frequent (often 6 or 12 day) exact repeat interval. When a snowpack is dry, C-band radar can penetrate through the entire snowpack (up to ~20 m), with backscatter dominated by the snow-ground interface (Mätzler, 1987; Nagler et al., 2016). However, the presence of liquid water dramatically alters the dielectric properties of snow, causing greater absorption of C-band radiation, shallow penetration depth (~5-10 cm), and consequently, a significant decrease in backscatter (Lund et al., 2020; Nagler, 1996).

Studies of C-band SAR backscatter time series have established that the minimum backscatter amplitude coincides with the transition from the ripening phase to the runoff phase of snowmelt (Darychuk et al., 2023; Gagliano et al., 2023; Lund et al., 2022; Marin et al., 2020). Carletti et al. (2025) provided a more rigorous physical understanding of the relationship between this characteristic backscatter minimum and runoff onset, combining high-resolution field measurements and radiative transfer modeling to demonstrate that the backscatter decrease to the characteristic minimum is caused by signal absorption from increasing liquid water content, while the subsequent post-minimum backscatter increase is controlled by evolving snow surface roughness during the runoff phase. Importantly, Carletti et al. (2025) emphasizes that rather than directly detecting the initiation of runoff onset, the backscatter minimum is caused by the complex interplay of these factors when the snowpack is already isothermal and likely releasing water. Despite these complexities at the process scale, this backscatter minimum and runoff onset timing relationship has been validated in diverse mountain environments against various reference measurements, including snow pillows at automatic weather stations (Darychuk et al., 2023; Gagliano et al., 2023; Gao & Ma, 2024; Marin et al., 2020), soil moisture pulses at automatic

weather stations (Detre et al., 2025), snow pit measurements (Lund et al., 2022; Rickenbaugh, 2023), a C-band SAR tower-based study (Brangers et al., 2024), and streamflow observations (Gagliano et al., 2023; Lund et al., 2022; Rickenbaugh, 2023).

However, the complexities revealed by Carletti et al. (2025) highlight the need for improved methodological approaches that can robustly detect snowmelt runoff onset across diverse environmental conditions. In previous work, we developed such an approach by integrating all available Sentinel-1 relative orbits, demonstrating enhanced temporal resolution and estimate robustness for snowmelt runoff onset mapping at a selection of stratovolcanoes in the Pacific Northwest of the United States (Gagliano et al., 2023). Here, we refine and scale this approach globally, combining our multi-orbit methodology – which provides multiple independent observations across different viewing geometries and times – with a custom MODIS-derived snow phenology dataset to constrain the temporal search window for runoff onset estimation. This integrated approach addresses several key challenges in snowmelt runoff onset detection, including many of those identified by Carletti et al. (2025): low temporal resolution of individual relative orbits, sensitivity to viewing geometry, false detection from isolated melt episodes, and false detection when or where no seasonal snow exists.

Using this refined methodology, we present a global dataset of snowmelt runoff onset timing for 2015-2024. We document the data processing workflow, describe the dataset structure, validate the dataset against a network of automated weather stations, establish empirically-derived environmental performance recommendations, and discuss key characteristics and limitations. This dataset provides unprecedented global coverage of snowmelt timing at high spatial resolution,

offering valuable information for hydrological modeling, water resource management, and ecological research.

3.3 DATA AND METHODS

3.3.1 *Input data sources*

3.3.1.1 Sentinel-1 SAR backscatter

We utilized the entire archive of Sentinel-1 C-band SAR data in Interferometric Wide mode, available as radiometrically terrain-corrected (RTC) cloud-optimized geoTIFFs hosted on Microsoft Planetary Computer (Microsoft Open Source et al., 2022). For each water year from 2015 to 2024, we selected all available VV-polarized scenes, which have demonstrated superior performance for snowmelt runoff onset identification when compared to VH polarization (Darychuk et al., 2023). Though the RTC images are available at 10-meter resolution, we leverage the pre-computed 80-meter overview embedded in the Cloud-Optimized GeoTIFF files in order to balance computation costs, accuracy, and spatial resolution. This resolution selection aligns with Manickam and Barros (2020), who found through area-variance scaling analysis that SAR backscatter measurements of snow exhibit minimum variance at characteristic spatial scales (~100-1000 m depending on terrain and forest cover), suggesting that our 80 m resolution captures wet snow spatial variability while remaining computationally efficient.

3.3.1.2 MODIS snow cover

We used the 500-meter resolution MODIS MOD10A2 8-day maximum snow extent product (Hall & Riggs, 2021) hosted on Microsoft Planetary Computer (Microsoft Open Source et al., 2022) to prepare a custom snow phenology dataset. This product accounts for cloud cover by reporting the

maximum snow extent from up to eight daily observations, recording snow presence if detected on at least one cloud-free day within each eight-day period.

3.3.1.3 Automatic weather station network

For in-situ estimation of snowmelt runoff onset, we accessed snow pillow measurements in the Western U.S. from both the SNOTEL network (Fleming et al., 2023; USDA Natural Resources Conservation Service, 2022) and the network operated by the California Cooperative Snow Surveys program and available on the California Data Exchange Center (California Department of Water Resources, 2025). To improve SNOTEL site geolocation accuracy, we used updated coordinates for 455 SNOTEL site locations (Detre et al., 2025). Though the snow pillow data is available at hourly intervals, we used snow pillow data at daily intervals to reduce measurement noise.

3.3.1.4 Forest cover fraction

We used the Copernicus Global Land Service: Land Cover 100 m: collection 3: epoch 2019: Globe (V3.0.1) dataset (Buchhorn et al., 2020) to gather forest cover fraction for masking during evaluation and interpretation of results. This global product is derived from PROBA-V satellite observations and ancillary datasets and includes fractional land cover layers representing the percentage ground cover of 10 different land cover classes at 100-meter resolution. We utilized the forest cover fraction layer to identify and mask heavily forested areas (>0.5) during evaluation of our SAR-based product, as dense forest canopies complicate C-band snowmelt runoff onset detection.

3.3.2 *Dataset creation methodology*

We developed a workflow that integrates two complementary remote sensing datasets to detect snowmelt runoff onset reliably at a global scale (Figure 3.1). First, we created a custom MODIS-derived snow phenology dataset to identify where and when seasonal snow exists. Within these constraints, we analyze Sentinel-1 SAR backscatter time series to detect characteristic minima that

indicate runoff onset. This approach leverages the individual strengths of both sensors: MODIS provides reliable snow cover detection and timing constraints that Sentinel-1 cannot achieve alone, while Sentinel-1 offers superior spatial resolution, weather-independent observations, and sensitivity to liquid water content changes during snowmelt. To create the snowmelt runoff onset dataset, we scaled this methodology from individual pixel processing to global coverage through a distributed computing architecture that processed over 100 TB of Sentinel-1 data acquired between October 1, 2014 and March 31, 2025.

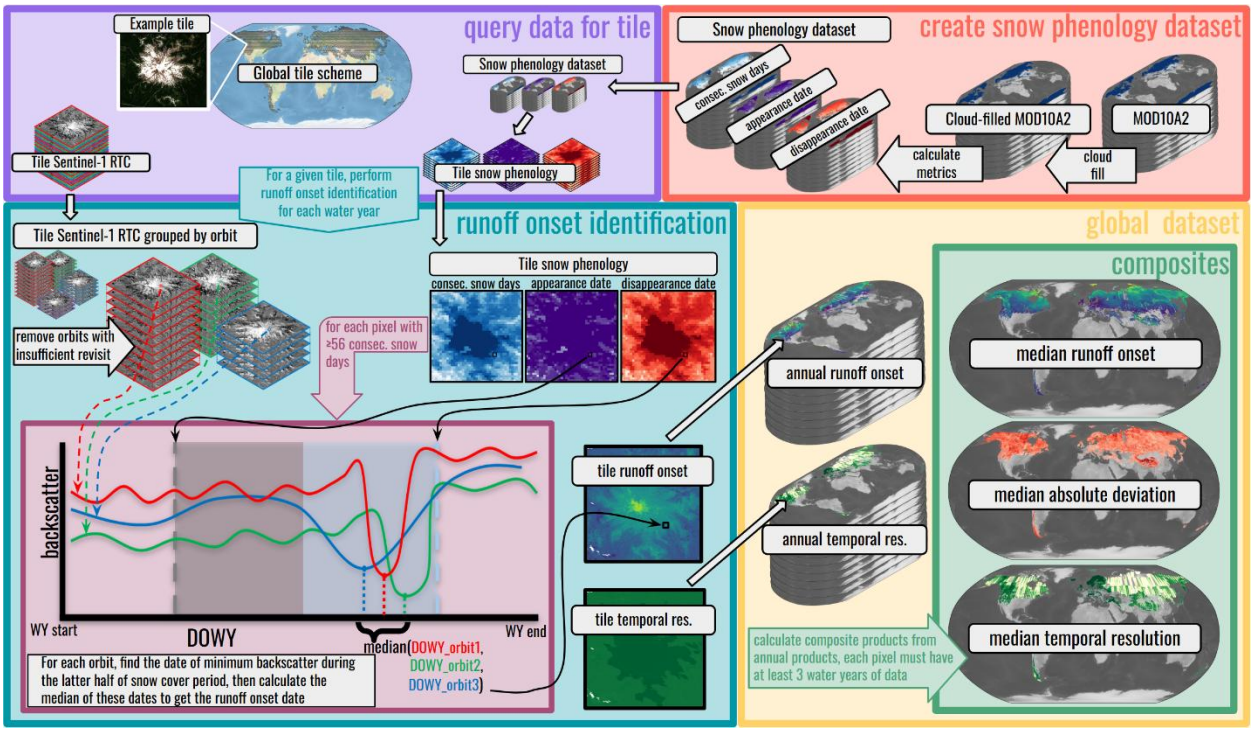

Figure 3.1. Graphical representation of the workflow used to create the global snowmelt runoff onset dataset. The MODIS-derived snow phenology dataset is initially created (top right) to guide runoff onset identification. For a given processing tile (shown here zoomed to Mt. Rainier, WA), the Sentinel-1 RTC backscatter data and snow phenology dataset are both queried for all water years (top left). To calculate runoff onset for a single water year (center left), Sentinel-1 data are first grouped by relative orbit and filtered to ensure sufficient revisit interval. For every pixel with >= 56 days consecutive snow days in the snow phenology dataset, the backscatter minimum during the latter half of the snow covered period is identified across multiple relative orbits and the median date becomes the runoff onset estimate (bottom left inset). The resulting

products for the tile are mosaicked to create global annual products (center right), and global composite products are created from the stack of annual products (bottom right).

3.3.2.1 Snow phenology dataset

Central to our methodology was the development of a custom snow phenology dataset (Gagliano, 2025a) derived from the MODIS MOD10A2 8-day maximum snow extent product using the MODIS_seasonal_snow_mask software library (Gagliano, 2025b). Snow phenology refers to the seasonal timing of snow cover events, including snow appearance, persistence, and disappearance patterns (Tang et al., 2022). This dataset provides the foundational spatial and temporal constraints for the runoff onset workflow by defining where and when to search for runoff onset signals in the Sentinel-1 data in each water year, using the snow cover, snow appearance date, and snow disappearance date products, respectively.

The MOD10A2 8-day maximum snow extent product represents the maximum snow extent observed over each 8-day MODIS compositing period, which reduces cloud contamination compared to daily observations, yet still contains substantial data gaps due to clouds and polar darkness that obscure snow presence during critical transition period. We applied an enhanced cloud-filling algorithm that builds on the methodology of Wrzesien et al. (2019), which assumes that snow-covered observations bracketing cloudy periods indicate continuous snow presence, which is particularly useful during persistent cloud cover coinciding with the snowmelt season. Processing occurs continuously across all years before water year segmentation, ensuring proper capture of continuous snow periods spanning water year boundaries. For polar regions above ~70° latitude, we implemented additional filtering to remove false “no snow” classifications during polar night periods, when the ~10:30 AM local MODIS observations are unreliable due to darkness.

From this cloud-filled data, we extracted three key variables for each pixel and water year: the number of continuous snow cover days, snow appearance date (first date of continuous snow cover), and snow disappearance date (first day after the last date of continuous snow cover). For

pixels with multiple snow covered periods within a single water year, we selected the longest continuous period.

These variables constitute valuable snow phenology data for the broader scientific community– beyond serving as the basis of our runoff onset methodology, this 10-year global dataset represents a significant standalone product offering global characterization of snow phenology patterns that can inform water resource management, ecological studies, and climate change research (Gagliano, 2025a).

3.3.2.2 Snowmelt runoff onset identification

We limited identification of snowmelt runoff onset to pixels identified with seasonal snow cover for the respective water year in our snow phenology dataset, specifically with at least 56 days of continuous snow presence, approximating the 60-day threshold from Sturm et al. (1995) but still divisible by 8 days, given the temporal resolution of our phenology product. This threshold serves two purposes: it distinguishes between ephemeral snow events with minimal hydrological impact, and it ensures sufficient time for complete snowmelt phase progression, through the warming, ripening, and runoff phases, which is necessary for reliable detection of the characteristic backscatter minimum associated with runoff onset (Carletti et al., 2025).

For pixels meeting this seasonal snow criterion, we analyzed the temporal evolution of Sentinel-1 VV-polarized backscatter to identify snowmelt runoff onset. Our preprocessing workflow included quality filtering to remove unrealistically low backscatter values (VV backscatter < -30 dB) and border noise artifacts (Ali et al., 2018), followed by temporal filtering using our snow phenology dataset to restrict analysis to the appropriate temporal detection window for each pixel and water year.

We processed each Sentinel-1 relative orbit independently to account for systematic backscatter differences between viewing geometries caused by varying incidence angle and azimuth orientation. Each relative orbit maintains consistent viewing geometry while providing regular temporal sampling of the same location, typically every 12 days, with overpass times in the early morning for descending relative orbits (~6 AM. local) and early evening for ascending relative

orbits (~6 PM local). To ensure adequate temporal sampling, we did not consider relative orbits with less than 1 observation per 30-day period or gaps of more than 30 days between consecutive acquisitions during the snow-covered period.

For each valid pixel-relative orbit combination, we identified the timing of minimum backscatter as the relative orbit-specific runoff onset date, searching within the latter half of the snow-covered period and extending through 16 days after the snow disappearance date (two additional MODIS snow cover periods). We constrained our search to the latter half of the snow-covered period because early season melt events often represented diurnal melt-refreeze cycles or rain-on-snow episodes followed by refreezing without sustained runoff, creating temporary backscatter minima unrelated to true runoff onset. By limiting analysis to the latter half of the snow-covered period, we were more likely to detect backscatter minima that are representative of sustained runoff onset. The 16-day extension of the temporal search window accounted for the spatial scale difference between MODIS (500 m) and Sentinel-1 (80 m) data, as residual patches of snow cover may have persisted within the coarser MODIS pixel, even when the MODIS products indicated snow disappearance (Crumley et al., 2020; Pflug et al., 2024).

For each pixel, we calculated the median date across all valid relative orbit-specific minimum backscatter estimates to produce a single robust estimate for that pixel and water year. This multi-orbit aggregation approach serves dual purposes: mitigating differences due to viewing geometry and orbit-specific artifacts, while effectively increasing the temporal resolution by combining observations from multiple relative orbits (Gagliano et al., 2023). The resulting annual runoff onset products represent our primary data product, providing pixel-wise runoff onset timing estimates with global coverage for water years 2015 to 2024. We also estimate the annual temporal resolution for all pixels with runoff onset timing estimates, calculated as the length of the valid observation window in days divided by the number of Sentinel-1 observations contained within that period.

We report all runoff onset dates as day of water year (DOWY), with the water year starting on October 1st of the previous year in the northern hemisphere and April 1st of the current year in the southern hemisphere (Aguayo et al., 2021; Cortés & Margulis, 2017).

3.3.2.3 Processing and scaling

The global scope of this analysis, spanning 10 water years across all seasonal snow on Earth, necessitated the development of a distributed computing approach capable of efficiently processing >100 TB of Sentinel-1 data. To ensure computational feasibility, data integrity, and reproducibility, we implemented an open-source, cloud-based processing architecture described below.

We partitioned the global domain into 23,520 seamless tiles, each covering 2048 x 2048 pixels (~164x164 km at the equator). We then pre-allocated a global Zarr data store (Abernathey, 2024) with this global array structure and optimized chunking in order to support parallel processing, where each worker could independently process individual tiles and write results directly to the final data structure without conflicts. This "embarrassingly parallel" approach allowed us to seamlessly scale from small regional processing to full global coverage using cloud computing resources.

Of the 23,520 total tiles, we limited processing to the 4,313 tiles that contained both seasonal snow and the relevant Sentinel-1 RTC data. Our processing workflow leveraged the Dask computing library, utilizing Dask's lazy evaluation and distributed computed capabilities to coordinate parallel processing across Coiled cloud computing infrastructure (Dask Development Team, 2016). We implemented a multi-stage chunking strategy to optimize memory-bandwidth tradeoffs across distributed workers: with chunking along the spatial dimension for data I/O heavy operations to maximize throughput, and chunking along the time dimension for computationally intensive time-series calculations.

We deployed and monitored computing resources on Microsoft Azure West Europe region, where Planetary Computer datasets are hosted. To balance computation costs and speed, we predominantly processed tiles in batches of 10, with 60 workers per batch (32GB memory, 4 cores each).

3.3.2.4 Generation of 10-year composite products

To aid in the interpretation of the annual snowmelt runoff onset products, we created three additional composite products for pixels with at least three years of valid annualt data. We calculated the median snowmelt runoff onset date across all available years, creating a 10-year median snowmelt runoff onset composite product. To quantify interannual variability, we created a 10-year snowmelt runoff onset median absolute deviation composite product. Finally, we created a 10-year local median temporal resolution composite product to capture the temporal resolution of these composites. These complementary products can be used for detailed study of the characteristic snowmelt runoff onset date and variability for any given pixel, providing a better understanding of the influence of fixed geographic controls (elevation, aspect, latitude) and environmental forcing (temperature and precipitation) for observed snowmelt runoff onset variability.

3.3.3 *Dataset validation methodology*

We employed a two-stage validation approach, evaluating our snowmelt runoff onset estimates against runoff onset estimates from in-situ snow pillow snow water equivalent (SWE) measurements at over 900 automated weather stations across the Western U.S. First, we conducted a comprehensive pixel-wise environmental controls analysis, examining all available pixels within a 1000 meter radius of all stations and all years to characterize how environmental factors affect dataset performance. We then use these empirically-derived thresholds to apply appropriate quality filters for station-level validation, ensuring robust performance assessment while providing practical guidance for dataset users.

For snow pillow runoff onset estimates, we first applied quality filters to daily SWE time series at each station, removing observations with negative SWE values and physically unrealistic apparent daily change (>20 cm/day). Further, we excluded water years with less than 10 cm SWE, less than 60 days of continuous snowcover, or data gaps exceeding 10 days, resulting in a total of 7,916 water years of snow pillow time series across 946 stations. Using the filtered time series, we calculated snow pillow runoff onset as the last day when SWE decreased beyond 95% of the water year maximum. We chose this timing instead of directly selecting the timing of maximum SWE in order to account for SWE decreases due to wind redistribution or sublimation, as well as to

mitigate scenarios where maximum SWE occurs early in a season and persists but doesn't melt significantly until later in the season (Dingman, 2015; Fassnacht et al., 2014).

However, environmental factors such as forest canopy density complicate C-band SAR interactions with the underlying snowpack. To optimize our validation approach and provide guidance for dataset users, we performed a pixel-wise environmental controls analysis within 1000 meter radii of the weather stations, examining how different environmental variables affect agreement between individual pixel-wise estimates from our annual snowmelt runoff onset products and estimates from nearby snow pillow runoff onset timing. We subtracted the snow pillow runoff onset estimates from the individual pixel estimates in the annual runoff onset products, and binned the residuals by forest cover fraction, temporal resolution, and maximum SWE accumulation. For each bin, we calculated both the median absolute deviation to quantify the spread of the residuals, as well as the median difference to quantify the bias.

We designed our station-level validation based on this analysis showing performance degradation over 0.5 forest cover fraction, under 20 cm of maximum SWE accumulation, and temporal resolution coarser than 14 days (see section 3.5.1). For each water year, we calculated SAR runoff onset estimates by extracting the median runoff onset date from our annual runoff onset products within a 1000 meter radius, masking out pixels with a forest cover fraction greater than 0.5 or a temporal resolution coarser than 14 days, and requiring at least 10% valid pixel coverage within the 3.14 km² area. We discarded water years where maximum SWE accumulation did not reach 20 cm. This resulted in a total of 4,763 water years of runoff onset estimate pairs across 735 stations. We then computed timing differences between our annual runoff onset products and the snow pillow runoff onset estimates for each water year.

3.4 DATASET DESCRIPTION

3.4.1 *Dataset overview*

The global snowmelt runoff onset dataset contains five groups of products organized in a cloud-optimized Zarr store designed for efficient distributed access, processing, and analysis. The dataset

spans the global domain from 180°W to 180°E longitude and 60°S to 81.1°N latitude, encompassing all major seasonal snow regions on Earth. All products are georeferenced to the WGS84 coordinate system (EPSG:4326) at 80-meter spatial resolution. The temporal dimension spans 10 water years (2015-2024), resulting in a complete dataset structure with dimensions (water_year: 10, latitude: 195970, longitude: 499998) for annual products, and (latitude: 195970, longitude: 499998) for the 10-year composite products. Though the original values are stored as integer or floating point numbers, all values are encoded as signed 16-bit integers, with no-data values of -9999. For the annual runoff onset products and 10-year median runoff onset composite product, values are integer DOWY. For the annual local median temporal resolution products, and 10-year local median temporal resolution and median absolute deviation composite products, values are floating point decimal days with precision limited to 0.1 days (accordingly stored with a scale factor of 0.1).

3.4.2 *Dataset variables*

3.4.2.1 Annual runoff onset products

The “runoff_onset” variable contains integer day of water year (DOWY) representing runoff onset date estimates for each individual water year from 2015 to 2024, stored as a 3-dimensional array with dimensions (water_year, latitude, longitude). All DOWY dates are relative to their respective hemispheres’ start of water year, discussed further in section 3.3.2.2. Valid DOWY values range from 1 to 366.

3.4.2.2 Annual local temporal resolution products

The dataset also includes an accompanying “temporal_resolution” variable to document the average local temporal resolution of our method at each pixel for each individual water year (water_year, latitude, longitude). These “temporal_resolution” values are in units of decimal days.

3.4.2.3 10-year composite products

The “runoff_onset_median” variable stores the 10-year median runoff onset composite product expressed as a DOWY date (Figure 3.2, Top), while the “runoff_onset_mad” variable contains the 10-year median absolute deviation composite product in decimal days (Figure 3.2, Middle). The

“temporal_resolution_median” variable is the 10-year local median temporal resolution composite product in decimal days (Figure 3.2, Bottom). These 2-dimensional products (latitude, longitude) are useful for understanding typical runoff onset timing, interannual variability of runoff onset timing, and the typical local temporal resolution of our method, respectively. As discussed in section 3.3.2.4, these composite products are only calculated at pixels that have 3 or more water years worth of data.

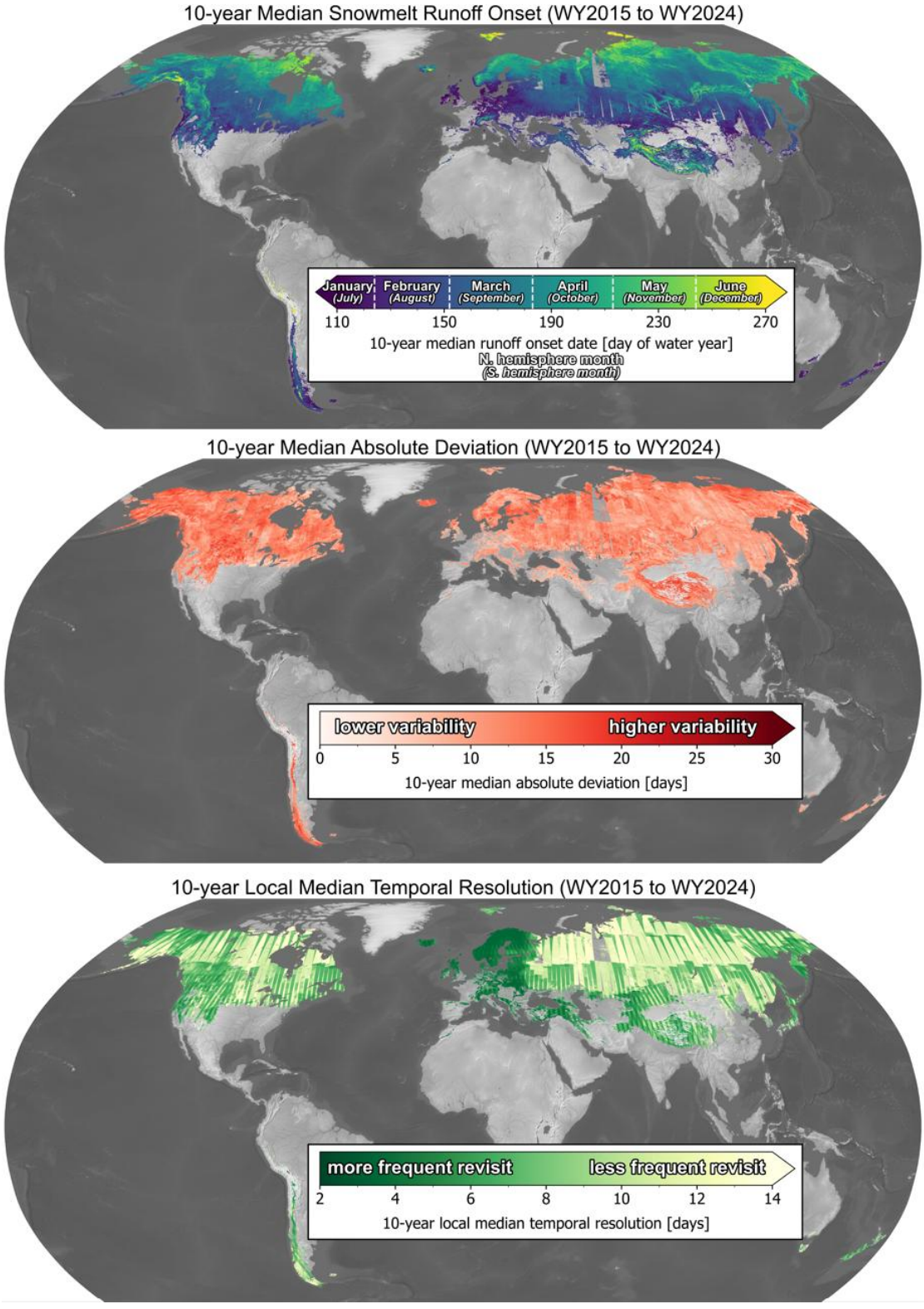

Figure 3.2. Global snowmelt runoff onset composite products. (Top) 10-year median snowmelt runoff onset, (Middle) 10-year median absolute deviation, and (Bottom) 10-year local median temporal resolution composite product.

3.4.3 *Spatial coverage and temporal resolution*

Dataset spatial coverage is constrained by the availability of Sentinel-1 Interferometric Wide mode data. Because Sentinel-1 data acquired over Antarctica and much of the Arctic is captured in Extra Wide mode, regions including Antarctica, Greenland, the Canadian Arctic Archipelago, and the Russian Arctic Islands are not represented in the dataset. Both the spatial coverage and temporal resolution of our dataset exhibit distinct temporal and regional patterns (Table 1). Three distinct phases characterize the temporal evolution of dataset coverage. Water years 2015 and 2016 had the smallest spatial coverage (~16 million km^2) and coarsest average temporal resolution (18.2 days). Water years 2017-2021 demonstrate substantially expanded spatial coverage (39.3-42.7 million km^2) and improved temporal resolution (8.2-9.5 days). Water years 2022-2024 exhibit intermediate spatial coverage (23.0-24.0 million km^2) and temporal resolution (8.7-10.9 days). Across all water years, the overall average global temporal resolution was 9.2 days, with the 10-year median runoff onset composite covering 43.7 million km^2.

Regional variations in temporal resolution are pronounced across the global domain (Figure 3.2, bottom). The finest 10-year median temporal resolution was observed over mainland Europe, with median temporal resolution of 4 days or better, improving to 2 days or better in northern Europe. In contrast, the worst temporal resolution is observed in northwest North America and northern Asia, with 10-year median temporal resolution of around 12 days. Most other global regions fall between these extremes, with 10-year median temporal resolution typically ranging from 6-10 days. The temporal resolution varies not only by region, but also locally within regions, reflecting both Sentinel-1 data availability as well as our pixel-wise processing methodology.

Table 3.1. Global snowmelt runoff onset dataset spatial coverage and average temporal resolution for each water year.

Water year	**Spatial coverage [km^2]**	**Average temporal resolution [days]**
2015	16,352,898	18.2
2016	16,140,507	18.2
2017	42,703,441	9.4
2018	39,708,851	9.5
2019	39,371,379	8.8
2020	40,497,938	9.0
2021	39,937,778	8.2
2022	23,781,413	9.8
2023	24,026,146	8.7
2024	22,973,905	10.9
10-year composites	43,725,005	9.2

3.5 DATASET EVALUATION

3.5.1 *Effects of forest cover fraction, temporal resolution, and maximum SWE*

The pixel-wise analysis reveals systematic relationships between environmental factors and agreement between our annual runoff onset products and snow pillow runoff onset estimates (Figure 3.3). The top row examines median differences of the residuals, and the bottom row median absolute deviation of the differences. These agreement metrics vary with temporal resolution (columns), forest cover fraction (x-axis), and maximum SWE accumulation (y-axis).

Increasing temporal resolution shows moderate but consistent effects on agreement. Both median absolute deviation and mean differences decrease with improving temporal resolution, indicating better agreement when SAR observations are more frequent. This effect is most pronounced between forest cover fraction of 0.4 and 0.7.

Maximum SWE accumulation also influences agreement, with generally smaller biases and lower spread in areas with higher snow accumulation. Agreement improves markedly above approximately 20-30 cm SWE for forest cover fraction below 0.5, with this SWE threshold increasing progressively with forest cover fraction.

Forest cover fraction emerges as the dominant control on agreement. Median absolute deviation increases substantially with forest cover fraction greater than 0.5, reaching 15-25 days in densely forested areas compared to 5-15 days in less densely forested areas. Similarly, median differences show increasing bias development with increasing forest cover fraction; for areas above 0.5 forest cover fraction, annual runoff onset products indicate runoff onset predominantly 5-20 days early relative to snow pillow estimates of runoff onset, as opposed to less densely forested areas with biases of less than 5 days.

Based on these empirical results, we limited the analysis to pixels with a forest cover fraction of at most 0.5, a temporal resolution of at most 14 days, and a maximum SWE accumulation of at least 20 cm in the station-level evaluation that follows.

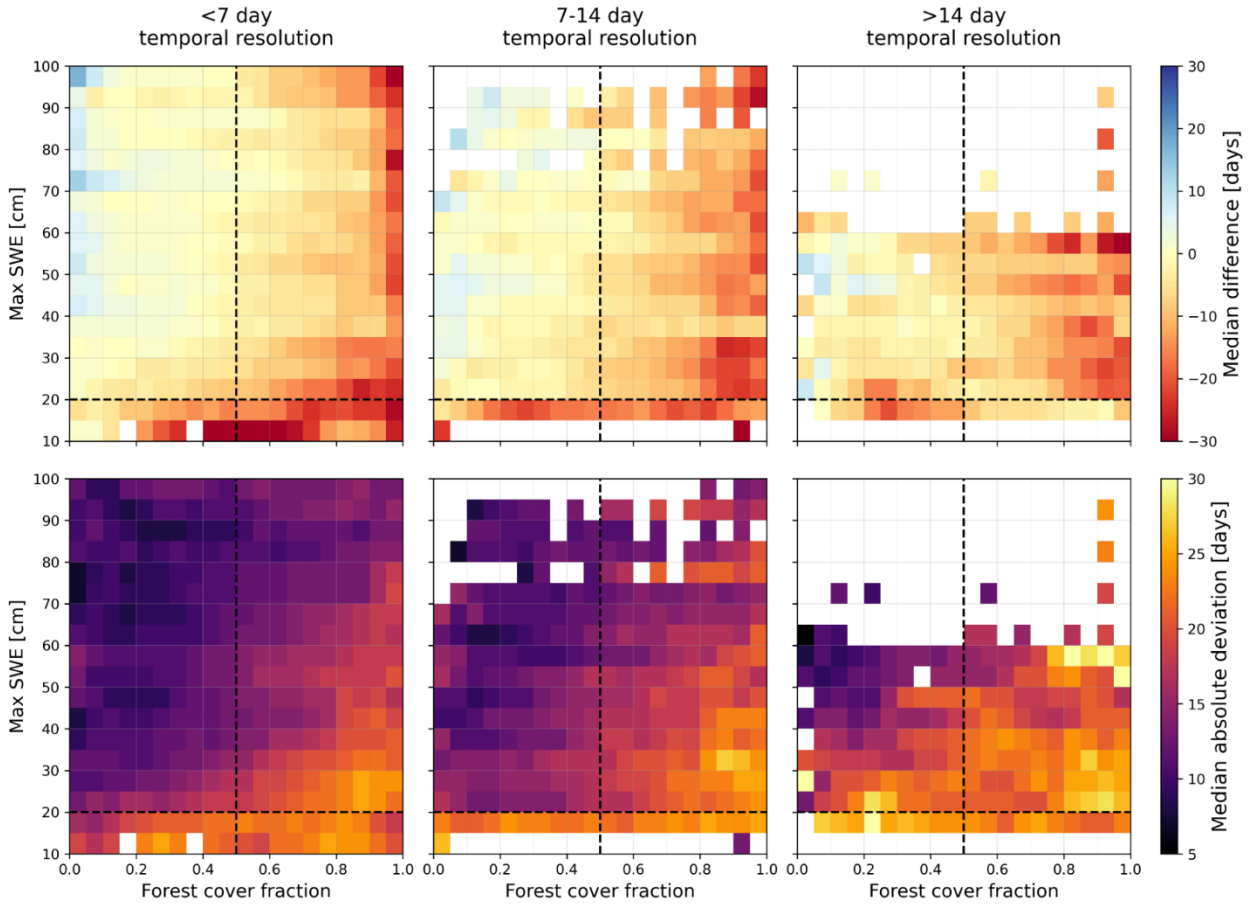

Figure 3.3. Snowmelt runoff onset detection performance as a function of temporal resolution and environmental controls, Median difference of residuals (our product minus snow pillow) on the top row, and median absolute deviation of residuals on the bottom row. Performance metrics are binned and shown for different combinations of forest cover fraction (x-axis), maximum SWE accumulation (y-axis), and temporal resolution (columns: >7 days, 7-14 days, >14 days). Note performance degradation at forest cover fraction values >0.5 (vertical dashed lines), maximum SWE accumulation <20 cm (horizontal dashed lines), and temporal resolution coarser than 14 days (third column). Please see Figure B.6 for an additional row showing pixel counts per bin.

3.5.2 *Automatic weather station validation results*

Our validation between our annual runoff onset products and snow pillow runoff onset estimates across the Western U.S. revealed generally good agreement with notable temporal and spatial patterns (Figure 3.4). Across all water years, we found a median difference (our product minus snow pillow) of -1.0 days and a median absolute deviation of 9.0 days, indicating minimal systematic bias and 50% of residuals falling within approximately 9 days, which is on the same order as the temporal resolution.

The distribution of residuals showed substantial improvement over the study period (Figure 3.4, left). Though bias remained relatively low throughout (highest bias of 4 days in both 2017 and 2018), early years with poor temporal resolution (>~10 days) exhibited a larger spread in residuals, with respective median absolute deviation values of 14.5 days for water year 2015, and 13.0 days for water year 2016. The distribution of residuals was tighter with improved temporal resolution, throughout water years 2017 to 2021 (4.1-5.6 days), with median absolute deviation values between 7.0 and 12.0 days. From water year 2022 onward, with average temporal resolution of 7.3-7.9 days, the distribution of residuals widened, with median absolute deviation values ranging from 7.0 to 13.0 days.

Spatial patterns in timing differences revealed distinct regional biases (Figure 3.4, right). Stations with the largest bias, where estimates from our products occurred up to 30 days earlier than snow pillow estimates, were observed in the southern Rocky Mountains east of the continental divide, where dense forest cover coincides with lower SWE accumulation. Conversely, stations with limited bias, where 50% of estimates from our products fell within 7 days of snow pillow estimates, were located in less densely forested regions with higher SWE accumulation, such as parts of the Sierra Nevada and the southern Rockies west of the continental divide.

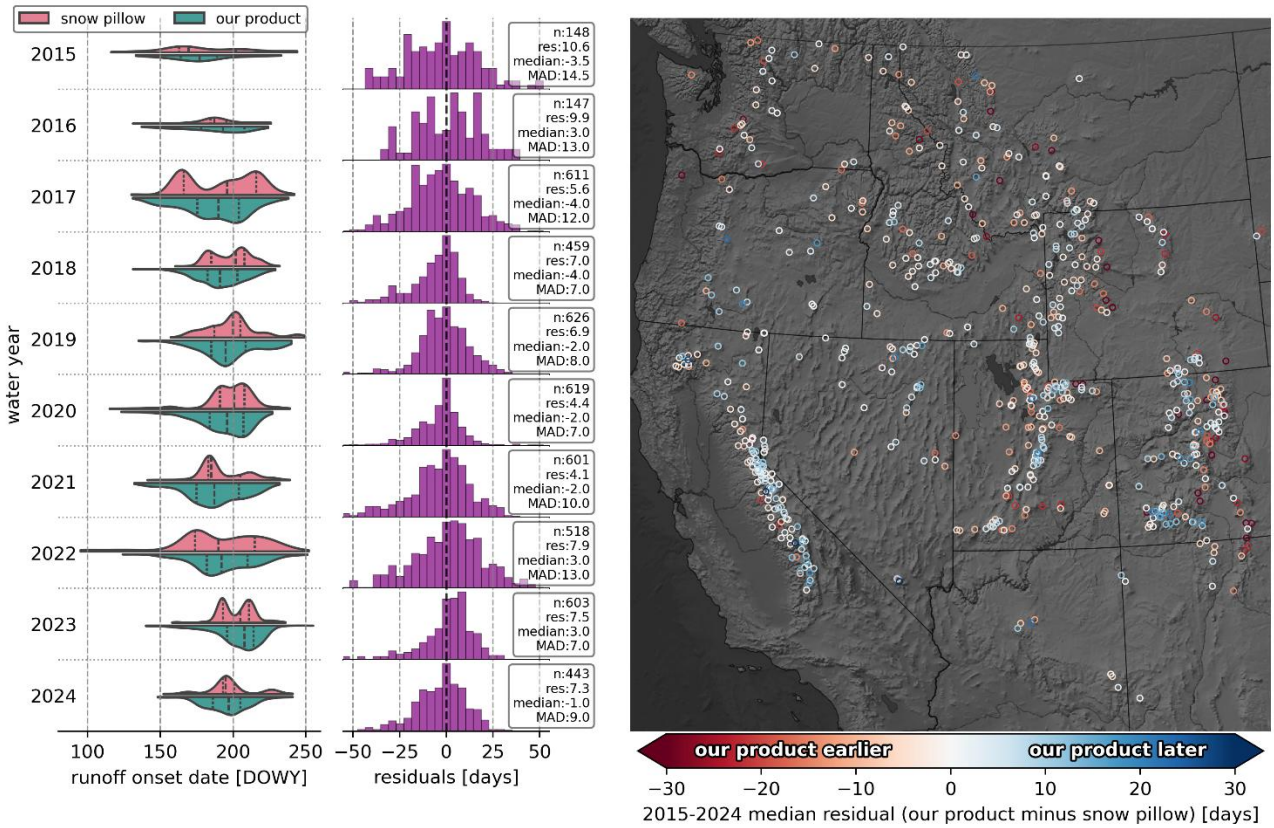

Figure 3.4. Validation of our snowmelt runoff onset products with 735 available automated weather station snow pillow observations for the 2015 to 2024 period. (Left) Distribution of all directly comparable snowmelt runoff onset estimates for each water year. (Center) Accompanying histograms of residuals (our product minus snow pillow) for each water year. Text annotations show residual statistics: number of stations (n), approximate average temporal resolution of the estimates from our product (res), median of the residual values (median), and median absolute deviation of the residuals (MAD). (Right) Median of 2015-2024 residuals (our product minus snow pillow) for each station. At each station, positive values (blue) indicate that the estimate from our product usually occurs after the snow pillow estimate, and negative values (red) indicate the estimate from our product usually occurs before the snow pillow estimate.

3.6 DISCUSSION

3.6.1 *Variations in spatial and temporal coverage*

This global high-resolution dataset represents a significant advancement in snow hydrology monitoring, providing unprecedented spatial detail and temporal coverage across Earth's seasonal snow-covered regions. With 80 meter resolution, it bridges a critical observation gap between coarse passive microwave products (typically ~25 km) and sparse point scale (~3 m) in-situ networks (1 station per ~1280 km^2 in mountain regions of the Contiguous Western U.S.), while offering a consistent, reproducible methodology applied globally over a decade-long record.

Though a comprehensive scientific analysis of the global dataset is presented in complementary manuscripts, preliminary examination of the dataset reveals coherent geographic patterns consistent with theoretical expectations of snowmelt across diverse snow environments. Across all continents and latitudes, we observe relatively smooth elevation gradients in snowmelt onset timing–the earliest snowmelt runoff onset occurs at lower elevations, with runoff onset occurring progressively later at higher elevations.

However, dataset spatial coverage and temporal resolution vary systematically across space and time due to the evolving Sentinel-1 constellation and the European Space Agency's observation priorities. The 10-year median temporal resolution composite (Figure 3.2, bottom) shows how typical temporal resolution varies from the most frequently observed regions (2-4 days in mainland Europe) to the least frequently observed regions (12+ days in northwest North America and northern Asia). Similarly, dataset spatial coverage and temporal resolution vary by water year, with three distinct temporal phases reflecting key constellation milestones. Water years 2015-2016 represent the early single-satellite period with Sentinel-1A alone, resulting in limited global coverage and coarse temporal resolution. Water years 2017-2021 coincide with the two-satellite constellation following Sentinel-1B's launch in April 2016, enabling more frequent observations that substantially improved spatial coverage and temporal resolution. Water years 2022-2024 reflect single-satellite observations after Sentinel-1B's failure in December 2021, though spatial coverage and temporal resolution remain significantly better than the initial period due to

modifications to the observation plan of Sentinel-1A made to compensate for the loss of Sentinel-1B (Potin et al., 2022).

As we'll demonstrate in the following sections, these variations in temporal resolution interact with forest cover and snow accumulation to create complex patterns of dataset performance at the pixel scale. We first characterize these pixel-scale environmental controls on dataset performance, and then use these empirical thresholds to appropriately filter station-level validation and ultimately inform practical recommendations for optimal dataset application across different environmental conditions.

3.6.2 *Environmental controls and dataset limitations*

Several important limitations affect the interpretation and application of this dataset. The physical interpretation of SAR backscatter minima can be complex in certain environments, particularly where backscatter change may not be fully attributable to snowmelt dynamics. When pixels contain mixed land cover types–including snow, vegetation, bare ground, structures, or other features–the SAR backscatter may be dominated by non-snow scatterers rather than the snowpack itself, especially for shallow or patchy snow cover. This challenge is most pronounced in forested regions, where C-band SAR represents an integrated response from the forest canopy, the underlying snowpack, and ground surface (Bonnell et al., 2024; Gao & Ma, 2024).

Accordingly, our systematic analysis of environmental factors found forest cover fraction as the dominant control on dataset performance, with greater forest cover fraction showing progressively degraded accuracy. This performance relationship exhibits an approximate inflection point around a forest cover fraction of 0.5, below which runoff onset estimation agreement remains relatively stable (median absolute deviations below 14 days with minimal bias), and above which estimation agreement degrades rapidly. Notably, other SAR-based analyses of snow, such as ΔSWE estimation from L-band InSAR (Bonnell et al., 2024) and snow depth estimation from C-band volume scattering (Hoppinen et al., 2024), also observe inflection points in performance around forest cover fraction of 0.5, suggesting that this threshold may represent a fundamental physical boundary for SAR penetration through forest canopies to underlying snowpack, for 1-5 GHz frequencies (5-25 cm wavelengths). For pixels with forest cover fraction above 0.5, the annual

runoff onset products tend to indicate runoff onset 5-20 days earlier than snow pillow estimates. This systematic early bias occurs because dense forest canopies fundamentally limit C-band SAR penetration to the underlying snowpack, causing changes in the backscatter time series to be dominated by changes in the C-band radar interactions with the canopy due to forest disturbance and canopy structural change (Kurum, 2015), tree sway (Raleigh et al., 2022), tree temperature (Bonnell et al., 2024; Lemmetyinen et al., 2022), tree water content (Steele-Dunne et al., 2012), and potentially intercepted snow melting in the canopy (Bonner et al., 2022). These canopy interactions represent a physical limitation of C-band SAR for snowmelt runoff onset detection in densely forested environments. Beyond C-band SAR interactions with the forest canopy, it is also possible that areas with dense forest cover and warmer winters also lead to more frequent winter melt, further complicating runoff onset identification (Lundquist et al., 2013). Forest cover fraction can help identify areas with dense forest cover, but cannot capture the full complexity of SAR interactions with the canopy and underlying snowpack. Factors such as canopy structure, tree species composition, branch density, and vertical canopy heterogeneity all influence C-band SAR interactions with the canopy, but are not represented in simple forest cover fraction metrics.

We found that maximum SWE accumulation also represented an important control on dataset performance. The environmental controls analysis revealed that runoff onset estimate agreement between our dataset and in-situ snow pillows improves dramatically above ~20 cm of maximum SWE for pixels with forest cover fraction below 0.5, with this threshold increasing steadily as forest cover fraction increases. For forest cover fraction below 0.5 and maximum SWE between 10-20 cm, we found poor performance, with bias approaching 30 days and median absolute deviation of up to 21 days. For the same forest cover fraction and maximum SWE between 30-40 cm, biases decrease to near 0, median absolute deviation is reduced to less than 7 days. Though dataset performance improves with maximum SWE values further beyond ~20 cm, it does so more gradually. While snow pillow performance itself may degrade below ~20 cm of SWE when no longer thermally insulated by overlying snowpack (Johnson & Schaefer, 2002), the observed dataset performance degradation with less than ~20 cm of SWE also reflects genuine physical controls of SAR detection capability.

The physical mechanisms underlying this apparent SWE threshold are complex. Fundamentally, detection of snowmelt runoff onset depends whether the associated characteristic backscatter minimum can be identified from the background backscatter variability: that is, whether the backscatter drop during runoff onset exceeds the dry-snow background backscatter variability. The underlying ground surface properties, particularly soil moisture and surface roughness, serve as the primary backscatter source when a snowpack is dry (Mätzler, 1987; Nagler et al., 2016). Stronger ground surface backscatter during dry-snow conditions results in a more pronounced backscatter minimum when the snowpack transitions to runoff onset, as backscatter absorption due to meltwater presence reduces the penetration depth, eliminating the backscatter contribution of the ground surface. Deeper snowpacks with greater SWE contribute additional dry-snow backscatter through enhanced volume scattering (Brangers et al., 2024), increasing the dry-snow backscatter and subsequently increasing the backscatter contrast during runoff onset. Additionally, shallower snowpacks with lower SWE have less cold content and experience more frequent melt-refreeze events, complicating identification of runoff onset. Interestingly, limited C-band penetration depth in wet snow suggests that total snow depth beyond ~5-10 cm should not directly influence the backscatter response once the surface is wet (Lund et al., 2020; Nagler, 1996). Yet deeper snowpacks consistently show improved snowmelt runoff onset detection in our environmental controls analysis, indicating that SWE likely serves as a useful proxy for environmental conditions that influence the identification of the characteristic backscatter minimum. In this context, improved dataset performance with greater SWE likely represents the combined effect of poorer dataset performance in shallow snowpacks with little cold content, as well as improved performance in deep snowpacks with greater backscatter contrast between dry-snow and runoff onset due to enhanced dry-snow volume scattering contributions. Finally, the observed dependence of the SWE threshold on forest cover fraction also supports this signal-to-noise interpretation: dense forest canopies introduce additional background backscatter variability, requiring progressively more dramatic backscatter decreases during runoff onset to produce a detectable backscatter minimum above the background backscatter variability.

Temporal resolution affected performance as well: both median absolute deviation and mean differences decreased as observation frequency improved. This relationship represents the challenge that, especially during rapid snowmelt transitions, low observation frequency may not

capture the characteristic SAR backscatter minimum. The effect of temporal resolution was most pronounced for pixels with forest cover fraction between 0.4 and 0.7, with median absolute deviation improving from 21 days for pixels with 23-26 day temporal resolution, to 14 days for pixels with 11-13 day temporal resolution. This relationship holds for forest cover fraction below 0.4, albeit weaker in strength. Beyond forest cover fraction of 0.7, the median absolute deviation of runoff onset estimates were within 21 days for pixels in both the 23-26 day and 11-13 day temporal resolution regimes, but decreased to 14 days for pixels in the 3-8 day temporal resolution regime.

Besides the effect of improved observation frequency, pixels with higher temporal resolution likely benefit from the aggregation of multiple viewing geometries in our methodology, as they tend to have coverage from multiple individual relative orbits. This might explain how the most densely forested areas with forest cover fraction exceeding 0.7, despite the fact that SAR backscatter is likely dominated by canopy effects, still show improvement in median absolute deviation from 21 days to 14 days from the 23-26 day and 11-13 day temporal resolution regimes to the 3-8 day temporal resolution regime. Different SAR viewing geometries interact with forest canopies and underlying snowpack at varying incidence angles, potentially allowing some geometries to achieve better penetration through canopy gaps or reduced canopy interference compared to other viewing geometries. In other words, areas with high temporal resolution, which benefit from both high observation frequency and multiple viewing geometries, enable the dataset to maintain reasonable performance even in challenging densely forested environments.

While we have discussed interactions between these factors throughout this section, it is worth emphasizing how these environmental controls interact to create compounding effects on dataset performance. Areas with the combination of poor temporal resolution, low maximum SWE, and high forest cover fraction represent the most challenging conditions for reliable snowmelt runoff onset detection, often resulting in median absolute deviation exceeding 30 days. Conversely, the dataset achieves optimal performance in areas with temporal resolution of 14 days or better, adequate snow accumulation above ~20 maximum SWE, and forest cover fraction below 0.5, where median absolute deviation can approach the temporal resolution of the underlying observations. Importantly, even when one of these factors is sub-optimal–such as moderately high

forest cover but good temporal resolution and adequate snow accumulation, or low temporal resolution but sparse forest cover and adequate snow accumulation–the dataset typically maintains reasonable performance with median absolute deviation in the 7-14 day range.

Finally, the environmental controls examined here are not exhaustive, and other factors contribute to dataset performance, such as terrain complexity, snow grain size evolution, land cover type and change, soil moisture and roughness, and local meteorological conditions.

3.6.3 *Validation and comparison challenges*

Our comprehensive validation against over 900 automated weather stations across the Western United States demonstrates strong agreement between our product and in-situ estimates of snowmelt runoff onset. The overall performance metrics–a median difference of -1.0 days and a median absolute deviation of 9.0 days–indicate minimal systematic bias and that 50% of residuals fall within 9.0 days, which approaches the temporal resolution of the original Sentinel-1 observations.

The validation reveals clear temporal patterns demonstrating how performance depends on observation frequency. Water years 2015 and 2016, with poorer temporal resolution due to single Sentinel-1 satellite coverage, had a median absolute deviation of up to 14.5 days in water year 2015. Performance improved markedly in water years 2017-2021 during the period with two Sentinel-1 satellites, with median absolute deviations between 7.0 and 12.0 days. Though performance degrades again in water years 2022-2024 after the failure of Sentinel-1B in December 2021, more frequent and consistent coverage compared to the first period of single Sentinel-1 coverage gave way to median absolute deviation ranging from 7.0 to 13.0 days. This interannual evolution in performance suggests that outside of environmental conditions like forest cover fraction and SWE accumulation, dataset performance is largely constrained by observation frequency rather than fundamental methodological limitations.

The spatial distribution of validation residuals reveals systematic regional patterns that are consistent with our environmental controls analysis. Stations with the largest biases–where our

estimates occurred up to 30 days earlier than snow pillow estimates–were concentrated in the southern Rocky Mountains east of the continental divide, where dense forest cover coincides with moderate SWE accumulation. This regional clustering of poor performance reflects the compounding effects of challenging environmental conditions. On the other hand, regions showing minimal bias correspond to sparser forest cover and high SWE accumulation, confirming that the dataset performs well under the environmental conditions we identified. This validation demonstrates that while environmental factors do create systemic regional patterns in dataset performance, our empirically-derived thresholds provide effective guidance for identifying regions with optimal performance.

It is important to emphasize that both our product and snowmelt runoff onset estimates from snow pillow measurements detect snowpack-scale processes–when water drains from the snowpack rather than basin-scale streamflow response. The timing we report represents meltwater availability for subsurface infiltration and eventually streamflow contribution, not the arrival of water at stream gauges, which can lag by days to weeks depending on basin characteristics (Frisbee et al., 2011; Lowry et al., 2010).

However, fundamental differences between snowmelt runoff onset estimation approaches can introduce natural timing offsets that complicate comparisons of snowmelt runoff onset estimates–both measurement approaches detect different physical processes related to snowmelt runoff onset. Snow pillows measure mass change in the snowpack and can register SWE reductions from various processes that may precede or follow actual meltwater outflow, while our SAR methodology aims to identify a characteristic backscatter minimum associated with changes to liquid water content and snow surface roughness that accompany the transition to the runoff phase. For example, sublimation and wind redistribution can modify SWE without changing the liquid water content in a snowpack, potentially leading to snow pillows indicating earlier runoff onset than our product. Conversely, diurnal melt-freeze cycles, rain-on-snow events, and isolated warm periods may temporarily increase liquid water content and alter snow surface roughness before continuous runoff begins, potentially leading to our product indicating earlier runoff onset than the snow pillows. Though we make attempts in our SAR methodology to minimize these early false positive runoff onset estimates by searching only the latter half of the snow covered period in the

snow phenology dataset (Section 3.3.2.1), we cannot guarantee the removal of false positive runoff onset estimates later in the season.

Beyond these fundamental measurement differences, several methodological constraints introduce additional uncertainty into the validation effort. First, the different temporal sampling of the methods challenges intercomparison: the snow pillow measurements have daily intervals, while the SAR observations occur at intervals ranging from 6 to 24 days depending on the Sentinel-1 observation plan. In fact, this difference in temporal sampling manifests in the distribution of runoff onset estimates by water year (Figure 3.4, left). The bimodal distribution of daily snow pillow estimates resolve the influence of discrete synoptic-scale weather-related melt events in distinct Western U.S. maritime and continental snowmelt timing regimes (Musselman et al., 2021) in high fidelity, whereas the coarser and spatially varying temporal resolution of our product yield smoother aggregate distributions. Additionally, snow pillow measurement errors, such as meltwater pooling on the instrument surface, can also distort the timing of SWE reduction (Webb et al., 2017). Finally, snow pillow geolocation uncertainty and scale differences between point-based snow pillow measurements and the 80-meter SAR pixels within the 1000-meter station radius contribute to timing differences in the methods. Local spatial variability in SWE and snowmelt timing around these stations introduces uncertainty in representativeness, and can be substantial even over short distances (Meromy et al., 2013). However, statistical aggregation over a total of 4,763 water years across 735 stations ensures that these local-scale mismatches do not compromise the overall conclusions of the validation effort.

Despite these challenges, the strong overall agreement and dramatic improvement in performance coinciding with increased temporal resolution, suggests that the dataset's performance is primarily constrained by observation frequency rather than fundamental methodological issues.

3.6.4 *Recommendations for dataset users*

Though we discuss the environmental controls analysis more rigorously in Section 3.6.2, here we provide brief takeaways and recommendations for dataset users. Our analysis identified three

primary controls on dataset performance: forest cover fraction, maximum SWE accumulation, and temporal resolution. These controls all interact to create compounding effects on performance.

For optimal performance, users should focus on areas where forest cover fraction remains below 0.5, maximum SWE accumulation exceeds ~20 cm, and temporal resolution is 14 days or better. Under these combined conditions, the dataset agrees with snow pillow reference measurements, with 50% of residuals falling within 7 days and near-zero systematic bias. When only one of these factors is sub-optimal, such as moderately dense forest cover but with high SWE accumulation and 7-day temporal resolution, the dataset typically maintains reasonable performance with median absolute deviation of 7-14 days and biases of up to 7 days. However, users should avoid using this dataset in areas where multiple challenging conditions coincide, particularly in areas that have dense forest cover, low SWE accumulation, and low temporal resolution, as median absolute deviation and bias can both approach 30 days. Users should consider the local temporal resolution when interpreting snowmelt runoff onset dates, shown in Figure 3.2 or Figure B.1 and available as a variable in the dataset. For expected agreement relative to snow pillow reference measurements given environmental conditions, users should consult Figure 3.3.

We implemented these recommendations in our validation study, and found that a majority of our estimates matched the snow pillow estimates to within 9 days or less. Even with such performance, some densely forested regions still showed strong biases, such as in the southern Rocky Mountains east of the continental divide, where dense forest cover, despite masking, combined with low SWE accumulation to create unfavorable conditions.

Additionally, in extreme high-elevation regions above 5000 m (~5% of our dataset), particularly in the tropical Andes and parts of High Mountain Asia, sublimation can often surpass snowmelt as the primary snow ablation mechanism (Ayala et al., 2023; Gascoin et al., 2013; Réveillet et al., 2020). The physical interpretation of backscatter minima in sublimation-dominated environments remains poorly understood, so we caution the use of this dataset in such locations, especially if site-specific validation is not possible.

Our snow phenology dataset inherits known MODIS snow product limitations, including false positive snow presence identification near turbid water bodies (e.g., on the Tibetan Plateau), over salt flats (e.g., in the Atacama Desert), and in regions with persistent cloud cover where cloud-snow misclassification is common (e.g., the eastern slopes of the tropical Andes) (Hall & Riggs, 2021; Saavedra et al., 2017). These inherited false positive snow presence values can cause our algorithm to search for runoff onset where no snowpack existed, resulting in spurious estimates in the final dataset.

Finally, users should recognize that reported snowmelt runoff onset timing represents a characteristic runoff onset event rather than a comprehensive description of complex snowmelt dynamics. The episodic nature of snowmelt processes means snowpacks often cycle repeatedly between phases during dynamic snowmelt conditions, potentially leading to multiple discrete instances of runoff onset in a single season (Dingman, 2015; Lund et al., 2022). Despite such dynamic melt seasons, our approach leverages a median aggregation of runoff onset estimates from multiple individual relative orbits, which provides robustness against such variability.

3.6.5 *Applications and future work*

This dataset enables diverse applications across multiple disciplines. The high-resolution onset timing products can provide critical retrospective information on the location and timing of snowmelt for hydrological applications. This information can enable the study of the relationship between the distribution of snowpack properties (e.g. snow depth and SWE) and runoff timing and volume, which could ultimately enhance streamflow forecasting, especially in snow-dominated watersheds and watersheds lacking in-situ observations.

We demonstrate the dataset's scientific potential through companion research that examines systematic relationships between geographic, topographic, and climatic factors, governing snowmelt timing across diverse mountain environments, providing insights into the fundamental drivers of global snowmelt variability. Additional companion analysis assesses global population exposure to snowmelt timing variability through basin-scale evaluation of runoff onset timing

anomalies across snow-dependent watersheds worldwide, revealing populations most vulnerable to changing snowmelt patterns under climate change.

This decade-long dataset also offers broader insights into the spatial and temporal variability in snowmelt timing, which represents a sensitive indicator of climate change impacts in mountain environments. As the satellite record continues, researchers can analyze longer-term trends in snowmelt timing, as well as the relationships between snowmelt patterns and improved climate forcing data, potentially revealing teleconnections between large-scale atmospheric patterns and regional snowmelt dynamics. The capability of this dataset to detect anomalously early or late melt timing makes it particularly valuable for examining snowmelt responses to climate anomalies.

More specialized applications include quantifying differences in snowmelt timing between burned and unburned areas to understand wildfire effects on snow hydrology (Rickenbaugh, 2023), examining the influence of light-absorbing particles and radiative forcing on spatial patterns of snowmelt timing (Skiles et al., 2018), quantifying the effect of forest properties on snowmelt timing (Lundquist et al., 2013), and examining the phenological responses to snowmelt across complex mountain terrain (John et al., 2020; Matias et al., 2024). Additionally, from a methodological perspective, our dataset could both enhance snowpack and hydrological model performance in data assimilation systems (Mirza et al., 2025), and help define the optimal spatial and temporal windows for reliable snow property retrievals for other remote sensing methods, including Sentinel-1 volume scattering methods for snow depth estimation (Hoppinen et al., 2024; Lievens et al., 2022), as well as ΔSWE estimation from L-band InSAR, such as the upcoming NISAR mission (Alabi et al., 2025; Bonnell et al., 2021; Palomaki & Sproles, 2023; Tarricone et al., 2023).

Future improvements in the temporal and spatial coverage of satellite SAR measurements could improve the quality and coverage of future datasets based on the methodology described in this paper. The recent launch of Sentinel-1C in December 2024 restored the Sentinel-1 constellation to two operational satellites, and Sentinel-1D is scheduled to launch in November 2025, improving temporal resolution for future water years. The recently launched L-band NISAR mission offers potential to extend snowmelt detection beneath dense forest canopies due to greater penetration

through vegetation than the C-band Sentinel-1 data. Though limited by proprietary data policies and spatial coverage, rapidly expanding commercial SAR constellations have the potential to provide sub-daily revisit capabilities, which could enable even more precise estimation of snowmelt runoff onset.

These advances in satellite SAR, combined with continued algorithm refinements and expanded validation efforts across different geographic regions and climate zones, will enhance future dataset versions and expand its applicability to an even wider range of environments and applications.

3.7 DATA AVAILABILITY

The global snowmelt runoff onset dataset is available from: [10.5281/zenodo.16953615], and the software used to generate it is available from: [https://github.com/egagli/global_snowmelt_runoff_onset]. The snow phenology dataset is available from: [https://doi.org/10.5281/zenodo.17246166], and the software used to generate it is available from [https://github.com/egagli/MODIS_seasonal_snow_mask].

3.8 CONCLUSIONS

This global snowmelt runoff onset dataset provides the first comprehensive high-resolution characterization of snowmelt timing across Earth's seasonal snow-covered regions. By combining multiple orbital geometries of Sentinel-1 C-band SAR with a custom MODIS-derived snow phenology dataset, we developed a robust methodology for detecting the characteristic backscatter minimum associated with snowmelt runoff onset, producing a global 80 meter snowmelt runoff onset record spanning water years 2015 to 2024.

Comprehensive validation against over 900 automatic weather stations in the Western U.S. over a 10 year period confirmed the reliability of our methodology, with a median difference of -1.0 days, and a median absolute deviation of 9.0 days compared to in-situ snow pillow measurements.

Our systematic analysis of environmental controls established recommendations for applications of our dataset. Forest cover fraction emerged as a dominant control, with consistent performance below forest cover fraction of 0.5, but progressively poorer performance beyond this threshold. Maximum SWE accumulation proved a milder control, though we identified a critical threshold of ~20 cm of SWE accumulation, below which snowmelt runoff onset could not be reliably detected. Finally, we observed improved results in areas with better temporal resolution, especially in areas with higher forest cover fraction.

By making this dataset and associated tools publicly available, we aim to support a wide range of applications in hydrology, climate science, ecology, and water resource management. The methodological framework and empirically-validated performance recommendations established here provide guidance for appropriate dataset application and may inform future developments as satellite observing capabilities continue to expand. This decade-long record of snowmelt runoff onset contributes to the growing body of observations needed to better understand and monitor global snowmelt in an era of environmental change.

Chapter 4. GLOBAL PATTERNS AND CONTROLS ON MOUNTAIN SNOWMELT RUNOFF ONSET FROM A DECADE OF HIGH-RESOLUTION OBSERVATIONS

This chapter is in preparation for submission.

4.1 ABSTRACT

Seasonal snowmelt sustains over one billion people globally, yet our understanding of spatiotemporal variability of snowmelt and controls across Earth's diverse mountain regions has been limited by observational constraints. Here we present the first comprehensive global analysis of a snowmelt runoff onset dataset prepared from a decade (2015-2024) of Sentinel-1 synthetic aperture radar backscatter measurements. Through systematic continental-scale and local-regional analyses spanning 150 major mountain ranges, we quantify how elevation, aspect, latitude, and spring air temperature control snowmelt timing and its interannual variability.

We find that elevation gradients exhibit a median snowmelt runoff onset delay of 3.5 days per 100 m, with substantial variability across mountain ranges (-0.5 to 9.0 days/100 m), weakening toward polar latitudes. Differences in runoff onset timing between sunny and shaded areas follows a predictable seasonal modulation depending on latitude, with small differences before spring, increasing to maximum differences of 20-60 days in early- to mid-spring, and then diminishing thereafter. For individual mountain ranges, aspect control varies with climate and topographic characteristics, with some clear-sky, steep continental ranges in Western High Mountain Asia showing runoff onset timing differences of >40 days for variable aspect, but nearby cloudier ranges showing very low differences (<10 days). Interannual variability during the 10-year period is lowest (<15 days) in high-latitude ranges, but exceeds 30 days in the tropical Andes and eastern Tibetan Plateau, where highly variable synoptic patterns govern snow accumulation and melt. Spring air temperature sensitivity analysis reveals that 72% of mountain ranges show correlations of $|r|>0.4$ between temperature and annual runoff onset timing, with mid-latitude ranges exhibiting sensitivities of -8 to -13 days/°C while polar ranges show minimal temperature influence. These relationships demonstrate that snowmelt timing, despite its complexity, follows predictable physical controls that vary coherently across geographic and climatic gradients.

4.2 INTRODUCTION

4.2.1 *Snow and snowmelt*

Snow plays a crucial role in the global water cycle and climate system, and globally, more than one-sixth of the world's population relies on meltwater from seasonal snow and glaciers (Barnett et al., 2005). This dependence is particularly pronounced in mountainous regions, where seasonal snowpack acts as a natural reservoir, storing water as snow in the winter and gradually releasing it during spring and summer.

The timing and spatial distribution of snowmelt represent critical parameters in water resource management. In particular, snowmelt runoff onset initiates the annual spring pulse, marking the beginning of increased water availability that sustains downstream ecosystems and human water needs during the warmer months. Knowledge of when and where snowmelt occurs can inform more accurate predictions of runoff response, which is essential for flood forecasting, reservoir operations, and agricultural planning (Lundquist & Dettinger, 2005).

Beyond its hydrological significance, snowmelt timing also serves as a key indicator of regional climate change (Dudley et al., 2017). As a process highly sensitive to temperature and precipitation variations, shifts in snowmelt patterns provide tangible evidence of changing climate conditions, often manifesting before other environmental indicators become apparent. In recent decades, climate change has significantly impacted global snow accumulation and snowmelt patterns (Ismail et al., 2023; Royer et al., 2021; T. Yang et al., 2022). Though these specific patterns vary regionally, they have far-reaching consequences for water security, agricultural productivity, and ecosystem health in snow-dominated regions and beyond (Qin et al., 2022). Yet despite the importance of snowmelt timing, our understanding of its detailed global spatial and temporal variability remains limited due to observational constraints (Awasthi & Varade, 2021).

4.2.2 *Snowmelt timing*

Generally, snowmelt proceeds in three phases. First, during the warming phase, the energy inputs bring the snowpack to an isothermal state at the melting point. Once the snowpack is isothermal, the ripening phase begins, when energy inputs must provide sufficient energy to overcome the latent heat of fusion for the phase change from ice to water. The initial melt period creates complex, heterogeneous melt patterns, with water flowing laterally along layer boundaries and within vertical pipes, until a more homogeneous wetting front moves from the surface to the base of the snowpack (e.g. Eiriksson et al., 2013). Once the snowpack cannot retain any more liquid water, it is considered ripe, and any additional energy inputs lead to the beginning of the output phase, when water begins to leave the snowpack (Dingman, 2015). Though not exactly the same due to subsurface conditions, the onset of the output phase is often referred to as runoff onset (Boike et al., 2003). These delineations are a simplification, in reality a snowpack rarely progresses through these phases neatly due to cycles of melt and refreeze (DeBeer & Pomeroy, 2017; Dunne & Black, 1971).

Snowmelt timing is largely determined by the energy balance at the snow surface, which involves a complex interplay of energy fluxes, the most important of which are radiative fluxes and turbulent fluxes (Male & Granger, 1981). Radiative fluxes include both net solar radiation, which represents the balance of incoming solar energy and solar energy reflected by the snow surface, as well as longwave radiation exchanges, which represent energy emitted by the atmosphere and environment and the snow surface itself. Turbulent fluxes include both sensible heat exchange, which represents heat exchange due to temperature differences between the snow and air, as well as latent heat exchanges, which represent energy associated with the phase changes of water (Marks & Dozier, 1992). Less dominant, but sometimes still significant, are the ground heat flux and heat advection during precipitation (Mazurkiewicz et al., 2008). The magnitude and relative importance of these fluxes are influenced by meteorological conditions (e.g. air temperature, precipitation, humidity, and wind speed), geography (e.g. latitude, regional climate, topography, and vegetation), snowpack properties (e.g. microstructure, depth, density, temperature, and albedo), and time of year. Due to the wide distribution of these processes and characteristics, snowmelt timing can have high spatial and interannual variability (Kattelmann & Dozier, 1999; Marks et al., 1998; Mote, 2006).

4.2.2.1 Spatial variability

Spatially, snowmelt timing is influenced by geographic characteristics, such as latitude, regional climate, topography, and vegetation.

Latitude influences average air temperatures, the magnitude of solar radiation received, as well as the hours of daylight over which the solar radiation is received (Pohl et al., 2006). Therefore, lower latitudes generally experience earlier snowmelt due to warmer air temperatures, and stronger insolation as a function of sunlight hours and higher sun elevation angles during the melt season. Generally, at higher latitudes the energy for melt is predominantly provided by radiative fluxes, and at lower latitudes (especially in maritime environments) turbulent fluxes become more relevant (Zhang et al., 2001).

Regional climate is an important factor influencing snowmelt timing because it represents the typical meteorological conditions a snowpack experiences, such as average air temperature, precipitation, cloud cover, humidity, and wind speed (Lisi et al., 2015). For example, regions with more maritime climates might experience earlier snowmelt due to warmer temperatures and higher amounts of precipitation falling as rain (Jefferson, 2011).

Topography represents an intuitive control on snowmelt timing, with surface elevation often being the dominant influence in differential snowmelt timing across similar latitudes. This gradient in snowmelt timing is directly related to adiabatic lapse rates: lower elevations often experience earlier snowmelt due to warmer air temperatures, and higher elevations often experience later snowmelt due to colder air temperatures (Clow, 2010) and more exposure to wind. Beyond elevation, topography can affect snowmelt timing because of differential solar radiation received by different slopes and aspects, which varies by latitude and time of year (Garnier & Ohmura, 1968; Lundquist & Flint, 2006; Munro & Young, 1982). For example, in the northern hemisphere, south-facing aspects experience greater solar radiation (magnitude varying by time of year and local topography) compared to north-facing aspects, driving earlier snowmelt on south-facing aspects. Topography is also important to snowmelt timing due to its coupling with regional

climate, as weather patterns interact with topography leading to preferential accumulation and modification of local snow characteristics, which can display relatively consistent repeatability year-to-year (Litaor et al., 2008; Sturm & Wagner, 2010).

Land cover characteristics, particularly forest cover, influence snowmelt timing by modifying the snowpack energy balance: forest canopies reduce solar radiation received by the underlying snowpack, trees increase longwave radiation to the snowpack, and the lower wind speeds observed in forests reduce snowmelt due to turbulent fluxes (Strasser et al., 2011). Due to these competing effects of forest cover, higher forest density can cause earlier or later melt depending on factors such as average winter temperature and time of year of melt (Lundquist et al., 2013).

4.2.2.2 Interannual variability

While snowmelt timing is largely determined by geographic factors, interannual variability in snowmelt timing is primarily driven by fluctuations in winter and spring weather. Geography defines the potential window for snowmelt through its influence on solar radiation and sensible heat flux cycles, whereas year-to-year variations within this window are governed by synoptic-scale meteorology (Stewart, 2009; Zhang et al., 1996).

In the winter, synoptic-scale weather patterns cumulatively shape snowpack properties (i.e., depth, density, temperature, and albedo). These antecedent snowpack conditions influence snowmelt timing by modulating the snowpack energy balance and its response to spring energy inputs (Warren, 1982; Yamaguchi et al., 2004). Other environmental factors often affect snowpack conditions, such as rain-on-snow events and events that deposit light-absorbing particles (e.g., black carbon), which have both been shown to modulate snowmelt timing (Skiles et al., 2018; Z. Yang et al., 2023).

In the spring, snowmelt timing can be heavily influenced by synoptic-scale weather patterns, particularly with increased longwave radiation and turbulent heat fluxes associated with the advection of warm and wet air masses (Cayan et al., 1993; Iijima et al., 2007). The influence of synoptic-scale weather patterns can often overwhelm the geographic controls on snowmelt timing.

Lundquist et al. (2004) found that in the Sierra Nevada, synoptic weather patterns bring warmer than average winter temperatures and cooler than average March temperatures, leading to relatively synchronous snowmelt, largely independent of elevation and aspect. Zhang et al. (1996) found that even at arctic latitudes, synoptic-scale weather patterns bring cloudy conditions and increased atmospheric thickness (with accompanying longwave radiation), which can shift snowmelt up to a month earlier in the year.

However, the relationship between synoptic forcing and geographic controls is more complex than simple override. When strong synoptic forcing drives very early melt, particularly before the spring equinox when sun angles are low, topographic control on snowmelt timing can actually become more pronounced. Lundquist & Flint (2006) demonstrated this during an unusually warm early-March melt event in 2004, when north-facing basins in the Sierra Nevada experienced snowmelt onset delays of up to four weeks later compared to sun-exposed basins. Despite uniformly warm temperature, this enhanced topographic timing difference occurred because low sun angles during early-March led to larger relative differences in solar radiation received across the mountain range (Lundquist & Flint, 2006). During years without strong synoptic-scale forcing, geographic controls reassert their influence through more typical seasonal progression, with adiabatic lapse rates becoming particularly important in causing lower elevations to melt first (Lundquist et al., 2004). These synoptic weather patterns are closely related to climate modes, and many previous studies have shown that climate indices can explain moderate variability in snowmelt timing (Tedesco et al., 2009; Vicente-Serrano et al., 2007; Zheng et al., 2022).

The relative importance of different energy balance components also varies seasonally, with changing radiation inputs, temperature patterns, vegetation, and snowpack properties shifting dominant energy balance terms (Baldocchi et al., 1997; Gnann et al., 2025). Snowmelt timing exhibits greater interannual variability in regions with earlier melt, lower latitudes, and more maritime climates. This is largely due to average warmer air temperatures as well as the profound influence of highly variable synoptic-scale weather patterns in these areas, contrasting with the relative consistency of annual cycles of solar radiation (Mioduszewski et al., 2015; Moore & Owens, 1984; Zhang et al., 2001). For snowpacks that survive later in the season, when the sun is higher in the sky and the intensity of synoptic-scale weather patterns in snow-covered areas tend

to diminish, the importance of insolation increases (Leathers & Robinson, 1997; Ohmura, 2001). It follows then that regions with lower synoptic-scale variability and regions with snowpacks that last later into the year should show more consistent geographic influence on snowmelt timing.

4.2.2.3 Longer term trends

Long-term observational studies have documented trends toward earlier snowmelt. For example, a global study of ~25 km resolution passive microwave remote sensing data from 1979 to 2018 found that on average, melt onset in the northern hemisphere progressively occurred earlier in the year, at a rate of 4 days per decade (Zheng et al., 2022). Further, a study of weather stations in the Western US found a trend toward earlier peak snow water equivalent (SWE) timing, with an average shift of 7 days earlier in the year from 1982 to 2023 (Evan, 2019; U.S. Environmental Protection Agency, 2024). And looking forward, the snowmelt timing of the Western US is projected to occur earlier in the year by up to 1 month by 2050 (Barnett et al., 2005; Stewart, 2009).

However, these trends are not uniform across regions and topography (Gnann et al., 2025). For instance, Musselman et al. (2021) found that in Western North America, trends toward increasing winter melt occurred most often at middle to higher elevations, but less so at lower elevations, especially in the Pacific Maritime regions. In Central Asia, Tomaszewska & Henebry (2018) documented trends towards earlier snowmelt occurring primarily below 3400 m in Kyrgyzstan. Lundquist & Flint (2006) found that shifts towards earlier melt may amplify spatial variability in snowmelt timing, as melt occurring when sun angles are lower can increase the importance of aspect and slope in controlling differential snowmelt rates across complex terrain. All of these nuanced relationships demonstrate the need for long-term observations of snowmelt variability with a resolution high enough to resolve hillslope scale processes (<100 m)

The implications of earlier snowmelt extend beyond simple shifts in timing (Han et al., 2024). Siirila-Woodburn et al. (2021) found that changes in snowmelt timing in the Western US will lead to a corresponding snowpack loss, projected to be roughly equivalent to a 25% decrease in streamflow from snowmelt by 2050. As both snowmelt magnitudes decrease and snowmelt timing

shifts earlier, populations dependent on snowmelt meltwater will become increasingly vulnerable to reduced meltwater availability and droughts (Livneh & Badger, 2020).

4.2.3 *Sentinel-1 SAR global snowmelt runoff onset dataset*

Despite decades of research and numerous regional studies, fundamental questions about global snowmelt runoff onset patterns remain unanswered. Most studies have focused on individual mountain ranges or regions, with variable data sources and methodology. While valuable for local needs, they are difficult to compile, limiting our understanding of how runoff onset varies systematically across the Earth's mountain ranges.

Traditional observation approaches make global analysis challenging. In-situ measurements provide valuable point data but lack standardization and the spatial coverage necessary for global analysis. These observations are also indirect, as typically decreasing SWE is used as a proxy for snowmelt onset. Modern optical satellite remote sensing has global coverage and high resolution, but suffers from persistent cloud cover during critical melt periods and typically measures changes in snow cover, rather than direct measurements of runoff onset. Passive microwave remote sensing provides global coverage and more direct measurements of melt, but the spatial resolutions are too coarse to capture snowmelt variability in complex mountain terrain (Mioduszewski et al., 2015).

Recent advances in synthetic aperture radar (SAR) remote sensing now enable global snowmelt monitoring at high spatial and temporal resolution. SAR is capable of imaging in all weather and illumination conditions, while its sensitivity to liquid water allows detections of the transition from snow ripening to runoff phases through characteristic backscatter patterns at C-band (Darychuk et al., 2023; Gagliano et al., 2023; Marin et al., 2020). The European Space Agency's Sentinel-1 constellation provides global systematic C-band SAR with typical revisits intervals of 6-12 days.

Here, we use a new global dataset of snowmelt runoff onset timing derived from a decade of Sentinel-1 C-band backscatter observations (2015-2024) (**10.5281/zenodo.16953615**) to provide the first comprehensive analysis of global snowmelt timing patterns and associated controls. We first characterize continent-scale global snowmelt runoff onset patterns and interannual variability

across all seasonal snow-covered areas, and then focus on quantifying elevation, aspect, and temperature controls for all snow-covered mountain ranges on Earth.

4.3 METHODS

4.3.1 *Preprocessing the global snowmelt runoff onset dataset*

We utilized a global snowmelt runoff onset timing dataset derived from Sentinel-1 SAR observations spanning water years 2015-2024, which provided annual runoff onset dates at 80-m spatial resolution and a global median temporal resolution of 9.3 days (**10.5281/zenodo.16953615**). All runoff onset dates are expressed as day of water year (DOWY), with water years beginning October 1st in the northern hemisphere and April 1st in the southern hemisphere.

We applied forest cover masking using the Forest Cover Fraction variable of the 100 m Land Cover 2015-2019 (version 3) dataset from Copernicus Global Land Service (Buchhorn et al., 2020), excluding pixels with >50% forest cover based on empirically derived performance recommendations from the companion paper (**10.5281/zenodo.16953615**). To reduce the influence of pixels with false positive seasonal snow identification and accompanying timing (including those caused by clouds, salt flats, and edges of water bodies), we use the ~300 m Global Seasonal-Snow Classification (version 1) dataset (Sturm & Liston, 2021) to remove pixels without previously documented seasonal snow from our analysis.

4.3.2 *Continental-scale analysis*

We aggregated the snowmelt runoff onset dataset using latitude-elevation binning, with latitude bin widths of 1° and elevation bin widths of 100 meters. To assess typical snowmelt runoff onset timing and its interannual variability within each bin, we calculated mean values of the 10-year median runoff onset timing and 10-year runoff onset median absolute deviation for each bin containing at least 1000 pixels.

To analyze the timing differences between sunny and shaded areas, we used the Global SRTM Continuous Heat-Insolation Load Index (CHILI), which quantifies insolation effects by modeling early afternoon sun altitude and equinox conditions (Theobald et al., 2015). Based on empirical thresholds provided in Theobald et al. (2015), we classified pixels as warm (CHILI>0.767), cool (CHILI<0.448), or neutral (0.448<CHILI<0.767). To understand differences in timing between sunny and shaded areas within each bin, we calculated the median timing difference between each bin's warm and cool CHILI pixels, when minimum sample sizes of 1000 pixels were available for each thermal category. To analyze the seasonal evolution of these sunny-shaded timing differences, we compared each bin's warm-cool timing difference as a function of the bin's median runoff onset timing.

4.3.3 *Mountain range analysis and temperature sensitivity*

We focused our range-scale analysis to 291 non-overlapping major mountain ranges that cover approximately ~20% of the global land area excluding Antarctica, as defined by the Global Mountain Biodiversity Assessment (Snethlage et al., 2022). From these mountain ranges, we selected those with sufficient data (at least 500 m of relief, valid data for at least 5 water years), yielding 150 mountain ranges.

For each range, we calculated five primary metrics: (1) "snowmelt runoff onset lapse rate" using linear regression of 10-year median runoff onset timing vs elevation (days of melt delay per 100 m elevation gain), (2) "aspect control" as the timing difference between a specific aspect-elevation bin median timing and its respective elevation band median timing, (3) "interannual variability" as the 10-year median absolute deviation of runoff onset timing, (4) "annual timing anomaly" as the mountain-range mean of per-pixel annual deviation from the 2015-2024 median, and "runoff onset spring temperature sensitivity," described in the following paragraph.

We used monthly 2-meter air temperature data from ERA5-Land reanalysis (Muñoz, 2019) at 0.1° resolution (~10 km at the equator), calculating spring-season averages (March-May for the northern hemisphere, September-November for southern hemisphere) and annual spring temperature anomaly relative to the 2015-2024 median for each mountain range.

We then analyzed the relationship between the average spring temperature anomaly and average runoff onset timing anomaly for each mountain range. For mountain ranges with at least 5 years of data, we used linear regression to assess temperature sensitivity (days early/late per 1°C warming) and computed the Pearson correlation coefficient (r) to assess correlation strength.

4.4 RESULTS

4.4.1 *Global patterns of runoff onset vs. latitude and elevation*

The 10-year median snowmelt runoff onset product reveals coherent global spatial variability associated with latitude and elevation (Figure 4.1, top). Snowmelt timing progresses systematically from early season melt at lower latitudes and elevations to late season melt at higher latitudes and elevations. In the Northern Hemisphere, the earliest median runoff onset (DOWY 120-150) occurs in mid-latitude maritime mountain ranges at low elevations, while the latest runoff onset (DOWY 250-280) occurs in continental mountain ranges and polar regions.

Interannual variability, captured by the 10-year runoff onset median absolute deviation (MAD) product, shows distinct geographic clustering (Figure 4.1, bottom). The regions with the lowest interannual variability (<15 days) include North Asia, West Asia, and Europe, and the regions with the highest interannual variability (>25 days) are concentrated in the tropical and sub-tropical Andes, and the northern Tibetan Plateau including the Kunlun, Qilian, Altyn Tagh, Qiangtang, Bayan Har, and Tanggula mountains.

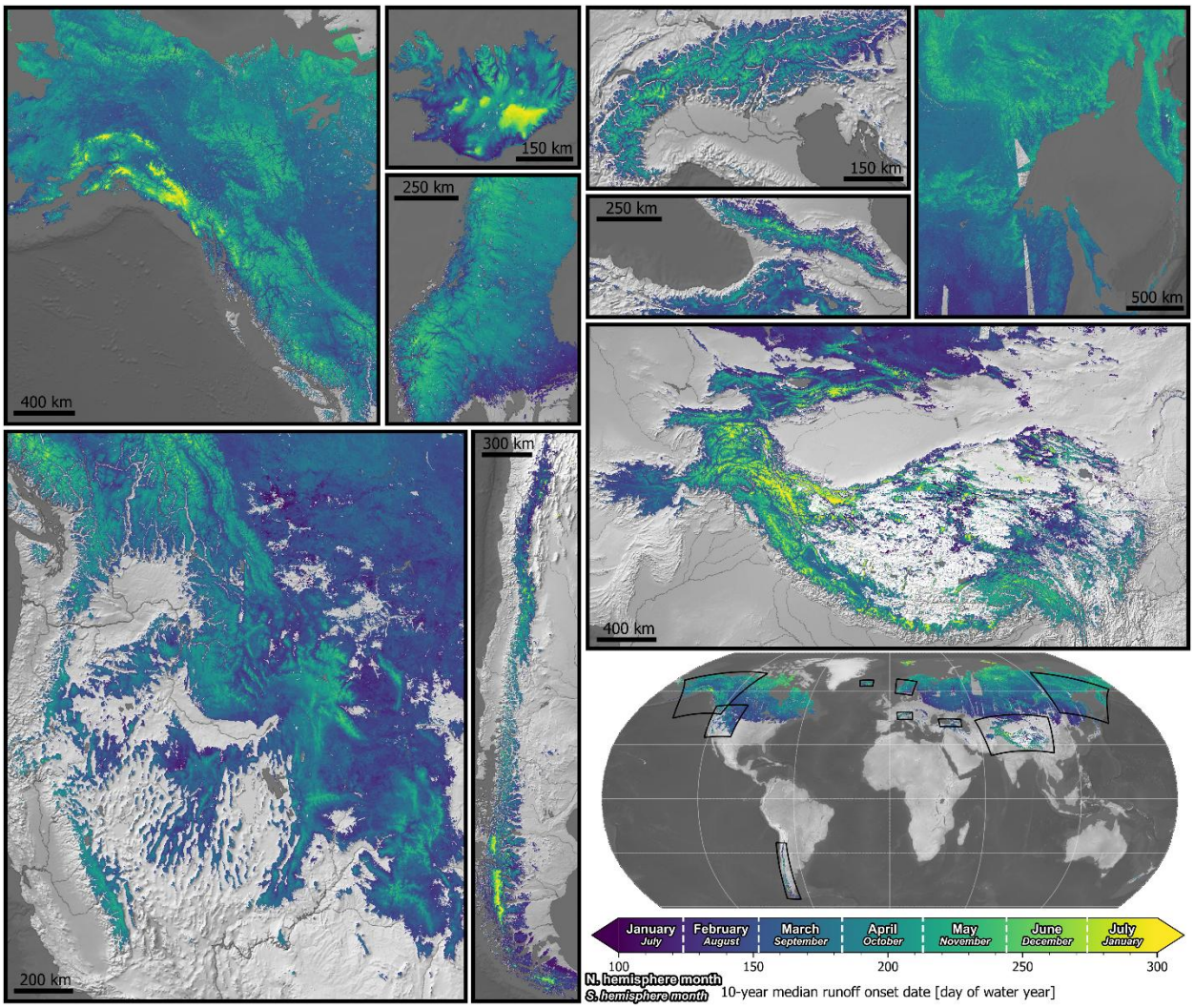
400 km
150 km
250 km
150 km
250 km
500 km
400 km
300 km
200 km
January
July
February
August
March
September
April
October
May
November
June
December
July
January
100
150
200
250
300
N. hemisphere month
S. hemisphere month
10-year median runoff onset date [day of water year]

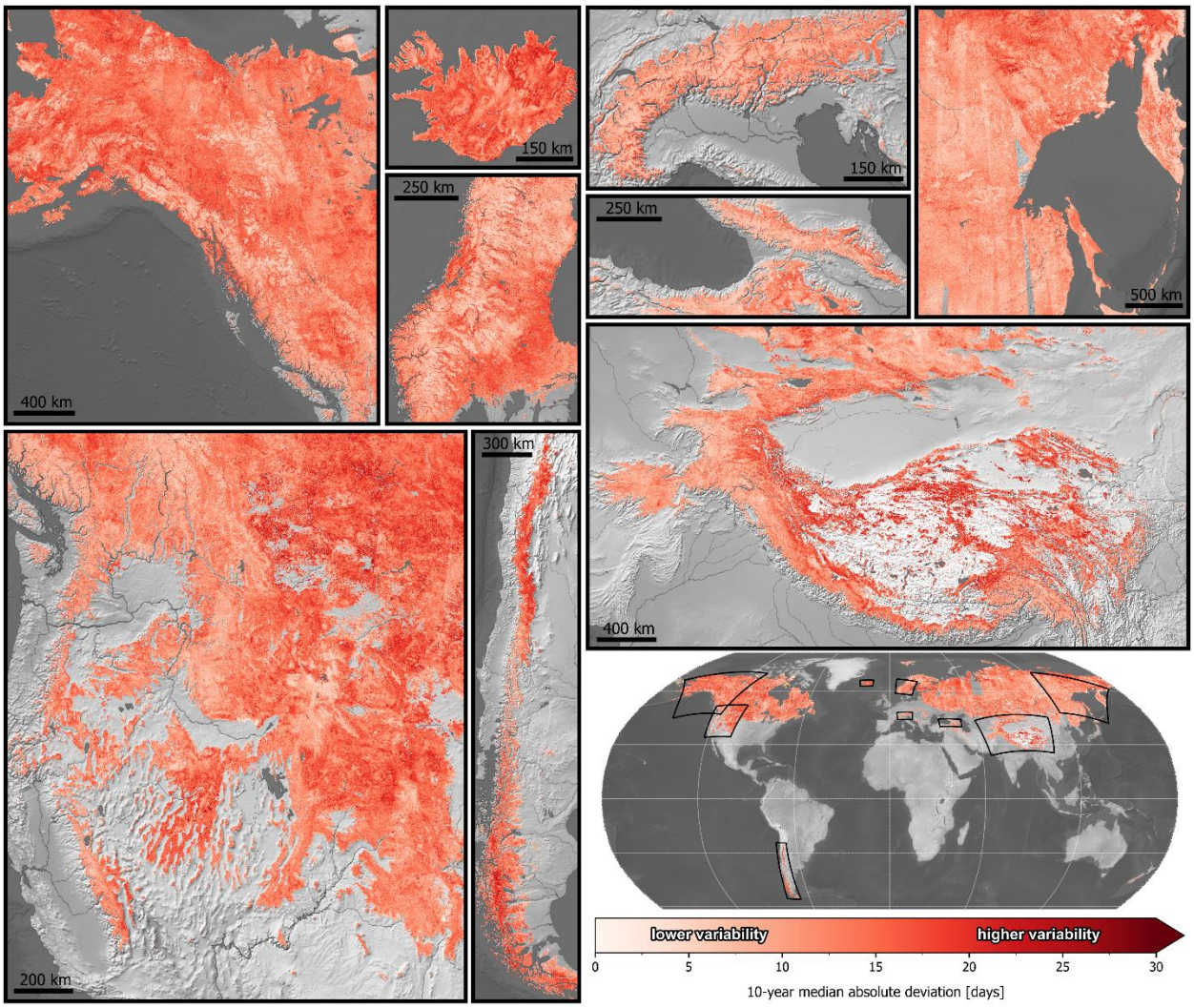

Figure 4.1. Global spatiotemporal variability of snowmelt runoff onset for the 2015 to 2024 period. (Top) 10-year median runoff onset date expressed as day of water year (DOWY), beginning October 1st of the previous calendar year in the Northern Hemisphere, and April 1st in the Southern Hemisphere. Earlier melt is shown in dark blue/purple and later timing in green-yellow. (Bottom) 10-year median absolute deviation of annual runoff onset expressed in days, indicating interannual variability, with low variability (consistent year-to-year runoff onset date) in white and high variability in red.

Continental-scale latitude-elevation binning reveals systematic patterns in snowmelt timing across global seasonal snow cover, including areas outside of mountain ranges.

We observe runoff onset timing delays with increasing elevation across all continents (Figure 4.2, left columns). The strongest elevation gradients occur in mid-latitude regions between ~30-50°N. Above ~50°N, elevation gradients weaken considerably. Europe in particular shows relatively stable elevation gradients at all latitudes. In the southern hemisphere, the Andes demonstrate moderate to strong elevation gradients below ~20°S, but weak elevation gradients above ~20°S in the tropical Andes.

We observe a relationship between runoff onset and latitude, with later onset at higher latitude within the same elevation bin. Specifically between ~30-60°N, runoff onset timing shows clear latitudinal progression, but this relationship weakens dramatically above ~60°N, becoming nearly negligible above ~70°N. Continental variations are evident, with Asia showing the strongest mid-latitude (~30-50°N) runoff onset relationship with latitude, and Europe showing the weakest relationship with latitude.

The interannual variability of runoff onset also varies as a function of latitude and elevation (Figure 4.2, center columns). At elevations above 4000 m in the mid-latitudes, MAD values are ~25-30 days, especially across the Tibetan Plateau. Lower elevation mid-latitude mountain ranges show moderate interannual variability of ~10-20 days. High latitude mountain ranges below 4000 m consistently show the lowest interannual variability, typically below 15 days. Europe and Oceania show the lowest MAD values.

Timing differences between sunny and shaded areas were quantified as the difference in median runoff onset timing between CHILI warm and CHILI cool pixels (CHILI, Section 4.3.2). The largest differences between sunny and shaded areas (most negative values, ~40-60 day difference) occur in mid-latitude regions (30-50°N) and at mid-to-high elevations (2000-5000 m), especially in Asia. For high latitude and low elevation bins, these sunny-shaded timing differences tend to shrink (<20 days). Europe shows notably weaker sunny-shaded timing differences, especially

below 50°N, similar to Oceania. Both North and South America show moderate sunny-shaded timing differences (<30 days), and Asia shows the greatest differences (<40-60 days).

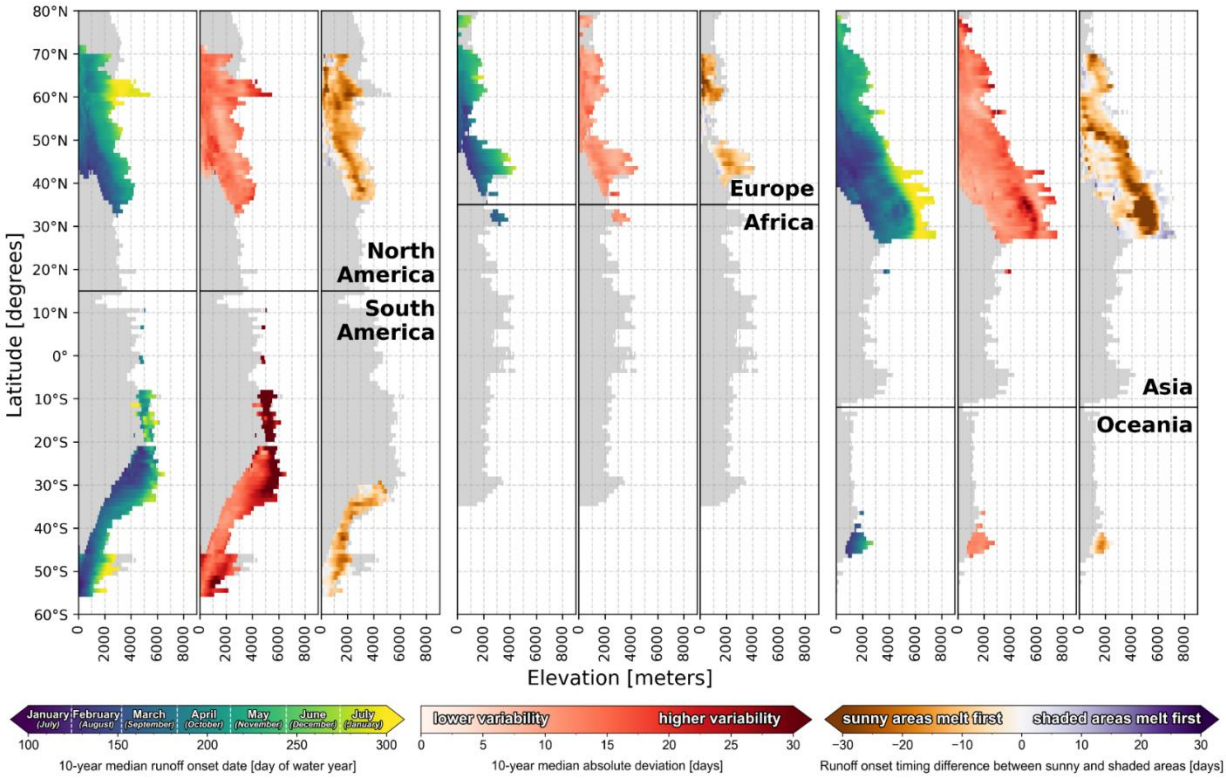

Figure 4.2. Key snowmelt runoff onset metrics for each continent, aggregated over 1° latitude bins and 100-m elevation bins. For each continent, the left column shows 10-year median snowmelt runoff onset date [DOWY] and the center column shows median absolute deviation of snowmelt runoff date [days], as in Figure 4.1. The right column shows the difference in median runoff onset timing [days] between sunny pixels and shaded pixels (See Section 4.3.2), with more negative values indicating earlier melt in areas that receive more solar radiation.

Further examination of sunny-shaded timing differences reveals seasonal modulation across all continents (Figure 4.3). We observe clear temporal evolution of sunny-shaded timing differences vs the 10-year median runoff onset timing. Before the start of spring, runoff onset timing differences between sunny and shaded areas are minimal. Throughout early- to mid-spring, the sunny-shaded timing differences increase to their maximum, and progressively diminishing through late-spring to minimal differences by the end of summer. The specific seasonal timing of

maximum sunny-shaded timing difference depends on latitude. While the vast majority of latitude-elevation bins show sunny areas melting before shaded areas, during the earliest and latest times of the melt season, particularly in Asia, we sometimes observe melt occurring earlier in the shaded areas.

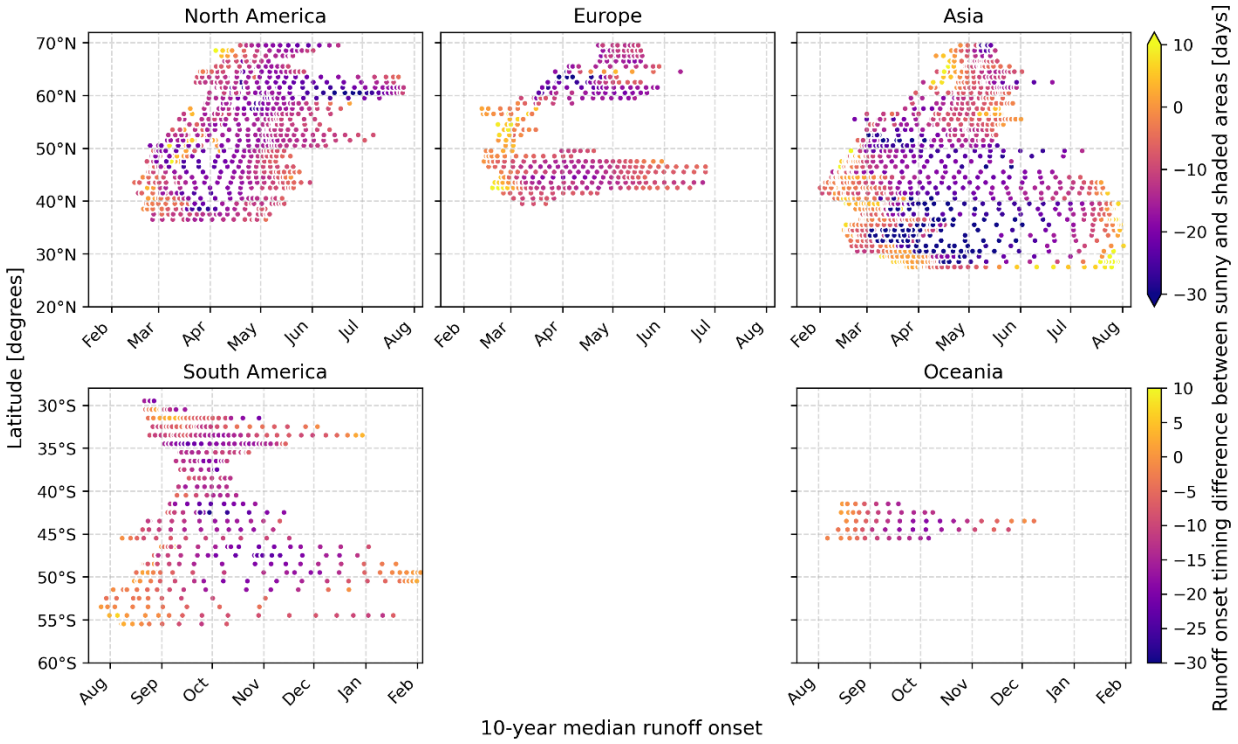

Figure 4.3. Seasonal modulation of sunny-shaded timing difference across continents. Each panel shows the relationship between the observed 10-year median runoff onset timing (x-axis), latitude bin (y-axis), and the difference in median runoff onset timing between sunny and shaded areas (color) for each of the elevation-latitude bins for the continent. Negative values runoff onset timing differences indicate earlier melt in sunny areas. The consistent pattern observed across all continents shows limited sunny-shaded timing differences before spring, increasing to maximum sunny-shaded timing differences during spring depending on latitude, with diminishing sunny-shaded timing differences thereafter.

4.4.2 *Mountain range runoff onset*

Analysis of runoff onset for individual mountain ranges reveals substantial variability in snowmelt timing controls (Figure 4.4). Across all mountain ranges with >1000 m relief, we observe a median runoff onset lapse rate of 3.5 day delay in runoff onset per 100 m increase of elevation, with an interquartile range of 1.9 days/100 m. Five mountain ranges have runoff onset lapse rates above 7.0 days/100 m, including the Tanggula Mountains (9.0 days/100 m, r=0.951), Qiangtang (8.4 days/100 m, r=0.902), Iceland (8.0 days/100 m, r=0.996), New Zealand's Southern Alps (7.4 days/100 m, r=0.992), and the Central Andes Cordillera Oriental (7.3 days/100 m, r=0.828). 12.5% of mountain ranges have strong runoff onset lapse rates between 5 and 7 days/100 m, including Patagonian Andes (5.3 days/100 m, r=0.985), Pyrenees (5.2 days/100 m, r=0.997), and Canadian Rockies (5.0 days/100 m, r=0.989). 45.3% of mountain ranges have moderate runoff onset lapse rates between 3 and 5 days/100 m, including the European Alps (4.8 days/100 m, r=0.997), r=0.888), the Cascade Range (4.1 days/100 m, r=0.996), and Tian Shan (3.5 days/100 m, r=0.954). 32.8% have weaker runoff onset lapse rates between 1 and 3 days/100 m, including Sierra Nevada (2.7 days/100 m, r=0.993) and the Saint Elias Mountains (2.3 days/100 m, r=0.902). Finally, just 7 mountain ranges show the weakest runoff onset lapse rates of less than 1 day / 100 m, including the Shanxi Mountains (0.8 days/100 m, r=0.945), and Kazakh Uplands (0.2 days/100 m, r=0.140).

We created "triplet plots" (Figure 4.4) for selected mountain ranges to document the elevation and aspect dependence of 10-year runoff onset timing,10-year median absolute deviation, and runoff onset timing difference by aspect. The left panel shows combined elevation and aspect controls on runoff onset timing. Most mountain ranges exhibit clear progression from early runoff onset at the lower elevations (outer edges of the plots) towards later runoff onset at higher elevations (center of the plots). Mountain ranges with strong elevation dependence have larger radial color gradients (e.g., Tian Shan), whereas mountain ranges with weak elevation control show more subdued color gradients (e.g., Central Siberian Plateau).

The center panel of the triplet plot shows 10-year interannual variability vs. elevation and aspect. For most mountain ranges, interannual variability is fairly stable across elevations and aspects. Interannual variability increases with elevation for some mountain ranges, including the Sierra Nevada, Tian Shan, and the Verkhoyansk Range. Some mountain ranges have particularly high

interannual variability, often over 20 days, concentrated in the Andes such as the Patagonian Andes, Dry Andes, and Cordillera Occidental, as well as concentrated in Eastern High Mountain Asia: Qiangtang, Qilian Mountains, Bayan Har, Kunlun, Altyn-Tagh, and Min Mountains. The lowest interannual variability, below 10 days, is observed in mid-latitude mountain ranges, especially in Europe and continental Canada. Some mountain ranges show aspect differences (>5 days differences) in interannual variability, such as South-Central Alaska, Pyrenees, and the Kamchatka Peninsula.

The right panel of the triplet plot isolates aspect effects by normalizing runoff onset by elevation bin, showing how median timing across different aspects varies across specific elevations. Northern Hemisphere mid-latitude mountain ranges consistently show the expected pattern of negative values (earlier melt, red) concentrated on southern aspects and positive values (later melt, blue) on northern aspects. The magnitude of aspect differences varies substantially between mountain ranges. Mountain ranges in the western portion of High Mountain Asia, including Tian Shan and Hindu Kush, show particularly strong aspect differences, with maximum median differences exceeding 40 days (south aspects -20 days, north aspects +20 days). To the east, the Himalaya and Transhimalaya show weaker maximum median aspect differences of ~10 days. North American mountain ranges including the Sierra Nevada, Great Basin Range, and Southern Rocky Mountains show moderate maximum aspect differences of less than 20 days. To the north, mountain ranges in Canada and Alaska show larger maximum median aspect differences of up to ~30 days. Similarly, European mountain ranges including the European Alps and the Pyrenees also show strong maximum aspect differences of ~30 days. Northern European mountain ranges including Iceland, and the Scandes, as well as going east up to Central Asia the Ural Mountains and Central Siberian Plateau show some of the weakest aspect differences largely below 10 days. Other polar mountain ranges, such as the Verkhoyansk Range, Brooks Range, and Mackenzie Mountains show much higher maximum aspect differences of at least 20 days.

Southern Hemisphere mountain ranges largely show the opposite (but expected) aspect dependence, with northern aspects melting before southern aspects. The Patagonian Andes, Dry Andes, Meseta Patagonica, and the Southern Alps in Oceania show maximum aspect timing differences of ~25 days.

While most mountain ranges show radially symmetric aspect difference patterns with north-south orientation, some ranges exhibit notable deviations. Some mountain ranges show aspect dependence offset up to 45° from north-south orientation, including the Great Basin Range, Appalachian Mountains, Meseta Patagonica, Dry Andes, and the Scandes. Some mountain ranges display aspect patterns that shift orientation with elevation, visible as angular rotation of the red/blue pattern across elevation bands, including Karakoram, Himalaya, Kunlun, Min Mountains, Bayan Har, Qiangtang, and Stanovoy Highlands. Several mountain ranges show unexpected reversal of the north-south orientation, with sun-facing aspects melting later than shaded aspects, including portions of the Min Mountains, Qiangtang, Bayan Har, and, most dramatically, the Cordillera Occidental in South America.

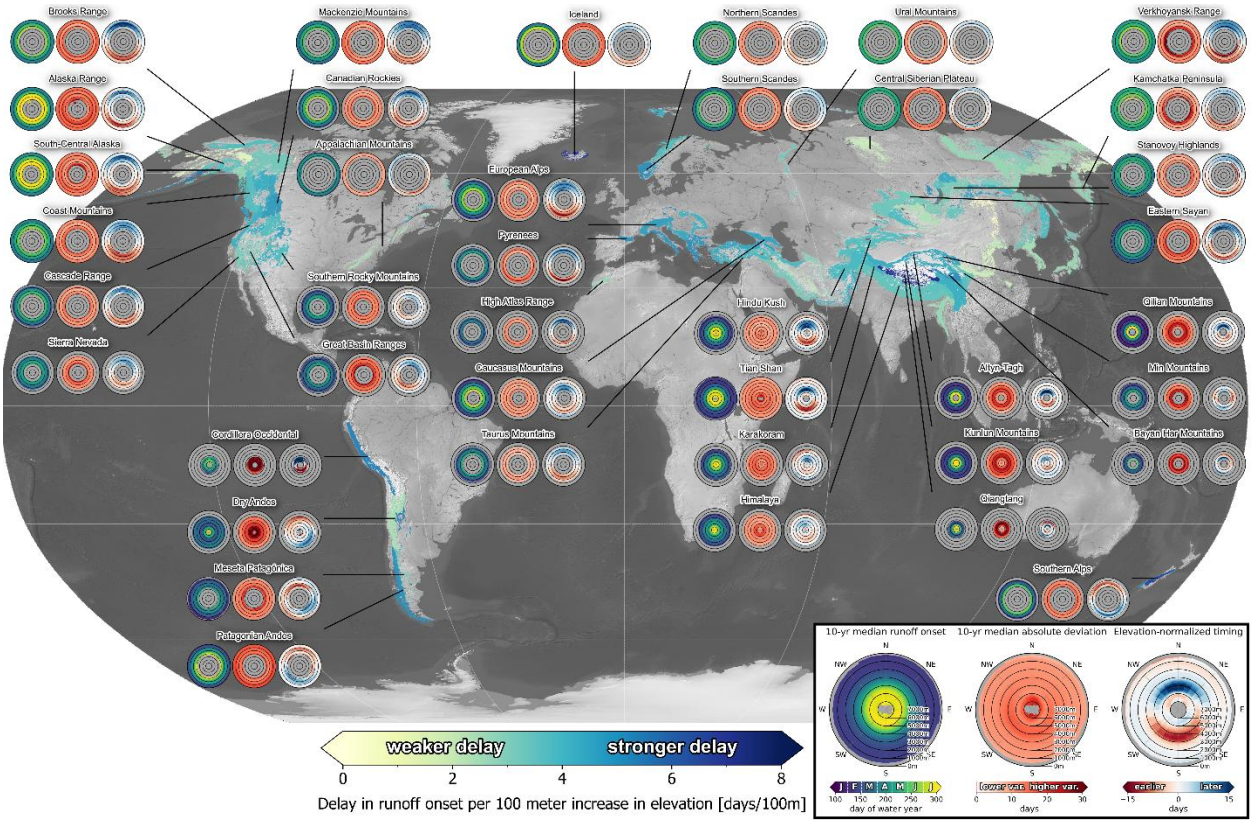

Figure 4.4. Topographic patterns of snowmelt runoff onset by mountain range. Global map shows "runoff onset lapse rate" values for each mountain range, documenting the delay in runoff onset per 100-meter increase in elevation, with higher values (darker blues) indicating steeper gradients and transparency corresponding to correlation strength (more transparent indicates weaker relationships). Triplet plots (see inset key in lower right corner) for selected mountain ranges show metrics binned by elevation (radial position, 0-8000 m ascending inwards) and aspect (angular position, North at the top): (left) 10-year median runoff onset timing [DOWY], revealing typical runoff onset progression across elevation and aspect, (center) 10-year median absolute deviation of runoff onset timing [days], representing interannual variability, and (right) elevation-normalized timing, showing aspect-dependent deviation from the median timing of each elevation bin, to isolate aspect effects independent of elevation gradients. In the elevation-normalized plots, negative values (red) indicate melt earlier than the elevation bin median while positive values (blue) indicate later melt. In the Northern Hemisphere, negative values typically appear on southern aspects and positive values on northern aspects, representing earlier melt on sun-facing aspects. The maximum difference in timing between aspects at a given elevation can be approximated as the sum of the absolute values of the opposing extreme values (e.g., if the

most extreme value from sun-facing aspects is -12 days and the most extreme value from shaded aspects is 10 days, the maximum aspect difference at that elevation is approximately 22 days).

4.4.3 *Interannual variability in runoff onset timing*

The annual runoff onset anomaly maps show coherent spatial patterns of interannual temporal variability at regional scales (Figure 4.5).

Western North America exhibits pronounced interannual variability, with individual years often showing spatially coherent patterns across distinct northern and south subregions. Water year 2015 shows widespread negative runoff onset anomalies for mountain ranges across the region, with all represented mountain ranges experiencing early runoff onset, many 15-40 days earlier than the decade-long median. In contrast, we observed positive anomalies across most mountain ranges during water year 2023 throughout the Western United States, with some mountain ranges showing runoff onset more than 15 days later than their decade-long median.

South America displays both some of the most dramatic annual anomalies as well as large contrasts between sub-regions. Tropical mountain ranges, though they have limited seasonal snow, show consistently large interannual variability beyond 30 days. Further south, the Dry Andes show smaller, but still substantial anomalies, with 4 years in the record exceeding 10 days from the 10-year median values. The Patagonian Andes show the least variability in the Andes.

Europe exhibits moderate annual runoff onset anomalies overall, though the European Alps maintain near-median timing across most years. The Carpathian Mountains, as well as mountain ranges on the Balkan Peninsula and Italian Peninsula have annual anomaly values often exceeding 14 days. In particular, these mountain ranges had runoff onset 20-25 days early in water year 2024.

High Mountain Asia shows dramatic and regionally consistent annual runoff onset anomalies, with many mountain ranges showing runoff onset 20-30 days earlier than the decade-long median in water year 2022, and runoff onset 14 days later than the decade-long median in water year 2017.

Central, Northeast, and East Asia show limited annual anomalies, with mountain ranges rarely exceeding deviations of more than 10-15 days in a given year. Of these mountain ranges, only The Verkhoyansk Range and Kolyma Mountains show the stronger anomaly values.

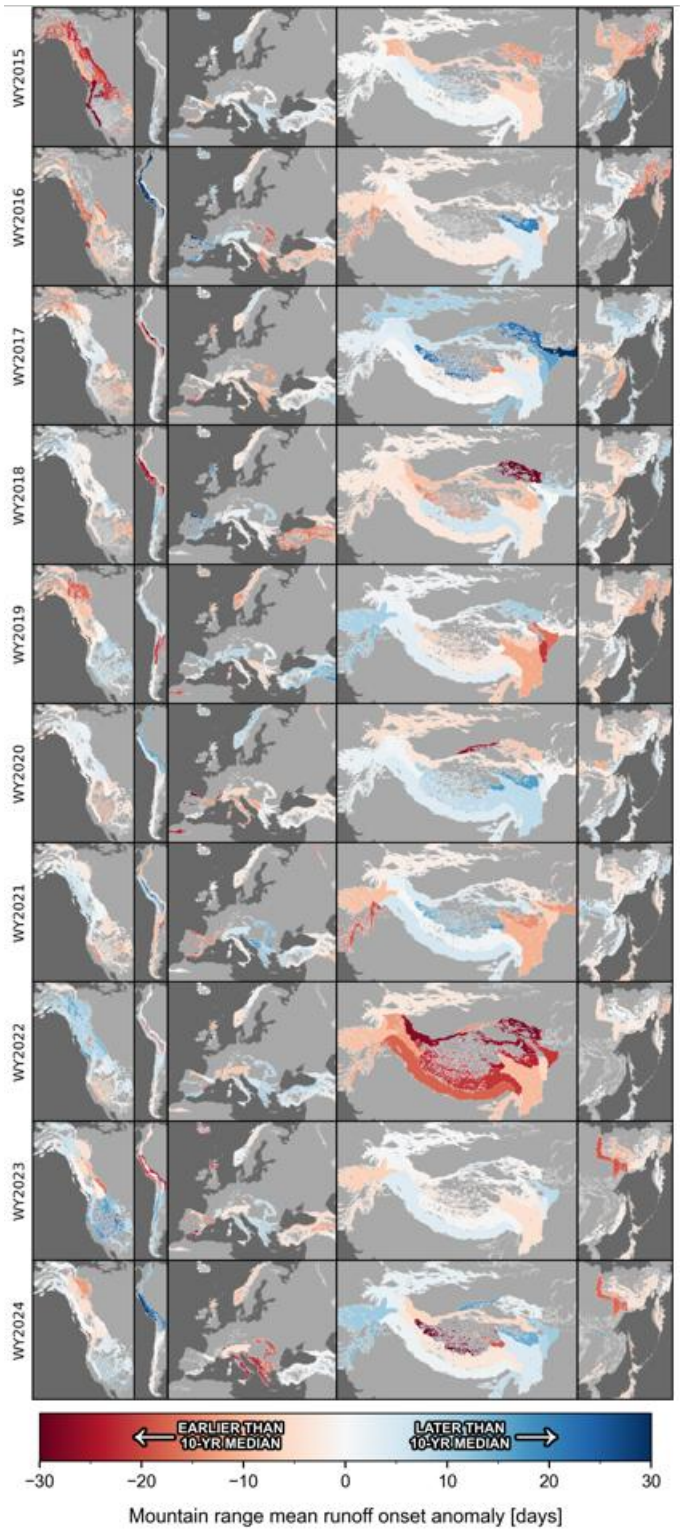

Figure 4.5. Annual snowmelt runoff onset anomaly maps for mountain ranges. Each column represents a geographic region (left to right, Western North America, South America, Europe, High-Mountain Asia, Eastern Asia), and each row shows the mean runoff onset anomaly in days

for that water year, relative to the 10-year median runoff onset values (Figure 4.1). Notable regional events include widespread early melt in Western North America in WY2015, late melt in the Western U.S. in WY2023, and widespread early melt in High-Mountain Asia in WY2022.

4.4.4 *Temperature sensitivity*

Analysis of annual runoff onset anomaly vs. average spring 2-m air temperature anomaly shows clear relationships across mountain ranges during the 10-year study period (Figure 4.6 & 4.7). For the majority of mountain ranges with sufficient data (>5 years), warmer spring conditions correspond to earlier annual runoff onset timing. We quantify this "spring runoff onset temperature sensitivity," as the slope of the linear regression model relating runoff onset timing anomaly to spring temperature anomaly for each mountain range (Figure 4.6).

Spring runoff onset temperature sensitivity values range from -14 days/°C to 14 days/°C, though 90% of mountain ranges have values between -12 days/°C and 4 days/°C. We observe regional coherence, with neighboring mountain ranges typically displaying similar sensitivity values and correlation strengths. Mountain ranges with the highest spring runoff onset temperature sensitivity values tend to have the highest correlation coefficients (Figure 4.7), with correlation coefficients $|r| > 0.4$ for 72% of mountain ranges.

The mountain ranges with the highest and strongest temperature sensitivity were concentrated in the mid-latitudes, such as in the Western United States, where Sierra Nevada exhibits sensitivity of -13.3 days/1°C (r=-0.88), Great Basin Ranges -11.1 days/1°C (r=-0.96), and the Cascade Range of -8.0 days/1°C (r=-0.83). European ranges also have high temperature sensitivity (especially southern Europe and the Iberian Peninsula), including the Cantabrian Mountains (-13.4 days/1°C, r=-0.70) and the Pyrenees (-7.5 days/1°C, r=-0.68), as well as more moderate sensitivity in the European Alps (-4.4 days/1°C, r=-0.77). Most mountain ranges in High Mountain Asia similarly exhibit high temperature sensitivity, such as the Qilian Mountains (-11.3 days/1°C, r=-0.77), Kunlun (-6.9 days/1°C, r=-0.89), and Himalaya (-6.1 days/1°C, r=-0.94), though the mountain ranges on the eastern side of Tibetan Plateau show weak temperature sensitivity relationships, such

as Bayan Har (-1.3 days/1°C, r=-0.14), Min Mountains (-3.5 days/1°C, r=-0.15), Hengduan Shan (-3.6 days/1°C, r=-0.40).

Mountain ranges with the lowest and weakest spring runoff onset temperature sensitivity (and even positive sensitivity, indicating warmer springs corresponding to later snow melt) were concentrated in the polar mountain ranges, in particular those in northeast Asia and Alaskan mountain ranges (Figure 4.7). such as Verkhoyansk Range (0.78 days/1°C, r=0.11), Kamchatka (0.49 days/1°C, r=0.49), and the Brooks Range (-1.4 days/1°C, r=-0.39). Of the 21 mountain ranges that showed positive spring temperature sensitivity, only 6 had r>0.5: Yukaghir Highlands (2.8 days/1°C, r=0.50), Dzhugdzhur Mountains (3.1 days/1°C, r=0.53), Greater Khingan (4.6 days/1°C, r=0.57), Cordillera Oriental (Northern Andes) (30.7 days/1°C, r=0.59), Chersky Range (3.9 days/1°C, r = 0.70), and Shanxi Mountains (7.9 days/1°C, r=0.74).

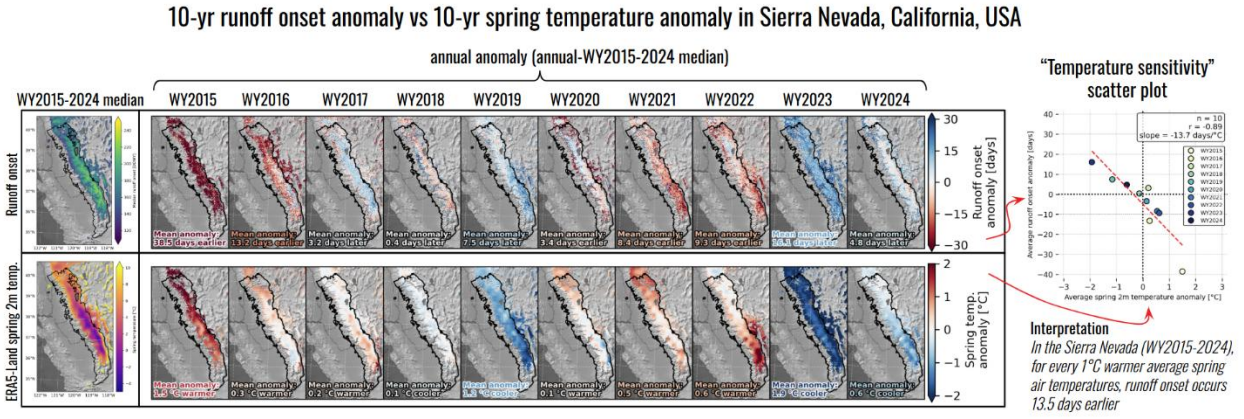

Figure 4.6. Time series of annual snowmelt runoff onset anomaly (top row) and spring 2-m air temperature anomaly (bottom row) for the Sierra Nevada, CA, and calculation of the corresponding spring runoff onset temperature sensitivity value (-13.5 days/°C, r=0.89). The mean annual anomaly for both values is shown in the bottom left corner of each subplot. Temperature sensitivity is calculated as the slope of the regression line between these mean annual anomaly values, expressed as runoff onset anomaly in days per 1°C warmer spring temperature. Negative values correspond to earlier melt onset, with positive values for later onset.

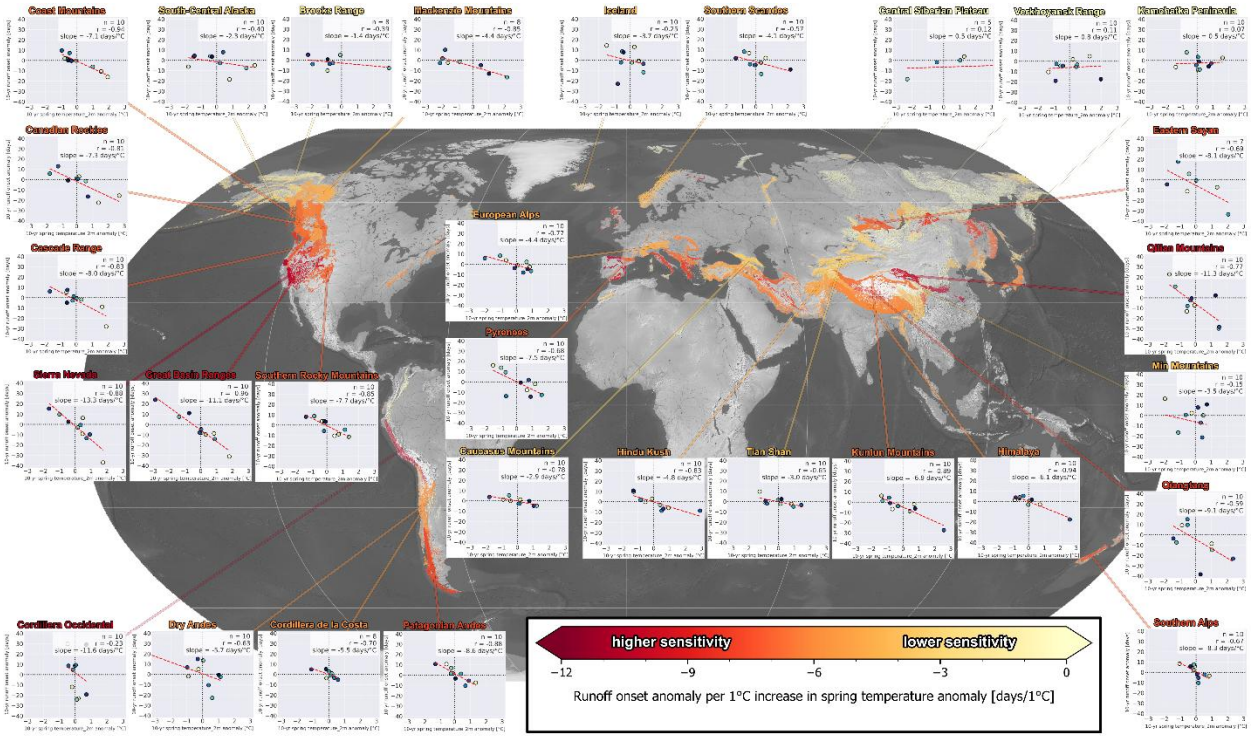

Figure 4.7. Spring runoff onset temperature sensitivity for snowmelt timing across global mountain ranges during the 2015 to 2024 period. The background map shows the relationship between 2-m air temperature and runoff onset timing (expressed as days earlier/later per 1°C) for individual mountain ranges, with dark red colors indicating higher sensitivity, and yellow-white colors indicating lower sensitivity. Inset plots show spring runoff onset temperature sensitivity for select mountain ranges. Each scatter plot includes the linear regression line (red dashed line), number of years (n), correlation coefficient (r), and slope values (days/1°C).

4.5 Discussion

4.5.1 *Global patterns*

Our analysis provides the first comprehensive quantification of snowmelt runoff onset controls across the Earth's mountain regions, revealing systemic patterns that reflect fundamental physical

processes. Runoff onset elevation gradients weaken from mid-latitudes to polar regions, latitudinal effects diminish above 60°N, and sunny-shaded runoff onset timing differences reach their maximum around early- to mid-spring, all demonstrating that typical runoff onset is governed by predictable geographic and topographic controls operating across diverse environments.

The weakening of runoff onset elevation gradients at high latitudes reflects the transition from temperature-dominated to radiation-dominated melt regimes. At high latitudes, late-spring snowmelt occurs when solar radiation is intense (higher sun angles, longer sunlight hours), reducing the importance of temperature gradients with elevation that dominate at lower latitudes (Ohmura, 2001; Zhang et al., 2001). Similarly, the weakening of runoff onset relationship with latitude above 60°N reflects the rapid increase in solar radiation in spring at polar latitudes. By the time snowpacks begin melting at 70°N, solar radiation is already near its annual maximum (Leathers & Robinson, 1997). We observed a delay in runoff onset of 3-6 days/1° latitude which agreed with previous passive microwave observations between 60-70°N (Mioduszewski et al., 2015).

The maximum timing differences between sunny and shaded areas traces a boundary between early-season (DOWY <150) and late-season (DOWY >250) melt regimes. This intermediate timing window (DOWY 150-250) represents conditions where snowpacks are neither energy-starved (early season with low sun angles) nor energy-saturated (late season with abundant radiation across all terrain). In this regime, differential solar radiation between opposing terrain aspects provides sufficient energy to melt sunny areas substantially earlier than shaded areas. The seasonal modulation follows fundamental solar geometry: mid-season sun angles (30-50°) optimize aspect-driven differences in solar radiation, while early season low angles (<30°) and late season high angles (>50°) reduce relative contrasts (Garnier & Ohmura, 1968; Lundquist & Flint, 2006). These patterns persist globally despite vastly different contexts, though local topography and regional climate and weather patterns modulate these controls at the mountain range-scale.

4.5.2 *Mountain range-scale variability and controls*

The variation in runoff onset lapse rates (median runoff onset lapse rate of 3.5 days/100 m with an IQR 1.9 days/100 m) across mountain ranges reveals how geographic context and snowpack characteristics can modulate runoff onset response to climate forcing.

The strongest runoff onset lapse rates (7-9 days/100 m) are located in ranges with deep, persistent snowpacks, especially those with early melt at low elevations and glaciers at high elevations (Tanggula, Qiangtang, Iceland, and New Zealand's Southern Alps). The presence of glaciers creates particularly steep runoff onset lapse rates because they delay melt substantially (Van Tiel et al., 2021).

Moderate runoff onset lapse rates (2-7 days/100 m) characterize the vast majority of mountain ranges globally. The Pyrenees (5.2 days/100 m), Canadian Rockies (5.0 days/100 m), Patagonian Andes (5.3 days/100 m), and European Alps (4.8 days/100 m) show consistent elevation control. Our estimates align well with previous regional studies: the Sierra Nevada's 2.7 days/100 m compares favorably with the ~4 days/100 m documented by Reece & Aguado (1992), while our Cascade Range estimate of 4.1 days/100 m agrees with 4.9 days/100 m found by Gagliano et al. (2023). Maritime ranges show moderate values (Coast Mountains 3.5 days/100 m), as do many High Mountain Asian ranges despite their extreme elevations (Tian Shan 3.8 days/100 m, Hindu Kush 3.5 days/100 m, Karakoram 3.6 days/100 m, Kunlun 3.4 days/100 m).

The weakest runoff onset lapse rates (<2 days/100 m) and accompanying low correlation strengths appear mostly in polar latitudes or high-latitude continental interior low-relief regions (Central Siberian Plateau 1.1 days/100 m, Mongolian Highlands 1.7 days/100 m, Kazakh Uplands 0.2 days/100 m), reflecting limited elevation ranges, shallow snowpacks, and synchronous regional temperature variations. However, some polar mountain ranges maintain moderate runoff onset lapse rates (Brooks Range 3.5 days/100 m, Mackenzie Mountains 3.0 days/100 m).

Aspect effects show systematic geographic patterns reflecting the interplay between solar geometry and regional climate. Western High Mountain Asian ranges (Tian Shan, Hindu Kush, Karakoram) exhibit exceptionally strong aspect effects (>40 days maximum difference), reflecting

continental semi-arid climates with clear skies allowing strong direct solar radiation and steep terrain enhancing geometric effects. In contrast, the Himalaya shows weaker aspect control (~10 days) likely reflecting regional climate differences, antecedent snowpack conditions and preferential deposition, and the influence of the South Asian Monsoon, while interior Tibetan Plateau ranges (Qiangtang, Bayan Har) show surprisingly weak aspect effects despite continental settings, potentially reflecting flat terrain minimizing geometric radiation differences, more frequent cloud cover, or shallow snowpacks melting rapidly once initiated. Mid-latitude ranges show pronounced aspect control (~20-30 days maximum difference) with relatively symmetric patterns where sun-facing and shaded aspects show balanced deviations from elevation medians. Maritime ranges show moderate aspect effects (~15-20 days maximum difference) reflecting frequent cloud cover reducing direct radiation advantages. Polar ranges tend to show weak aspect control, with some exceptions, like the Brooks Range and Mackenzie Mountains which maintain moderate aspect effects (20-25 days).

The unexpected aspect melt patterns observed in several ranges provide insight into the many intersecting controls beyond simple solar geometry. Ranges showing aspect patterns offset from directly north-south (Great Basin Ranges, Scandes, Meseta Patagonica) likely reflect characteristics such as range orientation, dominant weather pattern direction (in both accumulation and melt season), and diurnal anisotropic heating effects. Ranges displaying aspect melt patterns that shift orientation with elevation (Karakoram, Himalaya, Kunlun, Min Mountains, Bayan Har, Qiangtang) present a more complex phenomenon. While changing terrain orientation with elevation may contribute, these rotations likely also reflect elevation-dependent variations in the climate conditions experienced during melt. Different elevations melt at different times of year and therefore under different meteorological regimes–low elevations melting during early spring may experience different patterns of cloud cover, temperature, precipitation, wind and storm directions, than higher elevations melting during late spring or summer. These seasonal shifts in weather patterns could cause aspect melt timing differences to also shift throughout the season, manifesting as aspect patterns that appear to shift with elevation. The unexpected aspect reversals, where sun-facing aspects melt later than shaded aspects, most prominent in the high-elevation tropical Andean Cordillera Occidental though also evident in small portions of Min Mountains, Qiangtang, and Bayan Har, may similarly reflect complex interactions between extreme

elevations, seasonal shifts in synoptic weather patterns, and even the influence of poorly understood sublimation dominance (Gascoin et al., 2013; Réveillet et al., 2020).

4.5.3 *Interannual variability*

Interannual variability in snowmelt runoff onset, quantified through median absolute deviation (MAD), as well as through mountain range anomalies, shows distinct geographic patterns that suggest differences in melt drivers. The lowest interannual variability appears at elevations below 4000 m at latitudes above 50°N in the northern hemisphere, where snowmelt runoff onset shows remarkable consistency. Especially in polar latitudes, MAD <15 days reflects dominance of the annual solar radiation. This stability likely reflects the dominance of energy from consistent seasonal solar radiation cycles over energy from variable synoptic weather patterns during later spring melt periods at these latitudes. When snowmelt occurs during late spring at polar latitudes, solar forcing is intense and consistent year-to-year, while temperature and synoptic variations become secondary (Mioduszewski et al., 2015; Moore & Owens, 1984). Our median absolute deviations align with passive microwave melt onset standard deviations of 3-18 days between 60-80°N, supporting that melt drivers shift from advective toward radiative when melt occurs under strong insolation and weak synoptic influences (Mioduszewski et al., 2015).

Eastern Tibetan Plateau interannual variability (MAD>25 days in Qiangtang, Qilian, Bayan Har, Kunlun, Altyn-Tagh) reflects sensitivity to atmospheric circulation patterns. Short-term oscillations explain approximately 50% of snow cover variability (W. Li et al., 2020), with both Arctic Oscillation and ENSO influencing the subtropical westerly jet and moisture transport (S. Li et al., 2021), creating large swings in winter accumulation and consequently spring melt timing.

The Tropical Andes exhibit extreme interannual variability (MAD>30 days), exceeding all other regions globally. Their position in a transition zone between circulation systems creates intricate interactions between moisture transport mechanisms, which is complicated further by the Andean topography creating a strong east-west divide in temperature and precipitation patterns (Saavedra et al., 2017). Westerly Pacific cold fronts and cut-off low pressure systems vary significantly in frequency and intensity year-to-year (Masiokas et al., 2006; Vuille & Baumgartner, 1998). These

atmospheric patterns drive winter snowfall and vary substantially in relative importance, with ENSO being a dominant driver-El Nino years are generally associated with above average snow accumulation, while La Nina conditions often lead to average or below-average snowfall (Cortés & Margulis, 2017; Masiokas et al., 2006). Snow water equivalent volumes vary from 13 km^3 in extreme dry years to 66 km^3 in wet years (Cortés & Margulis, 2017), with snow course measurements showing fluctuations from 6% to 257% of the 1966-2004 mean (Masiokas et al., 2006). This extreme interannual variability persists even during the extended dry period (the "megadrought") affecting the central Andes since 2010, demonstrating that high interannual variability operates independently of longer-term drought conditions. The decrease in variability from the tropical Andes (>30 days), through the Dry Andes (~15-20 days), to the Patagonian Andes (~10 days) reflects the transition in dominant climate forcing as ENSO influence gives way to Southern Annular Mode control (Saavedra et al., 2018), suggesting a fundamental shift from tropical climate modes to stable mid-latitude westerlies.

The runoff onset anomaly maps demonstrate synoptic forcing can overwhelm typical local geographic controls during extreme years. The early melt across Western North America (15-40 days earlier than the 10-yr median) in WY2015 reflects the "2015 Snow Drought", exceptionally warm spring temperatures and record-low snowpack across the region (Mote et al., 2016). In contrast, the WY2023 late melt in the Western United States (>15 days later than the 10-yr median), especially in the Sierra Nevada, corresponds to the "2023 Snow Deluge", an exceptional snow year, driven by an atmospheric river-dominated winter producing near-record snowpack accumulation across the region (Marshall et al., 2024). The WY2022 widespread early melt across High Mountain Asia (20-30 days earlier than the 10-yr median) similarly reflects anomalously warm spring temperatures ("mega-heatwave", (Hassan et al., 2024)) coinciding with below-average accumulation across the Tibetan Plateau and surrounding mountain ranges (Zhu et al., 2024). These spatially coherent regional-scale events fit with previous findings that synoptic weather patterns can produce elevation and aspect independent timing shifts (Lundquist et al., 2004). In contrast, Europe's relative temporal stability, with the Alps maintaining near-median timing across most years, reflects moderating maritime climate influence and buffering from deep alpine snowpacks.

4.5.4 *Runoff onset spring temperature sensitivity and climate context*

Our observation of systematic temperature sensitivity patterns across mountain ranges, with 90% falling between -12 and +4 days/1°C, provides empirical evidence of the varying importance of spring temperature influence on runoff onset in different geographic and climatic settings. Our mountain range aggregation, while enabling systematic global comparison, obscures substantial intra-mountain-range spatial variability in both temperature and runoff onset anomalies as exemplified by the Sierra Nevada. Though the Sierra Nevada shows a strong spatial correspondence between local temperature and timing anomalies, temperature sensitivity likely varies locally. Aggregation allows us to identify broader sensitivity at mountain ranges but does not capture the local modulation by elevation, aspect, and microclimate that create fine-scale sensitivity gradients.

Geographic patterns align with energy balance expectations. Mid-latitude mountain ranges show the highest sensitivity with strong correlation, indicating robust temperature control. The Western United States exemplifies this pattern: Sierra Nevada (-13.3 days/1°C, r = -0.88), Great Basin Ranges (-11.1 days/1°C, r=-0.96), and the Cascade Range (-8.0 days/1°C, r = -0.83) all show both high sensitivity and strong correlation strength. European mountain ranges, especially those with marginal snowpacks (e.g. Iberian Peninsula) (López-Moreno et al., 2024), exhibit similar high spring temperature sensitivity and strong correlation.

High Mountain Asia shows regionally variable sensitivity. Western and central mountain ranges exhibit moderate to high sensitivity with strong correlations, such as the Kunlun (-6.9 days/1°C, r=-0.89), Hindu Kush (-4.8 days/1°C, r=-0.83), and Himalaya (-6.1 days/1°C, r=-0.94), but mountain ranges on the eastern side of Tibetan Plateau show variable temperature sensitivity relationships with weaker correlations, such as Bayan Har (-1.3 days/1°C, r=-0.14), Min Mountains (-3.5 days/1°C, r=-0.15), Hengduan Shan (-3.6 days/1°C, r=-0.40). Similar to the east-west gradient in aspect patterns, this east-west gradient in spring temperature sensitivity likely reflects different climatological influences, with eastern mountain ranges having higher cloud cover during their respective melt season, potentially decoupling surface temperature from melt energy available through enhanced longwave radiation (and reduced solar).

Polar mountain ranges show low sensitivity with weak correlations, indicating diminished spring temperature influence. Verkhoyansk Range (0.78 days/1°C, r=0.11), Kamchatka (0.49 days/1°C, r=0.49), and the Brooks Range (-1.4 days/1°C, r=-0.39) exemplify polar latitude late-season melt regimes where radiation dominates energy inputs.

Coupling between runoff onset spring temperature sensitivity magnitude and correlation strength suggests that these relationships represent genuine physical controls rather than statistical artifacts. However, we emphasize that these relationships are observational and correlative. spring temperatures covary with many other climate factors (e.g. cloud cover, humidity, precipitation) that each affect snowmelt. The relationships we document integrate these correlated effects but cannot isolate individual mechanisms. The substantial variation in correlation strength underscores this complexity, indicating that spring temperatures alone explains timing variability well in some settings (72% of mountain ranges showing $|r|>0.4$), but poorly in others. The varying strength of spring temperature correlations also reflects temporal mismatch between our fixed spring season window and actual melt timing, as mountain ranges with snow melting in early spring or early summer may show weaker spring temperature correlations because spring conditions are less representative of energy inputs preceding melt. The 21 mountain ranges showing positive spring temperature sensitivity mostly have weak correlations, except for Chersky Range (3.9 days/1°C, r = 0.70) and Shanxi Mountains (7.9 days/1°C, r=0.74). These exceptions, as well as the mountain ranges with particularly weak correlations in eastern High-Mountain Asia and the tropical Andes, suggest unique regional climate dynamics warranting investigation with additional climate variables.

Though we use linear regression to approximate the temperature sensitivity of runoff onset, we know that snow temperature relationships can often be nonlinear in nature. Recent work demonstrates the nonlinearity of snow temperature relationships, with warmer regions showing increasing temperature sensitivity driven by a rapid loss of days below freezing (Blau et al., 2024; Gottlieb & Mankin, 2025). This framework suggests our observed sensitivities may underestimate future responses if warming shifts more regions into highly-sensitive regimes where small temperature changes produce disproportionate effects on runoff onset timing. Temperature sensitivity also varies systematically with elevation within mountain ranges, as demonstrated by

regional studies, with marginal snowpacks at lower elevations typically exhibiting higher sensitivity than deep, persistent snowpacks at high elevations (Hammond et al., 2018; Musselman et al., 2021; Olefs et al., 2020). Moreover, aspect-driven differences in local solar radiation create spatially variable temperature sensitivity regimes, as sun-facing aspects, experiencing warmer baseline conditions than shaded aspects, can exhibit higher temperature sensitivity due to proximity to the nonlinear regime (López-Moreno et al., 2014). Future studies quantifying runoff onset temperature sensitivity more locally, especially separated by elevation and aspect, could reveal these differential responses and improve our understanding of heterogeneous warming responses across complex mountain terrain. As warming continues, understanding these heterogeneous melt onset responses will be essential for anticipating where mountain water resources face greatest vulnerability and for developing regionally-tailored adaptation strategies.

4.5.5 *Limitations and future research directions*

Some inherent limitations of our dataset propagate to our analysis. Due to C-band radar not being able to reliably penetrate forest canopies, our analysis focuses on pixels where forest cover fraction is less than 0.5, limiting inference about densely forested environments where forest-snow interactions can substantially modify energy balance and melt dynamics (Lundquist et al., 2013). Future work incorporating L-band SAR data from missions like NISAR may enable analysis beneath denser forest canopies.

In extreme high elevation (>5000 m) environments of the tropical Andes and High Mountain Asia (approximately 5% of our dataset), sublimation can equal or exceed melt as the primary ablation mechanism. Whether the anomalous patterns we observe in these regions reflect genuine physical processes or SAR methodological limitations in sublimation-dominated environments cannot be definitively resolved with our current dataset and represents an important area for future investigation.

Variability in Sentinel-1 orbital coverage introduces artifacts in our interannual variability estimates. The constellation's evolution over our study period means that different locations have different numbers of observations across water years, and that the specific water years contributing

to our median absolute deviation calculations vary spatially. This manifests as discontinuities in MAD values along satellite track boundaries, visible in our global maps, indicating that some apparent spatial variability in interannual variability may reflect sampling artifacts rather than genuine differences in climate forcing stability.

Our range-level aggregation enables systematic global comparison, but smooths intra-mountain-range variability. Future studies could use this dataset to examine sub-range patterns, particularly in large mountain systems, to reveal how local topography, microclimates, and terrain characteristics further modify the mountain range-scale patterns we document. The decade-long record provides unprecedented global coverage but remains limited for robust trend analysis. As Sentinel-1 and successor missions continue, more formal analysis of longer-term trends will become possible.

Our temperature sensitivity analysis (Section 4.5.4) represents one of the first global-scale empirical quantifications of temperature-snowmelt relationships at high-resolution, but its potential remains largely untapped. These sensitivity estimates could improve short- and long-term seasonal snowpack forecasting: combining our range-specific sensitivities with seasonal temperature forecasts could provide operational and probabilistic estimates of snowmelt timing anomalies months in advance, and combining our sensitivities with longer-term climate scenarios could help identify future vulnerability.

Finally, we'd like to emphasize a critical distinction: our analysis characterizes snowmelt runoff onset–when liquid water begins moving across or through the snowpack–rather than streamflow generation. Recent tritium age dating shows streamflow during snowmelt in western US mountains is dominated by groundwater with mean residence times of 5.7+/-4.3 years, with geology strongly mediating storage and release (Brooks et al., 2025). The lag between SAR-detected runoff onset and streamflow generation likely varies with geology, subsurface storage capacity, and catchment size. As downstream water availability is the ultimate quantity of concern for the hundreds of millions depending on mountain water resources, bridging this gap represents a critical research frontier for our community.

4.6 CONCLUSIONS

This study provides the first comprehensive global characterization of snowmelt runoff onset patterns and their controls using a decade of Sentinel-1 SAR observations spanning 2015-2024. By analyzing snowmelt runoff onset at the continent scale and quantifying controls within 150 individual mountain ranges, we reveal that snowmelt timing is governed by predictable geographic and topographic controls operating across Earth's diverse mountain environments, though local topography and regional climate modulates these controls at the mountain range-scale.

We explored the geographic and topographic controls of runoff onset by analyzing continent-scale latitude-elevation patterns and quantifying mountain range-scale elevation and aspect relationships. At the continent-scale, our analysis demonstrates the weakening elevation gradients from mid-latitudes to polar regions, the diminishing of latitudinal timing differences above 60°N, and the distribution and seasonality of sunny-shaded runoff onset timing differences. At the mountain-range scale, runoff onset lapse rates generally sit around 3.5 days /100 m, but vary geographically, with the highest runoff onset lapse rates in mountain ranges with high relief and extensive high elevation glacier area, and the lowest runoff onset lapse rates in mountain ranges at low elevations and lower relief. Aspect effects show dramatic regional variability–western High Mountain Asian mountain ranges exhibit exceptionally strong control (>40 days maximum difference) under relatively clear continental conditions during melt, whereas the Himalaya shows much weaker effects (~10 days) reflecting cloud differences, especially related to the South Asian Monsoon.

We explored the interannual variability of runoff onset by characterizing geographic patterns in timing consistency, documenting regional runoff onset timing anomaly events, and quantifying empirical relationships between spring temperature and runoff onset timing across mountain ranges. We quantified the effect of previously-documented regional scale anomaly events–the 2015 Western North America drought, 2023 Western US deluge, 2022 High Mountain Asia early melt—demonstrating how synoptic forcing can largely dictate interannual variability in runoff onset timing, producing spatially coherent 20-40 day shifts across entire regions. Temperature sensitivity patterns show spring temperature provides moderate-to-strong explanatory power for

timing variability in 72% of mountain ranges, though with dramatic geographic variation. Mid-latitude mountain ranges show highest sensitivities (up to -14 days/°C) with strong correlations, while polar mountain ranges show minimal sensitivity as solar radiation dominates.

Our globally consistent observational approach enables, for the first time, systematic quantification and intercomparison of topographic and climatic controls on runoff onset across Earth's seasonal snow-covered mountains. This represents a fundamental advance over previous research, which has predominantly examined individual mountain ranges using region-specific datasets and methodologies. This work establishes a foundation for understanding differences in how mountain water resources respond to climate forcing and change across Earth's diverse snow-covered regions. As warming progresses and more ranges transition into temperature-sensitive regimes, the patterns and relationships we document become increasingly critical for anticipating impacts on water resources for the over a billion people that rely on mountain snowmelt.

Chapter 5. FROM PEAK TO PLANET: SYNTHESIS, IMPLICATIONS FOR WATER RESOURCES, AND FUTURE DIRECTIONS

This chapter aims to summarize the methodological and scientific advances presented in previous chapters, examine their implications for understanding mountain snow and water resources, and identify priorities for future research.

5.1 INTRODUCTION

Mountain regions function as natural water storage systems that capture, store, and release water to downstream populations. Immerzeel et al. (2020) quantified this dependence through the mountain water tower index, demonstrating that 1.9 billion people rely on mountain water resources. However, the timing of meltwater release–governed by snowmelt runoff onset–exhibits substantial interannual variability. Characterizing this variability is essential for understanding water security, as the timing determines when water becomes available for agriculture, hydropower, municipal supply, and ecosystem functions.

In Chapter 2, we demonstrated how the Sentinel-1 constellation enables systematic observation of runoff onset for a sample of stratovolcanoes in the Cascade Range of North America. In Chapter 3, we scaled this methodology globally, processing ~3.9 million Sentinel-1 scenes to produce a comprehensive dataset spanning water years 2015-2024. In Chapter 4, we systematically analyzed patterns and controls across all major mountain ranges on Earth, quantifying how elevation, aspect, latitude, and spring temperature govern runoff onset and its interannual variability. This chapter

synthesizes these findings and examines their implications for downstream populations dependent on mountain water resources.

5.2 SYNTHESIS OF METHODOLOGICAL AND SCIENTIFIC ADVANCES

5.2.1 *Physical basis and initial validation*

Chapter 2 demonstrated an improved and scalable methodology for mapping runoff onset using Sentinel-1 backscatter time-series analysis. We validated our approach over stratovolcanoes in the Cascade Range of North America against estimated runoff onset from five in-situ snow pillows, finding good agreement between our estimates and the snow pillow estimates (median offset of 1 day, median absolute offset of 10 days). Regional analysis across the stratovolcanoes of the Cascade Range quantified topographic controls on snowmelt timing, finding median delays in snowmelt runoff onset of 4.9 days per 100 m of elevation gain ("runoff onset lapse rates"), and moderate correlation with aspect and slope, though only at mid-high elevations.

5.2.2 *Global scaling*

Chapter 3 improved and extended the methodology from chapter 2 through cloud-based processing workflows and snow presence masking using a custom snow phenology dataset. The resulting dataset for water years 2015-2024 provides an unprecedented combined spatial resolution of 80 m and average temporal resolution of 9.3 days (though this varies spatially, some locations and water years have daily resolution). We performed a systematic analysis of environmental controls, identifying forest cover fraction, SWE accumulation, and temporal resolution as critical factors affecting dataset performance. We validated our dataset against estimates from over 900 automated

weather stations in the Western U.S., finding a median difference of 1 day and a median absolute deviation of 9.0 days.

5.2.3 *Runoff onset patterns and controls across mountain ranges*

Chapter 4 provided the first high-resolution systematic quantification of topographic and climactic controls on snowmelt timing across 150 mountain ranges. Analysis of runoff onset lapse rates revealed a median runoff onset lapse rate of 3.5 days per 100 m of elevation gain, but with substantial variability (-0.5 to 9.0 days/100 m). Mountain ranges with high relief and extensive glacier coverage exhibited the steepest runoff onset lapse rates.

Aspect control on snowmelt timing demonstrates predictable yet regionally variable patterns. Maximum differences between sun-facing and shaded aspects reach 30-60 days during early- to mid-spring, following seasonal modulation that diminishes in intensity earlier and later in the season. However, local climate and topographic characteristics can lead to large differences in aspect control. Western High Mountain Asia under clear-sky continental conditions show aspect differences exceeding 40 days, whereas the cloudier Himalayan ranges show much weaker aspect differences of 10 days or less.

Broadly, high-latitude ranges displayed lower interannual variability (<15 days MAD), while mountain ranges in the tropical Andes and eastern Tibetan Plateau show higher interannual variability of 30 days or more.

Temperature sensitivity analysis demonstrated 72% of ranges show correlations |r|>0.4 between spring 2-m air temperature and annual runoff onset timing for the 2015 to 2024 period. Mid-latitude ranges exhibit sensitivities of -8 to -13 days/°C, while polar ranges show minimal air temperature influence.

These systematic analyses demonstrate that while runoff onset can be broadly understood to vary coherently over geographic and climatic gradients, runoff onset is heavily influenced by regional and local complexities. Given this nuance, in the following sections, we aggregate our runoff onset dataset by river basin (HydroBASINS level 5, (Lehner & Grill, 2013)) to explore more hydrological impacts. We considered several different basin definition options, but ultimately chose level 5 to balance sufficient spatial detail with hydrologically meaningful catchment boundaries.

5.3 FROM PLANET…

Our basin aggregation of 10-year median runoff onset (Figure 5.1) reveals fundamental patterns similar to those observed in earlier chapters: later melt at higher latitudes and higher elevations. The global distribution shows basins with median runoff onset ranging from January in low-elevation and low-latitude regions, to late June in high-latitude and high-elevation regions. Interannual variability, expressed as mediate absolute deviation (MAD), displays stark regional contrasts. Basins in Europe and North Asia show relatively low interannual variability (<15 days MAD), while basins in the subtropical Andes and basins in and around the Tibetan Plateau demonstrate high interannual variability (>30 days MAD).

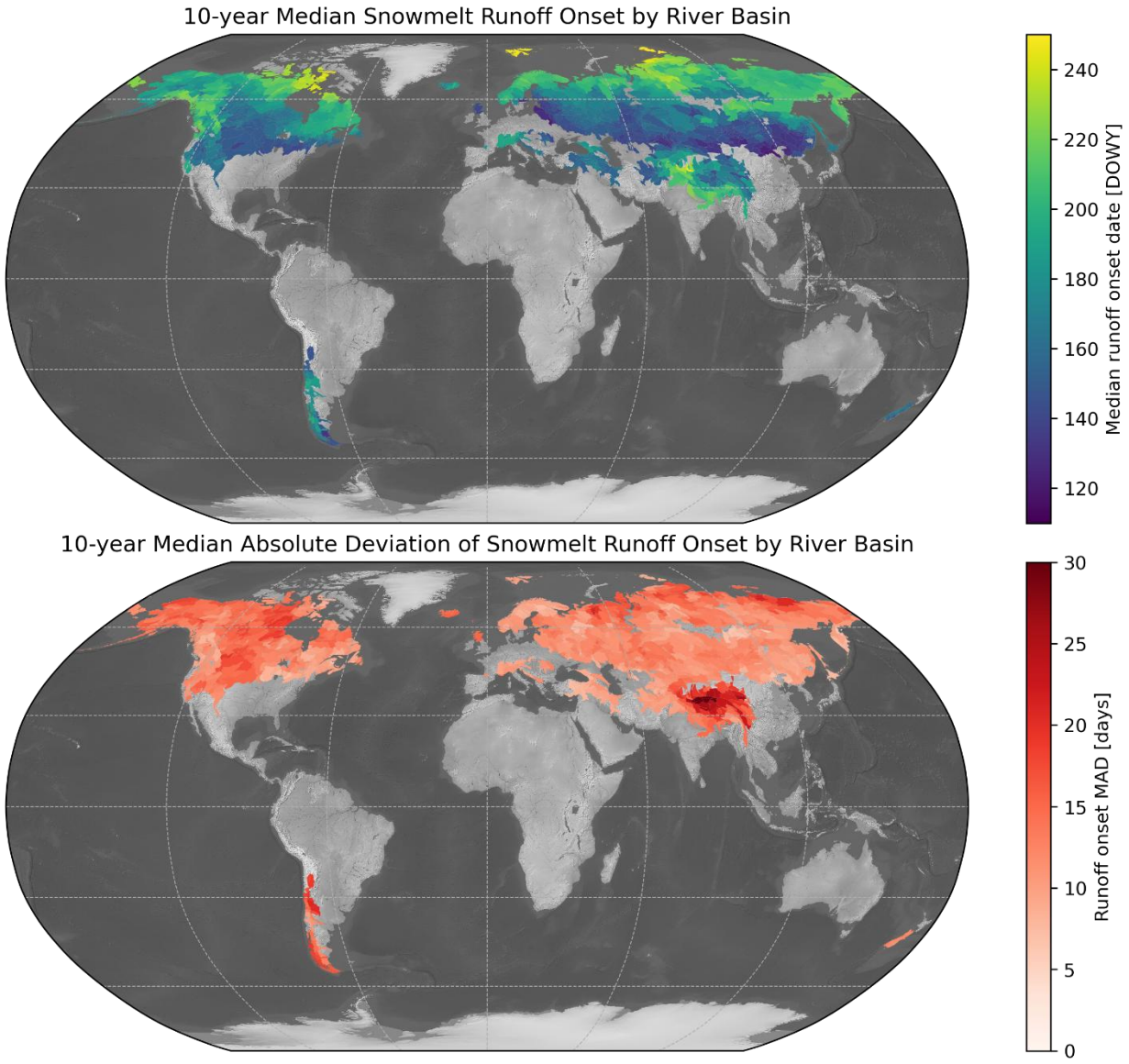

Figure 5.1. Global spatiotemporal variability of snowmelt runoff onset for WY2015-2024 by basin. (Top) Basin mean of per-pixel 10-year median runoff onset date expressed as day of water year (DOWY), beginning October 1st of the previous calendar year in the Northern Hemisphere, and April 1st in the Southern Hemisphere. (Bottom) Basin mean of per-pixel 10-year median absolute deviation of annual runoff onset expressed in days. These basin aggregations, by nature of the basins not having uniform hypsometry, will have values weighted by the elevation distribution of each basin.

The river basin annual runoff onset anomaly maps (Figure 5.2) exhibit coherent regional patterns that reflect documented synoptic-scale weather events. With these events, we observe runoff onset timing anomalies exceeding 30 days, explored further in 5.4.1 and 5.4.2.

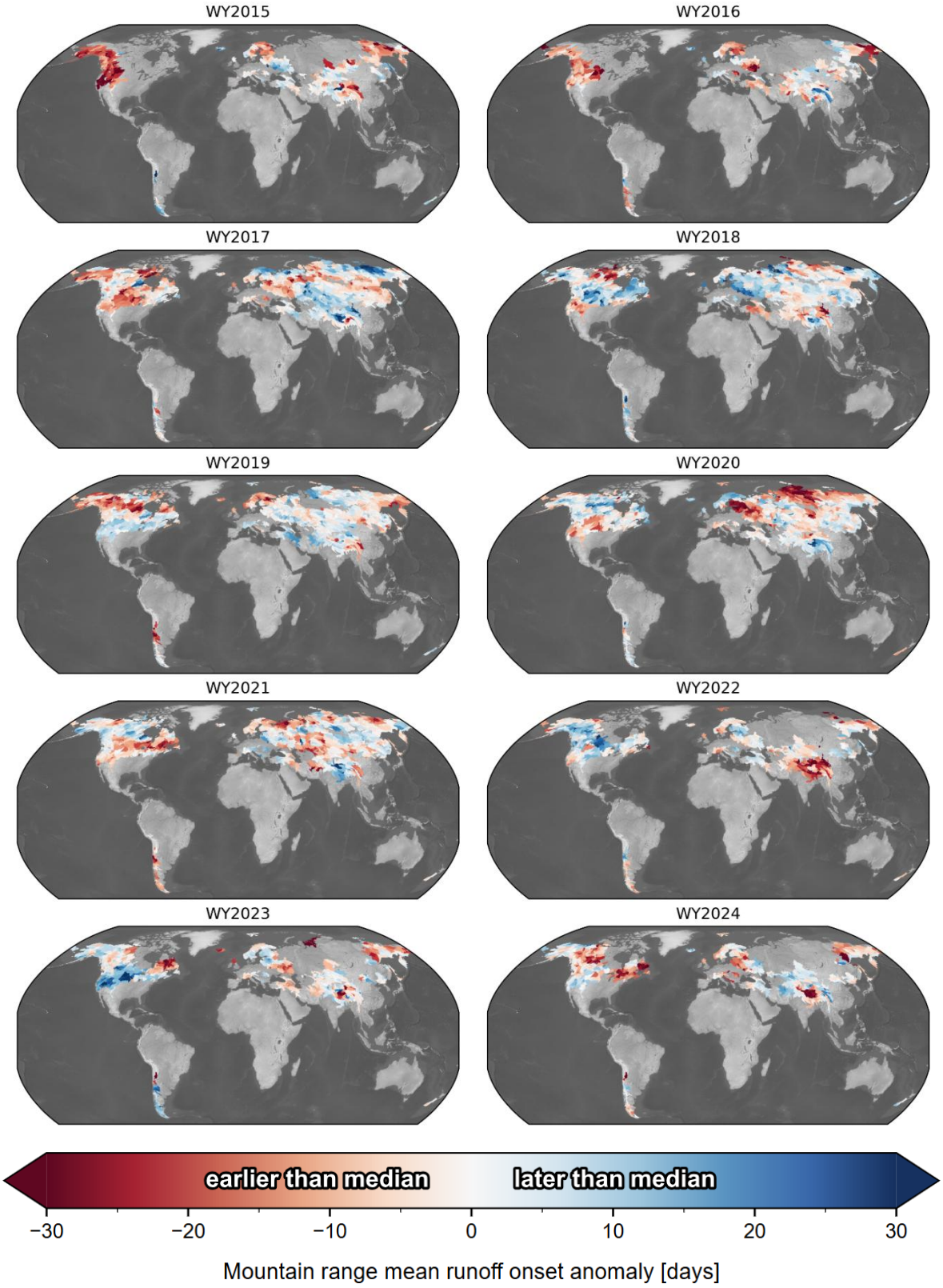

Figure 5.2. Basin mean of per-pixel annual snowmelt runoff onset anomaly (annual minus 10-year median).

5.4 …To peak (Regional implications)

5.4.1 *High-Mountain Asia*

High-Mountain Asia provides a critical case study given its role as a water resource for major river systems that support over a billion people (Immerzeel et al., 2020). Basin-scale patterns (Figure 5.3) reveal substantial heterogeneity in both median runoff onset and interannual variability. The Indus headwaters show median runoff onset in May, with low interannual variability (MAD<15 days). The Ganges and Brahmaputra headwaters have similar median runoff onset in May, with slightly higher interannual variability (~15 days MAD). Contrastingly, the headwaters of the Mekong, Yangtze, and Yellow have early median runoff onset in April, with moderate interannual variability (15-30 days MAD). In this way, basins draining the eastern portions of the Tibetan Plateau have earlier but more erratic runoff onset.

Basin population distribution shows the highest concentrations in the Indus, Brahmaptura, and Ganges headwaters, (10-100M people), though it's important to note that these values represent population within the headwater basin boundaries, substantially underestimating total dependence by not accounting for downstream use. We also show the basin mean percentage of precipitation falling as snow calculated using 1950-2024 precipitation data from monthly aggregated ERA5-Land (Muñoz, 2019). This metric represents a rough proxy for the relative importance of snow compared to all precipitation in a basin. The percentage of precipitation falling as snow displays a gradient increasing from east to west across the Tibetan Plateau.

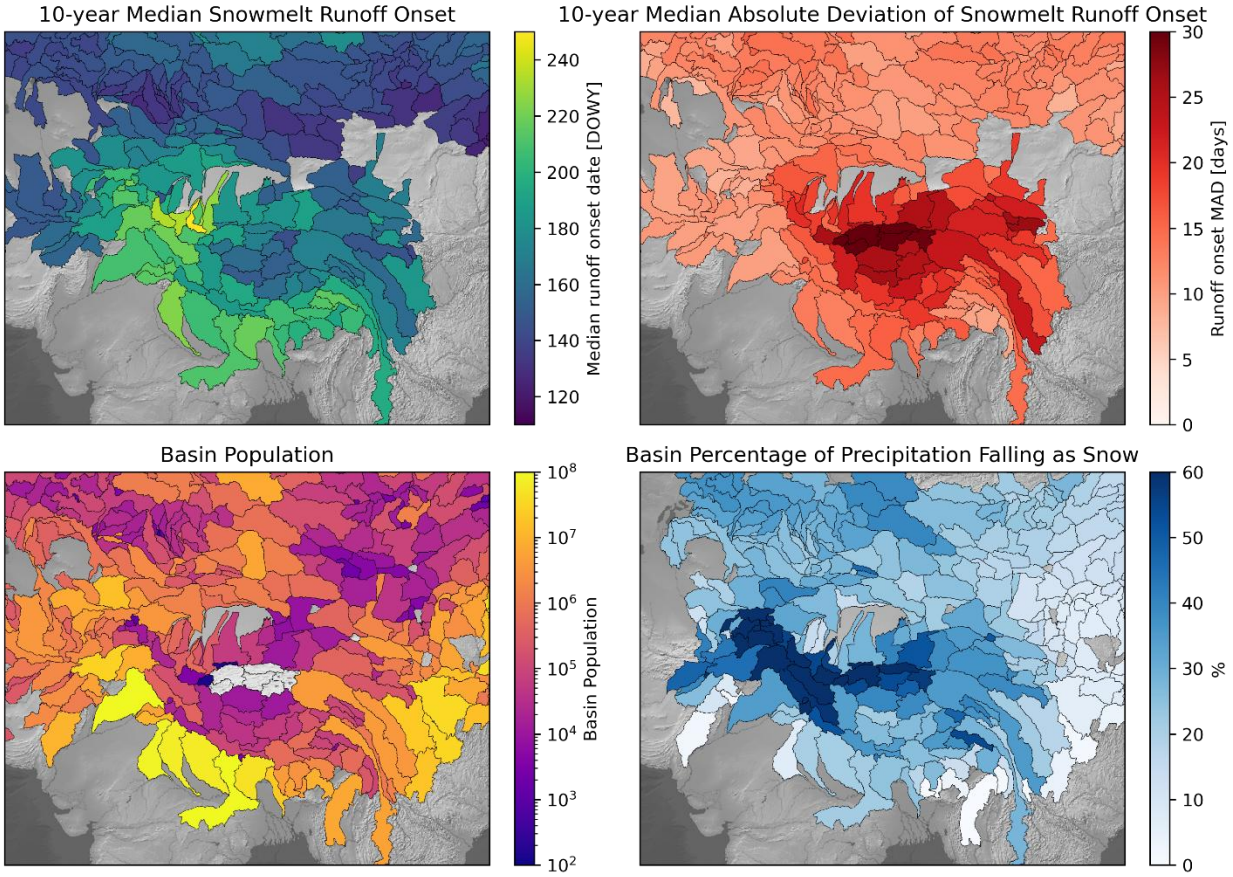

Figure 5.3. High-Mountain Asia river basin metrics. (Top left) Basin mean of per-pixel 10-year median snowmelt runoff onset. (Top right) Basin mean of per-pixel 10-year median absolute deviation of runoff onset timing. (Bottom left) Population within basin (Earth Science Data Systems, 2025). (Bottom right) Basin percent precipitation falling as snow.

The annual runoff onset anomaly maps (Figure 5.4) demonstrate susceptibility to synoptic-scale weather patterns. For example, the widespread early runoff onset in water year 2022, exceeding 30 days early for many basins surrounding the Tibetan Plateau, likely reflect the combined effects of below-average seasonal snow accumulation across the plateau, as well as the spring 2022 mega-heatwave (Hassan et al., 2024; Zhu et al., 2024). Conversely, water year 2017 shows coherent patterns of delayed snowmelt runoff onset. In other water years, the annual runoff onset anomaly

is less regionally homogeneous, potentially indicating differential weather across the region. This quantification of interannual variability has direct implications for downstream water security, as these weather patterns largely dictate the modulation of runoff onset from year to year.

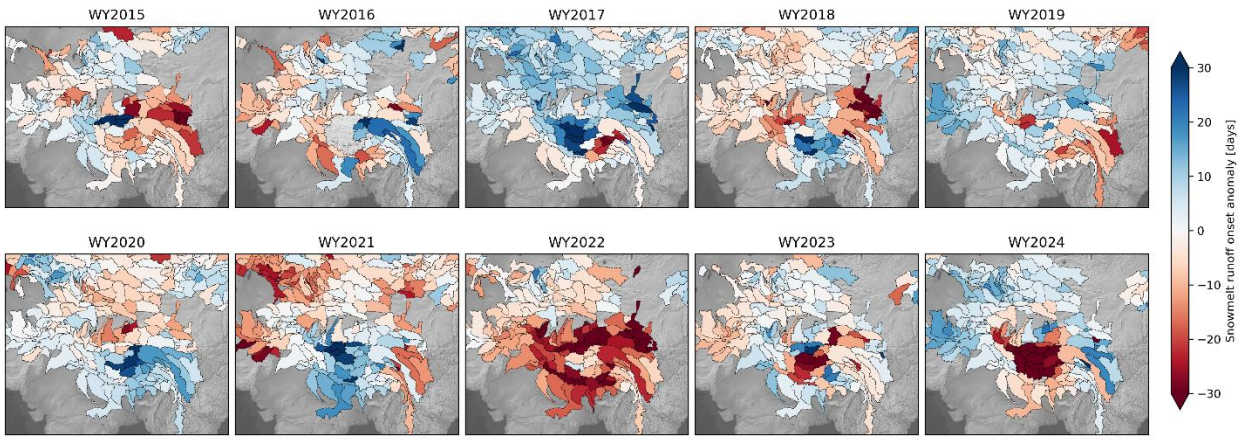

Figure 5.4. Basin mean of per-pixel annual snowmelt runoff onset anomaly (annual minus 10-year median).

To provide a high-level preliminary assessment of basin vulnerability to runoff onset timing interannual variability, we examine the relationships between the fraction of precipitation falling as snow, median runoff onset, interannual variability (MAD and largest WY2015-2024 runoff onset anomaly), and basin population (Figure 5.5). These analyses serve primarily to explore potential relationships, rather than comprehensive vulnerability assessment. Factors such as downstream population dependence and demand, water usage, water storage infrastructure, etc., are not currently considered.

High-mountain Asia basins with 15-40% precipitation falling as snow and median runoff onset dates in late February to mid-April tend to show the highest interannual variability, suggesting small perturbations in temperature and precipitation can substantially affect snow accumulation

and melt. The basins with the largest observed anomalies exceeded 30 days, and tended to have <50% precipitation falling as snow. Many basins with populations of at least 10 million show high runoff onset interannual variability. Interestingly, basins with higher percentage of precipitation falling as snow and later median runoff onset dates often showed a smaller maximum runoff onset anomaly, potentially reflecting the buffering effect of high-elevation snowpack and glacier ice.

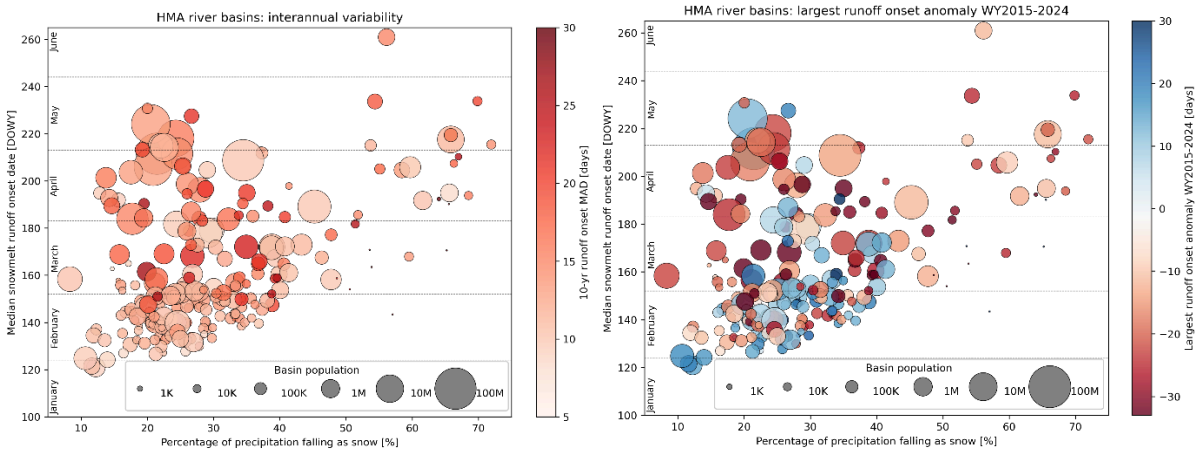

Figure 5.5. Basin-wide runoff onset vulnerability assessment. (Left) Basin 10-year median absolute deviation vs. percentage of precipitation falling as snow and 10-year median runoff onset. (Right) Basin largest runoff onset anomaly in the 10-year record vs. percentage of precipitation falling as snow and 10-year median runoff onset.

5.4.2 *Western North America*

Western North America presents a complementary case study, with extensive observational infrastructure and well-documented climate-hydrology relationships (M. Dettinger, 2005; M. D. Dettinger et al., 1998). Basin-scale patterns show median runoff onset ranging from early February

in the continental interior, to late May in northern Canada and along the Coast Range Arc. Also along the Coast Range Arc is lower interannual variability (<15 days MAD) and >50% of precipitation falling as snow. Population distribution in basins tends to vary from the hundreds to around 10 million, mostly decreasing from the south to the north.

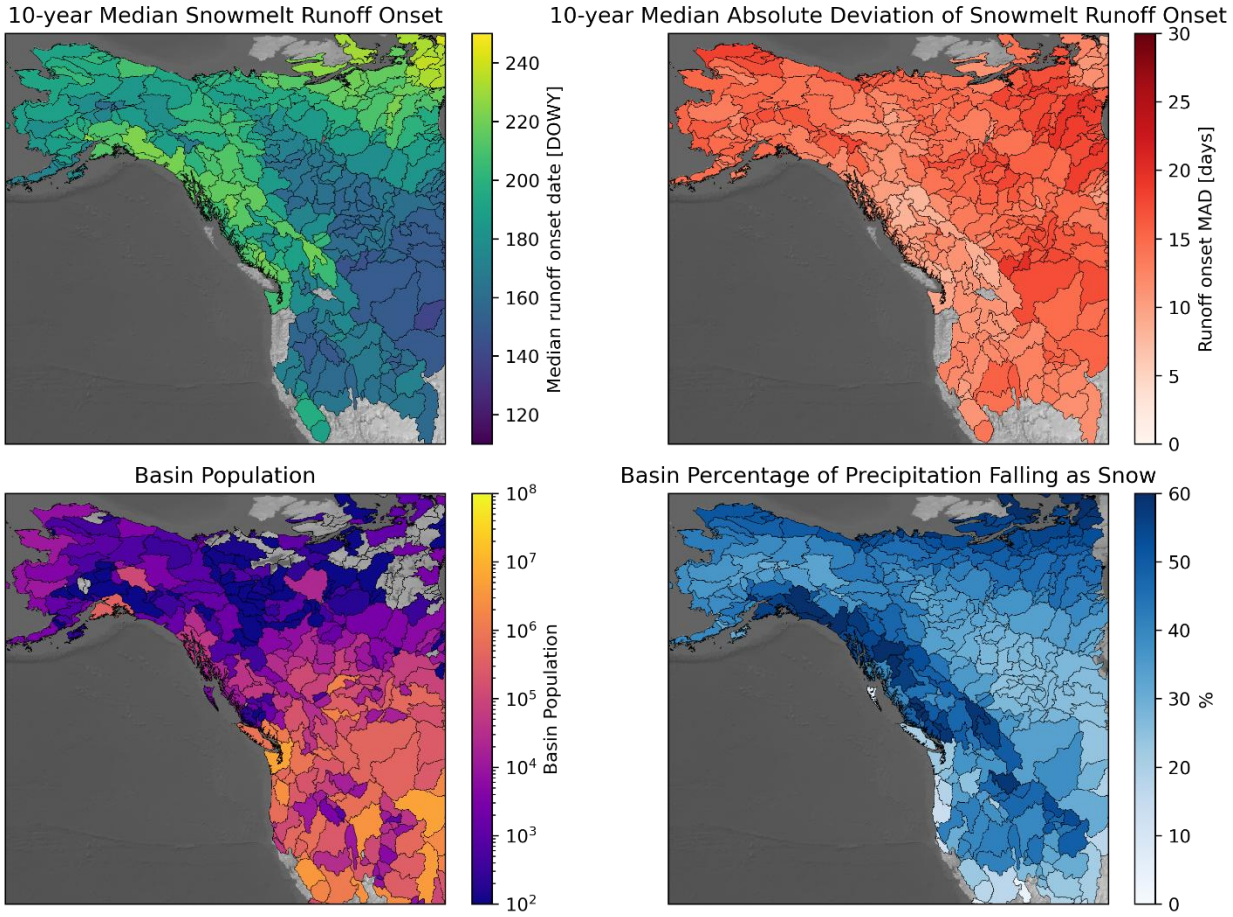

Figure 5.6. Western North America river basin metrics. See Figure 5.3 caption for details.

Similar to High-Mountain Asia, the annual runoff onset anomaly maps (Figure 5.7) capture well-documented synoptic-scale weather events affecting western North America. Water year 2015 has widespread early anomaly values, with most basins showing runoff onset 20 days early relative to the 10-year median, and many basins exceeding 30 days early. This coincides with record low

April 1 SWE and exceptionally warm winter temperatures of the infamous “2015 snow drought” (Mote et al., 2016). In contrast, water year 2023 shows widespread late snowmelt anomaly in the western U.S., particularly in the basins of the Sierra Nevada which show runoff onset occurring 15 days later than the 10-year median. This coincides with the exceptional winter precipitation from repeated atmospheric river events referred to as the “2023 snow deluge” (Marshall et al., 2024). Interestingly, for water years in which there is no uniform continental anomaly, regional anomaly patterns exhibit dipole-like behavior with relatively smooth spatial gradients (e.g. WY2019, WY2020). These patterns potentially reflect interannual variability in the location of the jet stream and accompanying storm tracks, consistent with documented precipitation “seesaws” (M. D. Dettinger et al., 1998; Kiladis & Diaz, 1989; Menounos et al., 2019).

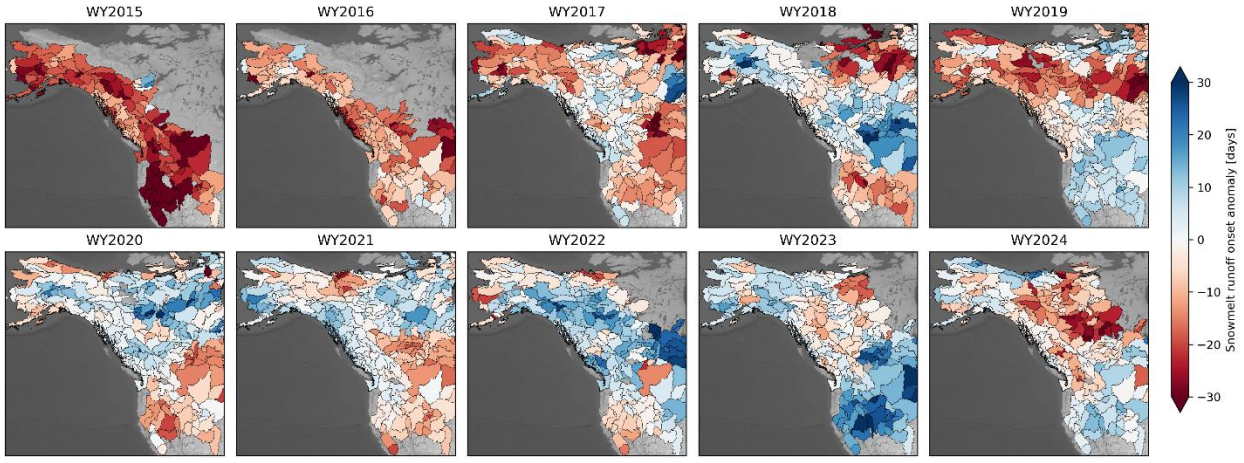

Figure 5.7. Basin mean of per-pixel annual snowmelt runoff onset anomaly (annual minus 10-year median).

Similar to High-Mountain Asia, we examine preliminary vulnerability indicators (Figure 5.8) while acknowledging the limitations of these basin-scale oversimplifications. Western North America basins show a similar pattern to High-Mountain Asia in which basins with 15-50% of precipitation falling as snow correspond to the highest interannual variability, though the 10-year MAD values are ultimately lower. In our WY2015-2024 record, most of the highest population basins in western North America have experienced a runoff onset anomaly of at least 30 days.

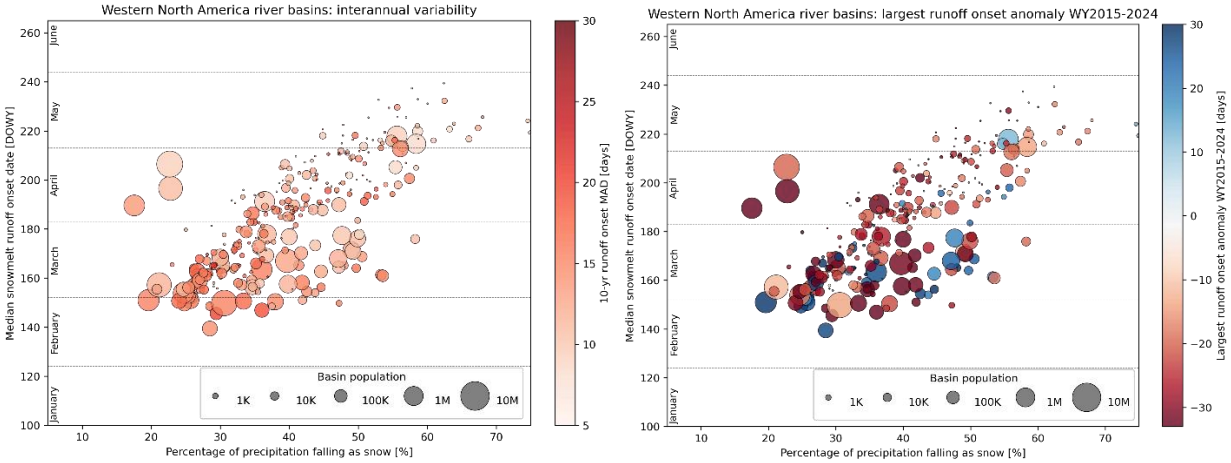

Figure 5.8. Basin-wide runoff onset vulnerability assessment. (Left) Basin 10-year median absolute deviation vs. percentage of precipitation falling as snow and 10-year median runoff onset. (Right) Basin largest runoff onset anomaly in the 10-year record vs. percentage of precipitation falling as snow and 10-year median runoff onset. Note the difference in population sizes and respective markers from the High-Mountain Asia Figure 5.5.

5.5 Community Adoption

This work establishes a foundation for systematic observation of snowmelt runoff onset at global scales. Many applications of our dataset and methodology are already actively being explored by the research community. Ongoing work demonstrates promise in connecting our runoff onset observations to streamflow and subsurface hydrology (Detre et al., 2025; Mirza et al., 2025; Rickenbaugh, 2023). Other researchers are investigating forest fire and snowmelt runoff interaction (Christopher-Moody, 2025; MacDonald et al., 2022), with implications for forest treatment. Our dataset is also being studied as a means to explore the feasibility of L-band InSAR SWE retrievals over the western U.S. (Kaur et al., 2025), with potential to improve global SWE estimation.

5.6 Future work

Several important research directions merit future investigation. Importantly, extending the observational record beyond the current 10-year period will enable more robust characterization of decadal-scale variability and potential longer-term trends. Exploring the integration of other SAR satellites to our methodology, including the recently launched L-band NISAR mission and X-band SAR constellations, could improve spatial and temporal resolution of our method. Further, L-band SAR could allow for improved runoff onset observations beneath the forest canopy. Integration of our dataset into basin-scale hydrologic models could possibly strengthen our understanding of basin-scale water delivery. Finally, the preliminary vulnerability assessment here

highlights the need for more comprehensive frameworks that incorporate downstream water dependence, infrastructure, and socioeconomic factors.

5.7 CONCLUSIONS

The WY2015-2024 basin-scale analyses show that many snowy regions supporting large populations, particularly in High-Mountain Asia and western North America, experience runoff onset interannual variability exceeding 30 days, with direct implications for water availability timing. These findings are particularly salient given that over a billion people depend on water resources from snowmelt for agriculture, hydropower, municipal supplies, and ecosystem functions.

The methodological advances presented in this dissertation–from initial validation over Cascade stratovolcanoes to global-scale dataset preparation using ~3.9 million Sentinel-1 scenes and systematic analysis across 150 mountain ranges–demonstrate that satellite SAR enables snowmelt runoff onset mapping at unprecedented spatial and temporal resolutions. Our analysis of the resulting 10-year snowmelt runoff onset record reveals fundamental patterns of geographic control, substantial interannual variability, and spring air temperature sensitivity.

The results presented in this dissertation represent an initial analysis of this rich dataset. With open-source data and software releases, we are excited to share this new resource with the snow community, enabling new insights for local study sites and new applications.

Snowmelt timing, and more importantly, water availability, will become less predictable as the climate continues to warm, making systematic observation increasingly critical for water resource management. The framework established here provides a foundation for continued monitoring of snowmelt, enabling communities and water managers to anticipate and adapt to future changes.

BIBLIOGRAPHY

Abernathey, R. (2024, June 5). A Serverless Approach to Building Planetary-Scale EO Datacubes in Zarr. *Earthmover*. https://earthmover.io/blog/serverless-datacube-pipeline/

Aguayo, R., León-Muñoz, J., Garreaud, R., & Montecinos, A. (2021). Hydrological droughts in the southern Andes (40–45°S) from an ensemble experiment using CMIP5 and CMIP6 models. *Scientific Reports*, *11*, 5530. https://doi.org/10.1038/s41598-021-84807-4

Alabi, I. O., Marshall, H.-P., Mead, J., & Trujillo, E. (2025). Advancing terrestrial snow depth monitoring with machine learning and L-band InSAR data: A case study using NASA's SnowEx 2017 data. *Frontiers in Remote Sensing*, *5*, 1481848. https://doi.org/10.3389/frsen.2024.1481848

Ali, I., Cao, S., Naeimi, V., Paulik, C., & Wagner, W. (2018). Methods to Remove the Border Noise From Sentinel-1 Synthetic Aperture Radar Data: Implications and Importance For Time-Series Analysis. *IEEE Journal of Selected Topics in Applied Earth Observations and Remote Sensing*, *11*(3), 777–786. IEEE Journal of Selected Topics in Applied Earth Observations and Remote Sensing. https://doi.org/10.1109/JSTARS.2017.2787650

Awasthi, S., & Varade, D. (2021). Recent advances in the remote sensing of alpine snow: A review. *GIScience & Remote Sensing*, *58*(6), 852–888. https://doi.org/10.1080/15481603.2021.1946938

Ayala, Á., Schauwecker, S., & MacDonell, S. (2023). Spatial distribution and controls of snowmelt runoff in a sublimation-dominated environment in the semiarid Andes of Chile.

Hydrology and Earth System Sciences, *27*(18), 3463–3484. https://doi.org/10.5194/hess-27-3463-2023

Baldocchi, D. D., Vogel, C. A., & Hall, B. (1997). Seasonal variation of energy and water vapor exchange rates above and below a boreal jack pine forest canopy. *Journal of Geophysical Research: Atmospheres*, *102*(D24), 28939–28951. https://doi.org/10.1029/96JD03325

Bales, R. C., Molotch, N. P., Painter, T. H., Dettinger, M. D., Rice, R., & Dozier, J. (2006). Mountain hydrology of the western United States. *Water Resources Research*, *42*(8). https://doi.org/10.1029/2005WR004387

Barnett, T. P., Adam, J. C., & Lettenmaier, D. P. (2005). Potential impacts of a warming climate on water availability in snow-dominated regions. *Nature*, *438*(7066), Article 7066. https://doi.org/10.1038/nature04141

Blau, M. T., Kad, P., Turton, J. V., & Ha, K.-J. (2024). Uneven global retreat of persistent mountain snow cover alongside mountain warming from ERA5-land. *Npj Climate and Atmospheric Science*, *7*(1), 278. https://doi.org/10.1038/s41612-024-00829-5

Böhner, J., & Antonić, O. (2009). Chapter 8 Land-Surface Parameters Specific to Topo-Climatology. In T. Hengl & H. I. Reuter (Eds.), *Developments in Soil Science* (Vol. 33, pp. 195–226). Elsevier. https://doi.org/10.1016/S0166-2481(08)00008-1

Boike, J., Roth, K., & Ippisch, O. (2003). Seasonal snow cover on frozen ground: Energy balance calculations of a permafrost site near Ny-Ålesund, Spitsbergen. *Journal of Geophysical Research: Atmospheres*, *108*(D2), ALT 4-1-ALT 4-11. https://doi.org/10.1029/2001JD000939

Bonnell, R., Elder, K., McGrath, D., Marshall, H. P., Starr, B., Adebisi, N., Palomaki, R. T., & Hoppinen, Z. (2024). L-Band InSAR Snow Water Equivalent Retrieval Uncertainty

Increases With Forest Cover Fraction. *Geophysical Research Letters*, *51*(24), e2024GL111708. https://doi.org/10.1029/2024GL111708

Bonnell, R., McGrath, D., Williams, K., Webb, R., Fassnacht, S. R., & Marshall, H.-P. (2021). Spatiotemporal Variations in Liquid Water Content in a Seasonal Snowpack: Implications for Radar Remote Sensing. *Remote Sensing*, *13*(21), Article 21. https://doi.org/10.3390/rs13214223

Bonner, H. M., Raleigh, M. S., & Small, E. E. (2022). Isolating forest process effects on modelled snowpack density and snow water equivalent. *Hydrological Processes*, *36*(1), e14475. https://doi.org/10.1002/hyp.14475

Brangers, I., Marshall, H.-P., De Lannoy, G., Dunmire, D., Mätzler, C., & Lievens, H. (2024). Tower-based C-band radar measurements of an alpine snowpack. *The Cryosphere*, *18*(7), 3177–3193. https://doi.org/10.5194/tc-18-3177-2024

Brooks, P. D., Solomon, D. K., Kampf, S., Warix, S., Bern, C., Barnard, D., Barnard, H. R., Carling, G. T., Carroll, R. W. H., Chorover, J., Harpold, A., Lohse, K., Meza, F., McIntosh, J., Neilson, B., Sears, M., & Wolf, M. (2025). Groundwater dominates snowmelt runoff and controls streamflow efficiency in the western United States. *Communications Earth & Environment*, *6*(1), 1–8. https://doi.org/10.1038/s43247-025-02303-3

Buchhorn, M., Smets, B., Bertels, L., Roo, B. D., Lesiv, M., Tsendbazar, N.-E., Herold, M., & Fritz, S. (2020). *Copernicus Global Land Service: Land Cover 100m: collection 3: epoch 2019: Globe* [Dataset]. Zenodo. https://zenodo.org/records/3939050

California Department of Water Resources. (2025). *California Cooperative Snow Surveys (CCSS)* [Dataset]. https://cdec.water.ca.gov/snow/

Carletti, F., Marin, C., Ghielmini, C., Bavay, M., & Lehning, M. (2025). Multitemporal analysis of Sentinel-1 backscatter during snowmelt using high-resolution field measurements and radiative transfer modelling. *The Cryosphere*, *19*(11), 5579–5612. https://doi.org/10.5194/tc-19-5579-2025

Cayan, D. R., Riddle, L. G., & Aguado, E. (1993). The influence of precipitation and temperature on seasonal streamflow in California. *Water Resources Research*, *29*(4), 1127–1140. https://doi.org/10.1029/92WR02802

Christopher-Moody, K. E. (2025). *EFFECTS OF FOREST MANAGEMENT ON SNOW ACCUMULATION AND ABLATION IN A MONTANE WATERSHED*.

Clow, D. W. (2010). Changes in the Timing of Snowmelt and Streamflow in Colorado: A Response to Recent Warming. *Journal of Climate*, *23*(9), 2293–2306. https://doi.org/10.1175/2009JCLI2951.1

Cortés, G., & Margulis, S. (2017). Impacts of El Niño and La Niña on interannual snow accumulation in the Andes: Results from a high-resolution 31 year reanalysis. *Geophysical Research Letters*, *44*(13), 6859–6867. https://doi.org/10.1002/2017GL073826

Cristea, N., Breckheimer, I., Raleigh, M., HilleRisLambers, J., & Lundquist, J. (2017). An evaluation of terrain-based downscaling of fractional snow covered area data sets based on LiDAR-derived snow data and orthoimagery. *Water Resources Research*, *53*. https://doi.org/10.1002/2017WR020799

Crumley, R. L., Palomaki, R. T., Nolin, A. W., Sproles, E. A., & Mar, E. J. (2020). SnowCloudMetrics: Snow Information for Everyone. *Remote Sensing*, *12*(20), Article 20. https://doi.org/10.3390/rs12203341

Darychuk, S. E., Shea, J. M., Menounos, B., Chesnokova, A., Jost, G., & Weber, F. (2023). Snowmelt characterization from optical and synthetic-aperture radar observations in the La Joie Basin, British Columbia. *The Cryosphere*, *17*(4), 1457–1473. https://doi.org/10.5194/tc-17-1457-2023

Dask Development Team. (2016). *Dask: Library for dynamic task scheduling* [Computer software]. http://dask.pydata.org

DeBeer, C. M., & Pomeroy, J. W. (2017). Influence of snowpack and melt energy heterogeneity on snow cover depletion and snowmelt runoff simulation in a cold mountain environment. *Journal of Hydrology*, *553*, 199–213. https://doi.org/10.1016/j.jhydrol.2017.07.051

Detre, A., McGrath, D., Gagliano, E., Bonnell, R., Webb, R., Marshall, H.-P., & Shean, D. (2025). Sentinel-1 SAR Estimates of Snowmelt Onset Coincide with SNOTEL Soil Moisture Pulses Across the Western U.S. *Hydrological Processes*.

Dettinger, M. (2005). *Changes in streamflow timing in the western United States in recent decades* (Report Nos. 2005–3018; Fact Sheet). USGS Publications Warehouse. https://doi.org/10.3133/fs20053018

Dettinger, M. D., Cayan, D. R., Diaz, H. F., & Meko, D. M. (1998). *North–South Precipitation Patterns in Western North America on Interannual-to-Decadal Timescales*. https://journals.ametsoc.org/view/journals/clim/11/12/1520-0442_1998_011_3095_nsppiw_2.0.co_2.xml

Dingman, S. L. (2015). *Physical Hydrology: Third Edition*. Waveland Press.

Dudley, R. W., Hodgkins, G. A., McHale, M. R., Kolian, M. J., & Renard, B. (2017). Trends in snowmelt-related streamflow timing in the conterminous United States. *Journal of Hydrology*, *547*, 208–221. https://doi.org/10.1016/j.jhydrol.2017.01.051

Dunne, T., & Black, R. (1971). Runoff Processes During Snowmelt. *Water Resources Research - WATER RESOUR RES*, *7*, 1160–1172. https://doi.org/10.1029/WR007i005p01160

Earth Science Data Systems, N. (2025). *Gridded Population of the World, Version 4 (GPWv4): Population Count, Revision 11 | NASA Earthdata* [Dataset]. Earth Science Data Systems, NASA. https://www.earthdata.nasa.gov/data/catalog/sedac-ciesin-sedac-gpwv4-popcount-r11-4.11

Eiriksson, D., Whitson, M., Luce, C. H., Marshall, H. P., Bradford, J., Benner, S. G., Black, T., Hetrick, H., & McNamara, J. P. (2013). An evaluation of the hydrologic relevance of lateral flow in snow at hillslope and catchment scales. *Hydrological Processes*, *27*(5), 640–654. https://doi.org/10.1002/hyp.9666

Evan, A. T. (2019). A New Method to Characterize Changes in the Seasonal Cycle of Snowpack. *Journal of Applied Meteorology and Climatology*, *58*(1), 131–143. https://doi.org/10.1175/JAMC-D-18-0150.1

Fassnacht, S. R., Deitemeyer, D. C., & Venable, N. B. H. (2014). Capitalizing on the daily time step of snow telemetry data to model the snowmelt components of the hydrograph for small watersheds. *Hydrological Processes*, *28*(16), 4654–4668. https://doi.org/10.1002/hyp.10260

Fleming, S. W., Zukiewicz, L., Strobel, M. L., Hofman, H., & Goodbody, A. G. (2023). SNO^{TEL}, the Soil Climate Analysis Network, and water supply forecasting at the Natural Resources Conservation Service: Past, present, and future. *JAWRA Journal of the*

American Water Resources Association, *n/a*(n/a). https://doi.org/10.1111/1752-1688.13104

Frans, C., Istanbulluoglu, E., Lettenmaier, D. P., Fountain, A. G., & Riedel, J. (2018). Glacier Recession and the Response of Summer Streamflow in the Pacific Northwest United States, 1960–2099. *Water Resources Research*, *54*(9), 6202–6225. https://doi.org/10.1029/2017WR021764

Frisbee, M. D., Phillips, F. M., Campbell, A. R., Liu, F., & Sanchez, S. A. (2011). Streamflow generation in a large, alpine watershed in the southern Rocky Mountains of Colorado: Is streamflow generation simply the aggregation of hillslope runoff responses? *Water Resources Research*, *47*(6). https://doi.org/10.1029/2010WR009391

Gagliano, E. (2022). *egagli/sar_snow_melt_timing: Initial Release* [Computer software]. Zenodo. https://doi.org/10.5281/zenodo.7098102

Gagliano, E. (2025a). *Global MODIS-derived seasonal snow cover (snow appearance date, disappearance date, and max consec snow days), water years 2015–2024* [Dataset]. Zenodo. https://doi.org/10.5281/zenodo.15692530

Gagliano, E. (2025b). *egagli/MODIS_seasonal_snow_mask: V1.0* [Computer software]. Zenodo. https://doi.org/10.5281/zenodo.17246166

Gagliano, E., Shean, D., Henderson, S., & Vanderwilt, S. (2023). Capturing the Onset of Mountain Snowmelt Runoff Using Satellite Synthetic Aperture Radar. *Geophysical Research Letters*, *50*(21), e2023GL105303. https://doi.org/10.1029/2023GL105303

Gao, B., & Ma, W. (2024). Capturing Snowmelt Runoff Onset Date under Different Land Cover Types Using Synthetic Aperture Radar: Case Study of Sierra Nevada Mountains, USA. *Applied Sciences*, *14*(15), Article 15. https://doi.org/10.3390/app14156844

Garnier, B. J., & Ohmura, A. (1968). *A Method of Calculating the Direct Shortwave Radiation Income of Slopes*. https://journals.ametsoc.org/view/journals/apme/7/5/1520-0450_1968_007_0796_amoctd_2_0_co_2.xml

Garvelmann, J., Pohl, S., & Weiler, M. (2014). Variability of Observed Energy Fluxes during Rain-on-Snow and Clear Sky Snowmelt in a Midlatitude Mountain Environment. *Journal of Hydrometeorology*, *15*(3), 1220–1237. https://doi.org/10.1175/JHM-D-13-0187.1

Gascoin, S., Lhermitte, S., Kinnard, C., Bortels, K., & Liston, G. E. (2013). Wind effects on snow cover in Pascua-Lama, Dry Andes of Chile. *Advances in Water Resources*, *55*, 25–39. https://doi.org/10.1016/j.advwatres.2012.11.013

Gershunov, A., & Barnett, T. P. (1998). Interdecadal Modulation of ENSO Teleconnections. *Bulletin of the American Meteorological Society*, *79*(12), 2715–2726. https://doi.org/10.1175/1520-0477(1998)079%253C2715:IMOET%253E2.0.CO;2

Gnann, S., Baldwin, J. W., Cuthbert, M. O., Gleeson, T., Schwanghart, W., & Wagener, T. (2025). The Influence of Topography on the Global Terrestrial Water Cycle. *Reviews of Geophysics*, *63*(1), e2023RG000810. https://doi.org/10.1029/2023RG000810

Gottlieb, A. R., & Mankin, J. S. (2025). Subseasonal Temperature Variability Drives Nonlinear Snow Loss With Warming. *Water Resources Research*, *61*(8), e2024WR039724. https://doi.org/10.1029/2024WR039724

Guneriussen, T., Hogda, K. A., Johnsen, H., & Lauknes, I. (2001). InSAR for estimation of changes in snow water equivalent of dry snow. *IEEE Transactions on Geoscience and Remote Sensing*, *39*(10), 2101–2108. IEEE Transactions on Geoscience and Remote Sensing. https://doi.org/10.1109/36.957273

Hale, K. E., Jennings, K. S., Musselman, K. N., Livneh, B., & Molotch, N. P. (2023). Recent decreases in snow water storage in western North America. *Communications Earth & Environment*, *4*(1), Article 1. https://doi.org/10.1038/s43247-023-00751-3

Hall, D., & Riggs, G. (2021). *MODIS/Terra Snow Cover 8-Day L3 Global 500m SIN Grid, Version 61* [Dataset]. NASA National Snow and Ice Data Center Distributed Active Archive Center. https://doi.org/10.5067/MODIS/MOD10A2.061

Hammond, J. C., Saavedra, F. A., & Kampf, S. K. (2018). Global snow zone maps and trends in snow persistence 2001–2016. *International Journal of Climatology*, *38*(12), 4369–4383. https://doi.org/10.1002/joc.5674

Han, J., Liu, Z., Woods, R., McVicar, T. R., Yang, D., Wang, T., Hou, Y., Guo, Y., Li, C., & Yang, Y. (2024). Streamflow seasonality in a snow-dwindling world. *Nature*, *629*(8014), 1075–1081. https://doi.org/10.1038/s41586-024-07299-y

Hassan, W. ul, Nayak, M. A., Saharwardi, M. S., Dar, J. A., Dasari, H. P., Hoteit, I., & Abualnaja, Y. (2024). Unveiling the devastating effect of the spring 2022 mega-heatwave on the South Asian snowpack. *Communications Earth & Environment*, *5*(1), 707. https://doi.org/10.1038/s43247-024-01857-y

Hoppinen, Z., Palomaki, R. T., Brencher, G., Dunmire, D., Gagliano, E., Marziliano, A., Tarricone, J., & Marshall, H.-P. (2024). Evaluating snow depth retrievals from Sentinel-1 volume scattering over NASA SnowEx sites. *The Cryosphere*, *18*(11), 5407–5430. https://doi.org/10.5194/tc-18-5407-2024

Huang, B., Thorne, P. W., Banzon, V. F., Boyer, T., Chepurin, G., Lawrimore, J. H., Menne, M. J., Smith, T. M., Vose, R. S., & Zhang, H.-M. (2017). Extended Reconstructed Sea Surface Temperature, Version 5 (ERSSTv5): Upgrades, Validations, and

Intercomparisons. *Journal of Climate*, *30*(20), 8179–8205. https://doi.org/10.1175/JCLI-D-16-0836.1

Iijima, Y., Masuda, K., & Ohata, T. (2007). Snow disappearance in Eastern Siberia and its relationship to atmospheric influences. *International Journal of Climatology*, *27*(2), 169–177. https://doi.org/10.1002/joc.1382

Immerzeel, W. W., Lutz, A. F., Andrade, M., Bahl, A., Biemans, H., Bolch, T., Hyde, S., Brumby, S., Davies, B. J., Elmore, A. C., Emmer, A., Feng, M., Fernández, A., Haritashya, U., Kargel, J. S., Koppes, M., Kraaijenbrink, P. D. A., Kulkarni, A. V., Mayewski, P. A., … Baillie, J. E. M. (2020). Importance and vulnerability of the world's water towers. *Nature*, *577*(7790), 364–369. https://doi.org/10.1038/s41586-019-1822-y

Ismail, M. F., Bogacki, W., Disse, M., Schäfer, M., & Kirschbauer, L. (2023). Estimating degree-day factors of snow based on energy flux components. *The Cryosphere*, *17*(1), 211–231. https://doi.org/10.5194/tc-17-211-2023

Jefferson, A. J. (2011). Seasonal versus transient snow and the elevation dependence of climate sensitivity in maritime mountainous regions. *Geophysical Research Letters*, *38*(16). https://doi.org/10.1029/2011GL048346

John, A., Ong, J., Theobald, E. J., Olden, J. D., Tan, A., & HilleRisLambers, J. (2020). Detecting Montane Flowering Phenology with CubeSat Imagery. *Remote Sensing*, *12*(18), Article 18. https://doi.org/10.3390/rs12182894

Johnson, J. B., & Schaefer, G. L. (2002). The influence of thermal, hydrologic, and snow deformation mechanisms on snow water equivalent pressure sensor accuracy. *Hydrological Processes*, *16*(18), 3529–3542. https://doi.org/10.1002/hyp.1236

Karbou, F., Veyssière, G., Coleou, C., Dufour, A., Gouttevin, I., Durand, P., Gascoin, S., & Grizonnet, M. (2021). Monitoring Wet Snow Over an Alpine Region Using Sentinel-1 Observations. *Remote Sensing*, *13*(3), Article 3. https://doi.org/10.3390/rs13030381

Kattelmann, R., & Dozier, J. (1999). Observations of snowpack ripening in the Sierra Nevada, California, U.S.A. *Journal of Glaciology*, *45*(151), 409–416. https://doi.org/10.3189/S002214300000126X

Kaur, P., Webb, R., Tarricone, J., Rittger, K., McGrath, D., Gagliano, E., Palomaki, R., Bonnell, R., Forster, R., & Marshall, H. P. (2025). *Feasibility Mapping of L-band InSAR for SWE retrievals*.

Kiladis, G. N., & Diaz, H. F. (1989). *Global Climatic Anomalies Associated with Extremes in the Southern Oscillation*. https://journals.ametsoc.org/view/journals/clim/2/9/1520-0442_1989_002_1069_gcaawe_2_0_co_2.xml

Kurum, M. (2015). C-Band SAR Backscatter Evaluation of 2008 Gallipoli Forest Fire. *IEEE Geoscience and Remote Sensing Letters*, *12*(5), 1091–1095. https://doi.org/10.1109/LGRS.2014.2382716

Leathers, D. J., & Robinson, D. A. (1997). *Abrupt Changes in the Seasonal Cycle of North American Snow Cover*. https://journals.ametsoc.org/view/journals/clim/10/10/1520-0442_1997_010_2569_acitsc_2.0.co_2.xml

Leffler, R. J., Changery, M., Redmond, K., Downs, R., Taylor, G., & Horvitz, A. (2001). Evaluation of a national seasonal snowfall record at the Mount Baker, Washington, Ski Area. *National Weather Digest*, *25*(1/2), 15–20.

Lehner, B., & Grill, G. (2013). Global river hydrography and network routing: Baseline data and new approaches to study the world's large river systems. *Hydrological Processes*, *27*(15), 2171–2186. https://doi.org/10.1002/hyp.9740

Lemmetyinen, J., Ruiz, J. J., Cohen, J., Haapamaa, J., Kontu, A., Pulliainen, J., & Praks, J. (2022). Attenuation of Radar Signal by a Boreal Forest Canopy in Winter. *IEEE Geoscience and Remote Sensing Letters*, *19*, 1–5. https://doi.org/10.1109/LGRS.2022.3187295

Li, H., Wang, Z., He, G., & Man, W. (2017, April 12). *Estimating Snow Depth and Snow Water Equivalence Using Repeat-Pass Interferometric SAR in the Northern Piedmont Region of the Tianshan Mountains* [Research Article]. Journal of Sensors; Hindawi. https://doi-org.offcampus.lib.washington.edu/10.1155/2017/8739598

Li, S., Sato, T., Nakamura, T., Liu, X., & Guo, W. (2021). Controlling Factors of Historical Variation of Winter Tibetan Plateau Snow Cover Revealed by Large-Ensemble Experiments. *Journal of Geophysical Research: Atmospheres*, *126*(21), e2021JD035127. https://doi.org/10.1029/2021JD035127

Li, W., Qiu, B., Guo, W., Zhu, Z., & Hsu, P.-C. (2020). Intraseasonal variability of Tibetan Plateau snow cover. *International Journal of Climatology*, *40*(7), 3451–3466. https://doi.org/10.1002/joc.6407

Liang, D., Guo, H., Zhang, L., Cheng, Y., Zhu, Q., & Liu, X. (2021). Time-series snowmelt detection over the Antarctic using Sentinel-1 SAR images on Google Earth Engine. *Remote Sensing of Environment*, *256*, 112318. https://doi.org/10.1016/j.rse.2021.112318

Lievens, H., Brangers, I., Marshall, H.-P., Jonas, T., Olefs, M., & De Lannoy, G. (2022). Sentinel-1 snow depth retrieval at sub-kilometer resolution over the European Alps. *The Cryosphere*, *16*(1), 159–177. https://doi.org/10.5194/tc-16-159-2022

Lisi, P. J., Schindler, D. E., Cline, T. J., Scheuerell, M. D., & Walsh, P. B. (2015). Watershed geomorphology and snowmelt control stream thermal sensitivity to air temperature. *Geophysical Research Letters*, *42*(9), 3380–3388. https://doi.org/10.1002/2015GL064083

Litaor, M. I., Williams, M., & Seastedt, T. R. (2008). Topographic controls on snow distribution, soil moisture, and species diversity of herbaceous alpine vegetation, Niwot Ridge, Colorado. *Journal of Geophysical Research: Biogeosciences*, *113*(G2). https://doi.org/10.1029/2007JG000419

Livneh, B., & Badger, A. M. (2020). Drought less predictable under declining future snowpack. *Nature Climate Change*, *10*(5), Article 5. https://doi.org/10.1038/s41558-020-0754-8

López-Moreno, J. I., Callow, N., McGowan, H., Webb, R., Schwartz, A., Bilish, S., Revuelto, J., Gascoin, S., Deschamps-Berger, C., & Alonso-González, E. (2024). Marginal snowpacks: The basis for a global definition and existing research needs. *Earth-Science Reviews*, *252*, 104751. https://doi.org/10.1016/j.earscirev.2024.104751

López-Moreno, J. I., Revuelto, J., Gilaberte, M., Morán-Tejeda, E., Pons, M., Jover, E., Esteban, P., García, C., & Pomeroy, J. W. (2014). The effect of slope aspect on the response of snowpack to climate warming in the Pyrenees. *Theoretical and Applied Climatology*, *117*(1), 207–219. https://doi.org/10.1007/s00704-013-0991-0

Lowry, C. S., Deems, J. S., Loheide II, S. P., & Lundquist, J. D. (2010). Linking snowmelt-derived fluxes and groundwater flow in a high elevation meadow system, Sierra Nevada

Mountains, California. *Hydrological Processes*, *24*(20), 2821–2833. https://doi.org/10.1002/hyp.7714

Lund, J., Forster, R. R., Deeb, E. J., Liston, G. E., Skiles, S. M., & Marshall, H.-P. (2022). Interpreting Sentinel-1 SAR Backscatter Signals of Snowpack Surface Melt/Freeze, Warming, and Ripening, through Field Measurements and Physically-Based SnowModel. *Remote Sensing*, *14*(16), Article 16. https://doi.org/10.3390/rs14164002

Lund, J., Forster, R. R., Rupper, S. B., Deeb, E. J., Marshall, H. P., Hashmi, M. Z., & Burgess, E. (2020). Mapping Snowmelt Progression in the Upper Indus Basin With Synthetic Aperture Radar. *Frontiers in Earth Science*, *7*. https://www.frontiersin.org/articles/10.3389/feart.2019.00318

Lundquist, J. D., Cayan, D. R., & Dettinger, M. D. (2004). Spring Onset in the Sierra Nevada: When Is Snowmelt Independent of Elevation? *Journal of Hydrometeorology*, *5*(2), 327–342. https://doi.org/10.1175/1525-7541(2004)005%253C0327:SOITSN%253E2.0.CO;2

Lundquist, J. D., & Dettinger, M. D. (2005). How snowpack heterogeneity affects diurnal streamflow timing. *Water Resources Research*, *41*(5). https://doi.org/10.1029/2004WR003649

Lundquist, J. D., Dickerson-Lange, S. E., Lutz, J. A., & Cristea, N. C. (2013). Lower forest density enhances snow retention in regions with warmer winters: A global framework developed from plot-scale observations and modeling. *Water Resources Research*, *49*(10), 6356–6370. https://doi.org/10.1002/wrcr.20504

Lundquist, J. D., & Flint, A. L. (2006). *Onset of Snowmelt and Streamflow in 2004 in the Western United States: How Shading May Affect Spring Streamflow Timing in a Warmer World*. https://doi.org/10.1175/JHM539.1

MacDonald, M., Fassnacht, S. R., & Tedesche, M. E. (2022). *High Elevation Post-Fire Landscapes on Snow Melt Trends in Seasonal and Transitional Snow Zones*. *2022*, GC53B-08. https://ui.adsabs.harvard.edu/abs/2022AGUFMGC53B..08M

Male, D. H., & Granger, R. J. (1981). Snow surface energy exchange. *Water Resources Research*, *17*(3), 609–627. https://doi.org/10.1029/WR017i003p00609

Manickam, S., & Barros, A. (2020). Parsing Synthetic Aperture Radar Measurements of Snow in Complex Terrain: Scaling Behaviour and Sensitivity to Snow Wetness and Landcover. *Remote Sensing*, *12*(3), Article 3. https://doi.org/10.3390/rs12030483

Mantua, N. J., Hare, S. R., Zhang, Y., Wallace, J. M., & Francis, R. C. (1997). A Pacific Interdecadal Climate Oscillation with Impacts on Salmon Production*. *Bulletin of the American Meteorological Society*, *78*(6), 1069–1080. https://doi.org/10.1175/1520-0477(1997)078%253C1069:APICOW%253E2.0.CO;2

Marin, C., Bertoldi, G., Premier, V., Callegari, M., Brida, C., Hürkamp, K., Tschiersch, J., Zebisch, M., & Notarnicola, C. (2020). Use of Sentinel-1 radar observations to evaluate snowmelt dynamics in alpine regions. *The Cryosphere*, *14*(3), 935–956. https://doi.org/10.5194/tc-14-935-2020

Marks, D., & Dozier, J. (1992). Climate and energy exchange at the snow surface in the Alpine Region of the Sierra Nevada: 2. Snow cover energy balance. *Water Resources Research*, *28*(11), 3043–3054. https://doi.org/10.1029/92WR01483

Marks, D., Kimball, J., Tingey, D., & Link, T. (1998). The sensitivity of snowmelt processes to climate conditions and forest cover during rain-on-snow: A case study of the 1996 Pacific Northwest flood. *Hydrological Processes*, *12*(10–11), 1569–1587.

https://doi.org/10.1002/(SICI)1099-1085(199808/09)12:10/11%253C1569::AID-HYP682%253E3.0.CO;2-L

Marshall, A. M., Abatzoglou, J. T., Rahimi, S., Lettenmaier, D. P., & Hall, A. (2024). California's 2023 snow deluge: Contextualizing an extreme snow year against future climate change. *Proceedings of the National Academy of Sciences*, *121*(20), e2320600121. https://doi.org/10.1073/pnas.2320600121

Masiokas, M. H., Villalba, R., Luckman, B. H., Quesne, C. L., & Aravena, J. C. (2006). *Snowpack Variations in the Central Andes of Argentina and Chile, 1951–2005: Large-Scale Atmospheric Influences and Implications for Water Resources in the Region*. https://doi.org/10.1175/JCLI3969.1

Matias, M. T., Ramage, J. M., Gurarie, E., & Brodzik, M. J. (2024). Snowmelt Onset and Caribou (Rangifer tarandus) Spring Migration. *Remote Sensing*, *16*(13), Article 13. https://doi.org/10.3390/rs16132391

Mätzler, C. (1987). Applications of the interaction of microwaves with the natural snow cover. *Remote Sensing Reviews*, *2*(2), 259–387. https://doi.org/10.1080/02757258709532086

Mazurkiewicz, A. B., Callery, D. G., & McDonnell, J. J. (2008). Assessing the controls of the snow energy balance and water available for runoff in a rain-on-snow environment. *Journal of Hydrology*, *354*(1), 1–14. https://doi.org/10.1016/j.jhydrol.2007.12.027

Menounos, B., Hugonnet, R., Shean, D., Gardner, A., Howat, I., Berthier, E., Pelto, B., Tennant, C., Shea, J., Noh, M.-J., Brun, F., & Dehecq, A. (2019). Heterogeneous Changes in Western North American Glaciers Linked to Decadal Variability in Zonal Wind Strength. *Geophysical Research Letters*, *46*(1), 200–209. https://doi.org/10.1029/2018GL080942

Meromy, L., Molotch, N. P., Link, T. E., Fassnacht, S. R., & Rice, R. (2013). Subgrid variability of snow water equivalent at operational snow stations in the western USA. *Hydrological Processes*, *27*(17), 2383–2400. https://doi.org/10.1002/hyp.9355

Microsoft Open Source, McFarland, M., Emanuele, R., Morris, D., & Augspurger, T. (2022). *microsoft/PlanetaryComputer: October 2022* (Version 2022.10.28) [Computer software]. Zenodo. https://doi.org/10.5281/zenodo.7261897

Mioduszewski, J. R., Rennermalm, A. K., Robinson, D. A., & Wang, L. (2015). Controls on Spatial and Temporal Variability in Northern Hemisphere Terrestrial Snow Melt Timing, 1979–2012. *Journal of Climate*, *28*(6), 2136–2153. https://doi.org/10.1175/JCLI-D-14-00558.1

Mirza, B. N., Small, E. E., & Raleigh, M. S. (2025a). Evaluating the Utility of Sentinel-1 in a Data Assimilation System for Estimating Snow Depth in a Mountainous Basin. *EGUsphere*, 1–31. https://doi.org/10.5194/egusphere-2025-978

Mirza, B. N., Small, E. E., & Raleigh, M. S. (2025b). Evaluating the utility of Sentinel-1 in a Data Assimilation System for estimating snow depth in a mountainous basin. *The Cryosphere*, *19*(12), 6691–6709. https://doi.org/10.5194/tc-19-6691-2025

Moore, R. D., & Owens, I. F. (1984). Controls on Advective Snowmelt in a Maritime Alpine Basin. *Journal of Climate and Applied Meteorology*, *23*(1), 135–142.

Mote, P. W. (2006). *Climate-Driven Variability and Trends in Mountain Snowpack in Western North America*. https://doi.org/10.1175/JCLI3971.1

Mote, P. W., Rupp, D. E., Li, S., Sharp, D. J., Otto, F., Uhe, P. F., Xiao, M., Lettenmaier, D. P., Cullen, H., & Allen, M. R. (2016). Perspectives on the causes of exceptionally low 2015

snowpack in the western United States. *Geophysical Research Letters*, *43*(20), 10,980-10,988. https://doi.org/10.1002/2016GL069965

Muñoz, S., J. (2019). *ERA5-Land monthly averaged data from 1950 to present* [Dataset]. Copernicus Climate Change Service (C3S) Climate Data Store (CDS). https://doi.org/10.24381/cds.68d2bb30

Munro, D. S., & Young, G. J. (1982). An operational net shortwave radiation model for glacier basins. *Water Resources Research*, *18*(2), 220–230. https://doi.org/10.1029/WR018i002p00220

Musselman, K. N., Addor, N., Vano, J. A., & Molotch, N. P. (2021). Winter melt trends portend widespread declines in snow water resources. *Nature Climate Change*, *11*(5), Article 5. https://doi.org/10.1038/s41558-021-01014-9

Naderpour, R., Schwank, M., Houtz, D., Werner, C., & Mätzler, C. (2022). Wideband Backscattering From Alpine Snow Cover: A Full-Season Study. *IEEE Transactions on Geoscience and Remote Sensing*, *60*, 1–15. IEEE Transactions on Geoscience and Remote Sensing. https://doi.org/10.1109/TGRS.2021.3112772

Nagler, T. (1996). *Methods and analysis of synthetic aperture radar data from ERS-1 and X-SAR for snow and glacier applications* [Leopold-Franzens-Universität Innsbruck]. https://www.uibk.ac.at/projects/station-hintereis-opal-data/theses/pdf/nagler_1996.pdf

Nagler, T., Rott, H., Ripper, E., Bippus, G., & Hetzenecker, M. (2016). Advancements for Snowmelt Monitoring by Means of Sentinel-1 SAR. *Remote Sensing*, *8*(4), Article 4. https://doi.org/10.3390/rs8040348

Ohmura, A. (2001). *Physical Basis for the Temperature-Based Melt-Index Method*. https://journals.ametsoc.org/view/journals/apme/40/4/1520-0450_2001_040_0753_pbfttb_2.0.co_2.xml

Olefs, M., Koch, R., Schöner, W., & Marke, T. (2020). Changes in Snow Depth, Snow Cover Duration, and Potential Snowmaking Conditions in Austria, 1961–2020—A Model Based Approach. *Atmosphere*, *11*(12), 1330. https://doi.org/10.3390/atmos11121330

Palomaki, R. T., & Sproles, E. A. (2023). Assessment of L-band InSAR snow estimation techniques over a shallow, heterogeneous prairie snowpack. *Remote Sensing of Environment*, *296*, 113744. https://doi.org/10.1016/j.rse.2023.113744

Pflug, J. M., Yang, K., Cristea, N., Boudreau, E. T., Vuyovich, C. M., & Kumar, S. V. (2024). Using Commercial Satellite Imagery to Reconstruct 3 m and Daily Spring Snow Water Equivalent. *Water Resources Research*, *60*(11), e2024WR037983. https://doi.org/10.1029/2024WR037983

Planet Observer. (2017). *PlanetDEM 30 Plus* [Dataset]. https://www.planetobserver.com/products/planetdem/planetdem-30/.

Pohl, S., Marsh, P., & Pietroniro, A. (2006). Spatial–temporal variability in solar radiation during spring snowmelt. *Hydrology Research*, *37*(1), 1–19. https://doi.org/10.2166/nh.2006.0001

Potin, P., Colin, O., Pinheiro, M., Rosich, B., O'Connell, A., Ormston, T., Gratadour, J.-B., & Torres, R. (2022). Status And Evolution Of The Sentinel-1 Mission. *IGARSS 2022 - 2022 IEEE International Geoscience and Remote Sensing Symposium*, 4707–4710. https://doi.org/10.1109/IGARSS46834.2022.9884753

Qin, Y., Hong, C., Zhao, H., Siebert, S., Abatzoglou, J. T., Huning, L. S., Sloat, L. L., Park, S., Li, S., Munroe, D. K., Zhu, T., Davis, S. J., & Mueller, N. D. (2022). Snowmelt risk

telecouplings for irrigated agriculture. *Nature Climate Change*, *12*(11), 1007–1015. https://doi.org/10.1038/s41558-022-01509-z

Raleigh, M. S., Gutmann, E. D., Van Stan II, J. T., Burns, S. P., Blanken, P. D., & Small, E. E. (2022). Challenges and Capabilities in Estimating Snow Mass Intercepted in Conifer Canopies With Tree Sway Monitoring. *Water Resources Research*, *58*(3), e2021WR030972. https://doi.org/10.1029/2021WR030972

Ramage, J. M., McKenney, R. A., Thorson, B., Maltais, P., & Kopczynski, S. E. (2006). Relationship between passive microwave-derived snowmelt and surface-measured discharge, Wheaton River, Yukon Territory, Canada. *Hydrological Processes*, *20*(4), 689–704. https://doi.org/10.1002/hyp.6133

Rasmussen, L. A., & Tangborn, W. V. (1976). Hydrology of the North Cascades Region, Washington: 1. Runoff, precipitation, and storage characteristics. *Water Resources Research*, *12*(2), 187–202. https://doi.org/10.1029/WR012i002p00187

Reece, B., & Aguado, E. (1992). Accumulation and melt characteristics of northeastern Sierra Nevada snowpacks. *Proceedings of the American Water Resources Association 28th Annual Conference and Symposium: Managing Water Resources during Global Change*, 631–640.

Réveillet, M., MacDonell, S., Gascoin, S., Kinnard, C., Lhermitte, S., & Schaffer, N. (2020). Impact of forcing on sublimation simulations for a high mountain catchment in the semiarid Andes. *The Cryosphere*, *14*(1), 147–163. https://doi.org/10.5194/tc-14-147-2020

Rickenbaugh, E. A. (2023). *When and where does irrigation water originate? Leveraging stable water isotopes and synthetic aperture radar to assess the complex hydrology of a snow-*

dominated catchment in southwestern Montana [Montana State University - Bozeman, College of Letters & Science]. https://scholarworks.montana.edu/handle/1/18301

Rott, H., & Nagler, T. (1995). Monitoring temporal dynamics of snowmelt with ERS-1 SAR. *1995 International Geoscience and Remote Sensing Symposium, IGARSS '95. Quantitative Remote Sensing for Science and Applications*, *3*, 1747–1749. https://doi.org/10.1109/IGARSS.1995.524014

Royer, A., Picard, G., Vargel, C., Langlois, A., Gouttevin, I., & Dumont, M. (2021). Improved Simulation of Arctic Circumpolar Land Area Snow Properties and Soil Temperatures. *Frontiers in Earth Science*, *9*. https://doi.org/10.3389/feart.2021.685140

Saavedra, F. A., Kampf, S. K., Fassnacht, S. R., & Sibold, J. S. (2017a). A snow climatology of the Andes Mountains from MODIS snow cover data. *International Journal of Climatology*, *37*(3), 1526–1539. https://doi.org/10.1002/joc.4795

Saavedra, F. A., Kampf, S. K., Fassnacht, S. R., & Sibold, J. S. (2017b). A snow climatology of the Andes Mountains from MODIS snow cover data. *International Journal of Climatology*, *37*(3), 1526–1539. https://doi.org/10.1002/joc.4795

Saavedra, F. A., Kampf, S. K., Fassnacht, S. R., & Sibold, J. S. (2018). Changes in Andes snow cover from MODIS data, 2000–2016. *The Cryosphere*, *12*(3), 1027–1046. https://doi.org/10.5194/tc-12-1027-2018

Scher, C., Steiner, N. C., & McDonald, K. C. (2021). Mapping seasonal glacier melt across the Hindu Kush Himalaya with time series synthetic aperture radar (SAR). *The Cryosphere*, *15*(9), 4465–4482. https://doi.org/10.5194/tc-15-4465-2021

Shi, J., & Dozier, J. (1995). Inferring snow wetness using C-band data from SIR-C's polarimetric synthetic aperture radar. *IEEE Transactions on Geoscience and Remote Sensing*, *33*(4),

905–914. IEEE Transactions on Geoscience and Remote Sensing. https://doi.org/10.1109/36.406676

Siirila-Woodburn, E. R., Rhoades, A. M., Hatchett, B. J., Huning, L. S., Szinai, J., Tague, C., Nico, P. S., Feldman, D. R., Jones, A. D., Collins, W. D., & Kaatz, L. (2021). A low-to-no snow future and its impacts on water resources in the western United States. *Nature Reviews Earth & Environment*, *2*(11), Article 11. https://doi.org/10.1038/s43017-021-00219-y

Skiles, S. M., Flanner, M., Cook, J. M., Dumont, M., & Painter, T. H. (2018). Radiative forcing by light-absorbing particles in snow. *Nature Climate Change*, *8*(11), 964–971. https://doi.org/10.1038/s41558-018-0296-5

Small, D. (2011). Flattening Gamma: Radiometric Terrain Correction for SAR Imagery. *IEEE Transactions on Geoscience and Remote Sensing*, *49*(8), 3081–3093. IEEE Transactions on Geoscience and Remote Sensing. https://doi.org/10.1109/TGRS.2011.2120616

Snethlage, M. A., Geschke, J., Ranipeta, A., Jetz, W., Yoccoz, N. G., Körner, C., Spehn, E. M., Fischer, M., & Urbach, D. (2022). A hierarchical inventory of the world's mountains for global comparative mountain science. *Scientific Data*, *9*(1), 149. https://doi.org/10.1038/s41597-022-01256-y

Steele-Dunne, S. C., Friesen, J., & van de Giesen, N. (2012). Using Diurnal Variation in Backscatter to Detect Vegetation Water Stress. *IEEE Transactions on Geoscience and Remote Sensing*, *50*(7), 2618–2629. https://doi.org/10.1109/TGRS.2012.2194156

Stewart, I. T. (2009). Changes in snowpack and snowmelt runoff for key mountain regions. *Hydrological Processes*, *23*(1), 78–94. https://doi.org/10.1002/hyp.7128

Stigter, E. E., Steiner, J. F., Koch, I., Saloranta, T. M., Kirkham, J. D., & Immerzeel, W. W. (2021). Energy and mass balance dynamics of the seasonal snowpack at two high-altitude sites in the Himalaya. *Cold Regions Science and Technology*, *183*, 103233. https://doi.org/10.1016/j.coldregions.2021.103233

Strasser, U., Warscher, M., & Liston, G. E. (2011). *Modeling Snow–Canopy Processes on an Idealized Mountain*. https://doi.org/10.1175/2011JHM1344.1

Sturm, M., Holmgren, J., & Liston, G. E. (1995). A Seasonal Snow Cover Classification System for Local to Global Applications. *Journal of Climate*, *8*(5), 1261–1283. https://doi.org/10.1175/1520-0442(1995)008%253C1261:ASSCCS%253E2.0.CO;2

Sturm, M., & Liston, G. E. (2021). Revisiting the Global Seasonal Snow Classification: An Updated Dataset for Earth System Applications. *Journal of Hydrometeorology*, *22*(11), 2917–2938. https://doi.org/10.1175/JHM-D-21-0070.1

Sturm, M., & Wagner, A. M. (2010). Using repeated patterns in snow distribution modeling: An Arctic example. *Water Resources Research*, *46*(12). https://doi.org/10.1029/2010WR009434

Tang, Z., Deng, G., Hu, G., Zhang, H., Pan, H., & Sang, G. (2022). Satellite observed spatiotemporal variability of snow cover and snow phenology over high mountain Asia from 2002 to 2021. *Journal of Hydrology*, *613*, 128438. https://doi.org/10.1016/j.jhydrol.2022.128438

Tarricone, J., Webb, R. W., Marshall, H.-P., Nolin, A. W., & Meyer, F. J. (2023). Estimating snow accumulation and ablation with L-band interferometric synthetic aperture radar (InSAR). *The Cryosphere*, *17*(5), 1997–2019. https://doi.org/10.5194/tc-17-1997-2023

Tedesco, M., Brodzik, M., Armstrong, R., Savoie, M., & Ramage, J. (2009). Pan arctic terrestrial snowmelt trends (1979–2008) from spaceborne passive microwave data and correlation with the Arctic Oscillation. *Geophysical Research Letters*, *36*(21). https://doi.org/10.1029/2009GL039672

Theobald, D. M., Harrison-Atlas, D., Monahan, W. B., & Albano, C. M. (2015). Ecologically-Relevant Maps of Landforms and Physiographic Diversity for Climate Adaptation Planning. *PLOS ONE*, *10*(12), e0143619. https://doi.org/10.1371/journal.pone.0143619

Tomaszewska, M. A., & Henebry, G. M. (2018). Changing snow seasonality in the highlands of Kyrgyzstan. *Environmental Research Letters*, *13*(6), 065006. https://doi.org/10.1088/1748-9326/aabd6f

Tsai, Y.-L. S., Dietz, A., Oppelt, N., & Kuenzer, C. (2019). Remote Sensing of Snow Cover Using Spaceborne SAR: A Review. *Remote Sensing*, *11*(12), Article 12. https://doi.org/10.3390/rs11121456

U.S. Environmental Protection Agency. (2024). *Technical Documentation: Snowpack*. U.S. Environmental Protection Agency (EPA). https://www.wcc.nrcs.usda.gov/snow/index.html

US EPA, O. (2021, November 22). *Seasonality and Climate Change* [Reports and Assessments]. https://www.epa.gov/climate-indicators/seasonality-and-climate-change

USDA Natural Resources Conservation Service. (2022). *SNOwpack TELemetry Network (SNOTEL)* [Dataset]. https://data.nal.usda.gov/dataset/snowpack-telemetry-network-snotel

Van Tiel, M., Van Loon, A. F., Seibert, J., & Stahl, K. (2021). Hydrological response to warm and dry weather: Do glaciers compensate? *Hydrology and Earth System Sciences*, *25*(6), 3245–3265. https://doi.org/10.5194/hess-25-3245-2021

Vicente-Serrano, S. M., Grippa, M., Le Toan, T., & Mognard, N. (2007). Role of atmospheric circulation with respect to the interannual variability in the date of snow cover disappearance over northern latitudes between 1988 and 2003. *Journal of Geophysical Research: Atmospheres*, *112*(D8). https://doi.org/10.1029/2005JD006571

Vuille, M., & Baumgartner, M. F. (1998). Monitoring the regional and temporal variability of winter snowfall in the arid Andes using digital NOAA/AVHRR data. *Geocarto International*. https://doi.org/10.1080/10106049809354629

Warren, S. G. (1982). Optical properties of snow. *Reviews of Geophysics*, *20*(1), 67–89. https://doi.org/10.1029/RG020i001p00067

Webb, R. W., Fassnacht, S. R., & Gooseff, M. N. (2017). Defining the Diurnal Pattern of Snowmelt Using a Beta Distribution Function. *JAWRA Journal of the American Water Resources Association*, *53*(3), 684–696. https://doi.org/10.1111/1752-1688.12522

Wrzesien, M. L., Pavelsky, T. M., Durand, M. T., Dozier, J., & Lundquist, J. D. (2019). Characterizing Biases in Mountain Snow Accumulation From Global Data Sets. *Water Resources Research*, *55*(11), 9873–9891. https://doi.org/10.1029/2019WR025350

Yamaguchi, S., Sato, A., & Lehning, M. (2004). Application of the numerical snowpack model (SNOWPACK) to the wet-snow region in Japan. *Annals of Glaciology*, *38*, 266–272. https://doi.org/10.3189/172756404781815239

Yang, T., Li, Q., Zou, Q., Hamdi, R., Cui, F., & Li, L. (2022). Impact of Snowpack on the Land Surface Phenology in the Tianshan Mountains, Central Asia. *Remote Sensing*, *14*(14), Article 14. https://doi.org/10.3390/rs14143462

Yang, Z., Chen, R., Liu, Y., Zhao, Y., Liu, Z., & Liu, J. (2023). The impact of rain-on-snow events on the snowmelt process: A field study. *Hydrological Processes*, *37*(11), e15019. https://doi.org/10.1002/hyp.15019

Zanaga, D., Van De Kerchove, R., De Keersmaecker, W., Souverijns, N., Brockmann, C., Quast, R., Wevers, J., Grosu, A., Paccini, A., Vergnaud, S., Cartus, O., Santoro, M., Fritz, S., Georgieva, I., Lesiv, M., Carter, S., Herold, M., Li, L., Tsendbazar, N.-E., … Arino, O. (2021). *ESA WorldCover 10 m 2020 v100* (Version v100) [Dataset]. Zenodo. https://doi.org/10.5281/zenodo.5571936

Zhang, T., Stamnes, K., & Bowling, S. A. (1996). *Impact of Clouds on Surface Radiative Fluxes and Snowmelt in the Arctic and Subarctic*. https://journals.ametsoc.org/view/journals/clim/9/9/1520-0442_1996_009_2110_iocosr_2_0_co_2.xml

Zhang, T., Stamnes, K., & Bowling, S. A. (2001). *Impact of the Atmospheric Thickness on the Atmospheric Downwelling Longwave Radiation and Snowmelt under Clear-Sky Conditions in the Arctic and Subarctic*. https://journals.ametsoc.org/view/journals/clim/14/5/1520-0442_2001_014_0920_iotato_2.0.co_2.xml

Zheng, L., Cheng, X., Chen, Z., Wang, S., Liang, Q., & Wang, K. (2022). Global Snowmelt Onset Reflects Climate Variability: Insights from Spaceborne Radiometer Observations. *Journal of Climate*, *35*(10), 2945–2959. https://doi.org/10.1175/JCLI-D-21-0265.1

Zhu, F., Zhu, M., Yang, W., Wang, Z., Guo, Y., & Yao, T. (2024). Drivers of the Extreme Early Spring Glacier Melt of 2022 on the Central Tibetan Plateau. *Earth and Space Science*, *11*(6), e2023EA003297. https://doi.org/10.1029/2023EA003297

APPENDIX A

Supporting Information for "Capturing the onset of mountain snowmelt runoff using satellite synthetic aperture radar"

This document includes supporting figures A.1 to A.9 and supporting table A.1.

Table A.2. Summary of snowmelt runoff onset analysis for stratovolcanoes in the Cascade Range.

2015-2022 Median Runoff Onset Map vs. Terrain Characteristics					
Geography			Correlation Strength		Regression
Stratovolcano	Latitude (°N)	Summit Elevation [m]	with Elevation	with DAH	For every 100m of elevation gain, the average runoff onset day is predicted X days later
Mt. Baker, WA	48.78	3,286	0.89	0.15	6.04
Glacier Peak, WA	48.11	3,213	0.82	0.22	5.80
Mt. Rainier, WA	46.85	4,392	0.88	0.16	4.65
Mt. Adams, WA	46.20	3,740	0.84	0.21	5.18
Mt. St. Helens, WA	46.19	2,549	0.81	0.05	4.27
Mt. Hood, OR	45.37	3,426	0.80	0.12	5.91
Mt. Jefferson, OR	44.67	3,199	0.71	0.23	5.80
Three Sisters, OR	44.15	3,157	0.60	0.22	4.27
Mt. Shasta, CA	41.41	4,317	0.80	0.29	4.32
Lassen Peak, CA	40.49	3,187	0.42	0.45	2.53

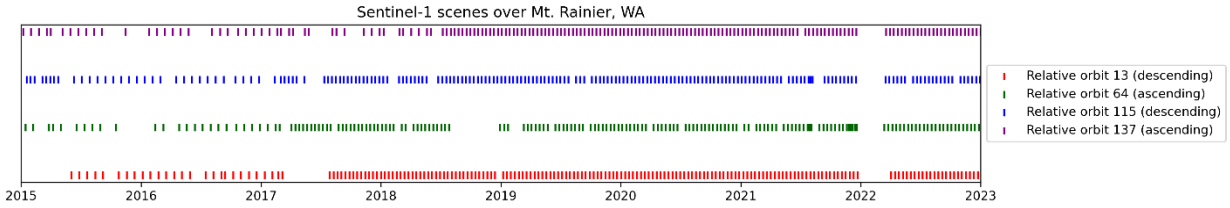

Figure A.1. Timing of Sentinel-1 relative orbits over Mt. Rainier site.

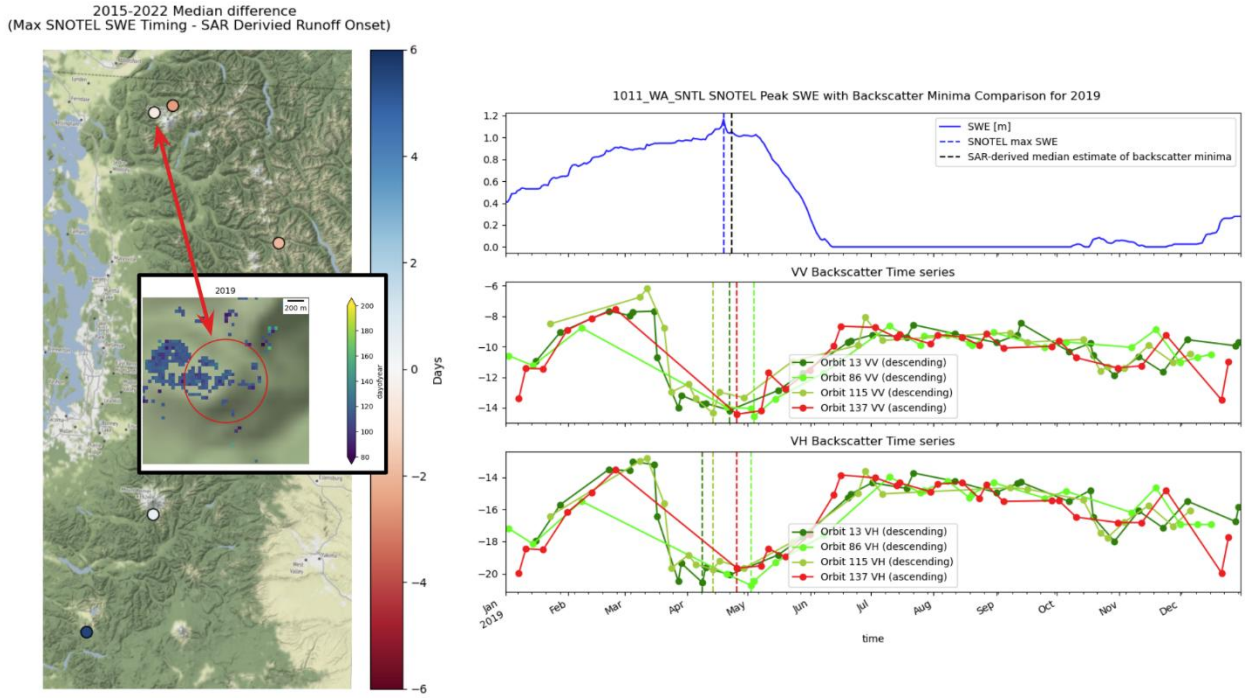

Figure A.2. Comparison between in-situ SNOTEL and SAR derived snowmelt runoff onset measurements. Map on the left shows the median difference in days between timing of maximum daily SWE and the SAR-derived runoff onset for SNOTEL sites with viable coverage during the 2015 to 2022 period. The top right time series plot shows daily SWE measurements for a SNOTEL site near Mt. Baker (MF Nooksack 1011, elevation ~341 m) in 2019. Vertical dashed lines show the timing of maximum SWE (blue) and SAR-derived runoff onset (black) within a 500 meter buffer around the SNOTEL site (red outline on map inset). The middle and lower time series plots show individual runoff onset estimates from each relative orbit and polarization, with vertical dashed lines indicating timing of associated minimum backscatter.

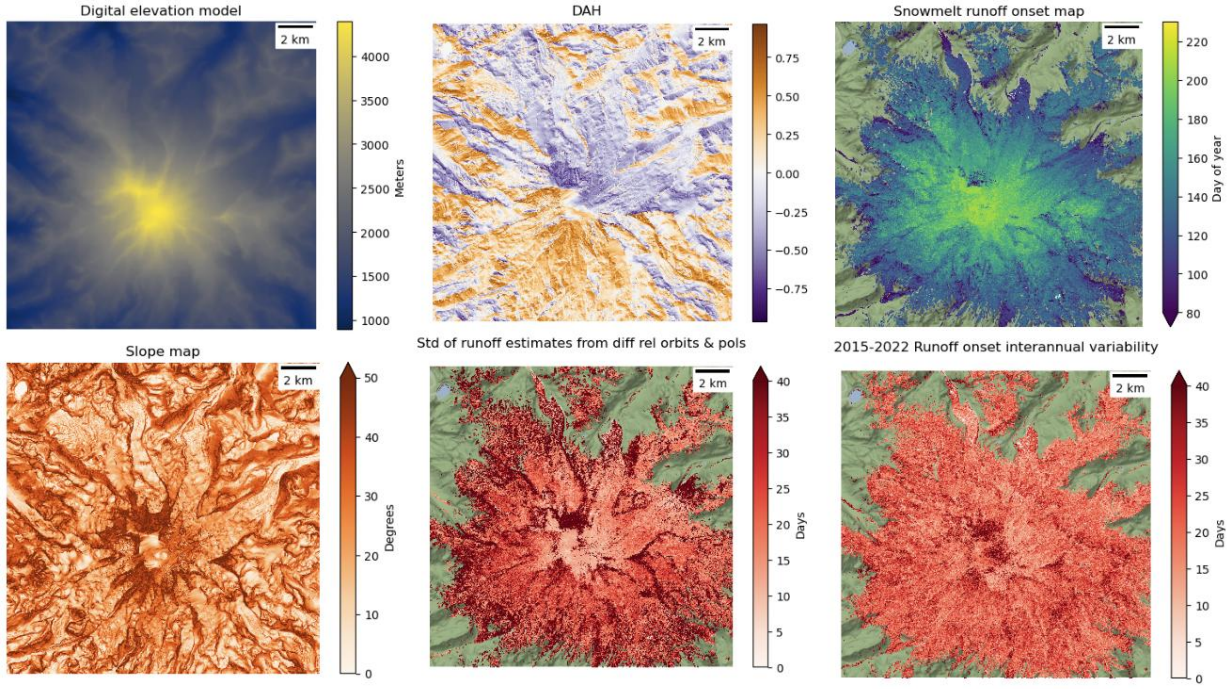

Figure A.3. Raster products for Mt. Rainier site. Top row shows digital elevation model (DEM), diurnal anisotropic heating index (DAH), and 8-year median snowmelt runoff onset map. The DAH map is calculated using $\mathrm{DAH} = \cos(\alpha_{\max} - \alpha) * \arctan(\beta)$, where α_{max} is 202.5° (the aspect experiencing the most diurnal heating), α is the aspect map, and β is the slope map (Böhner & Antonić, 2009). Bottom row shows surface slope, per-pixel standard deviation of runoff onset estimates from all available relative orbits and polarizations during the 2021 season, and the interannual variability in runoff onset during the 2015–2022 period.

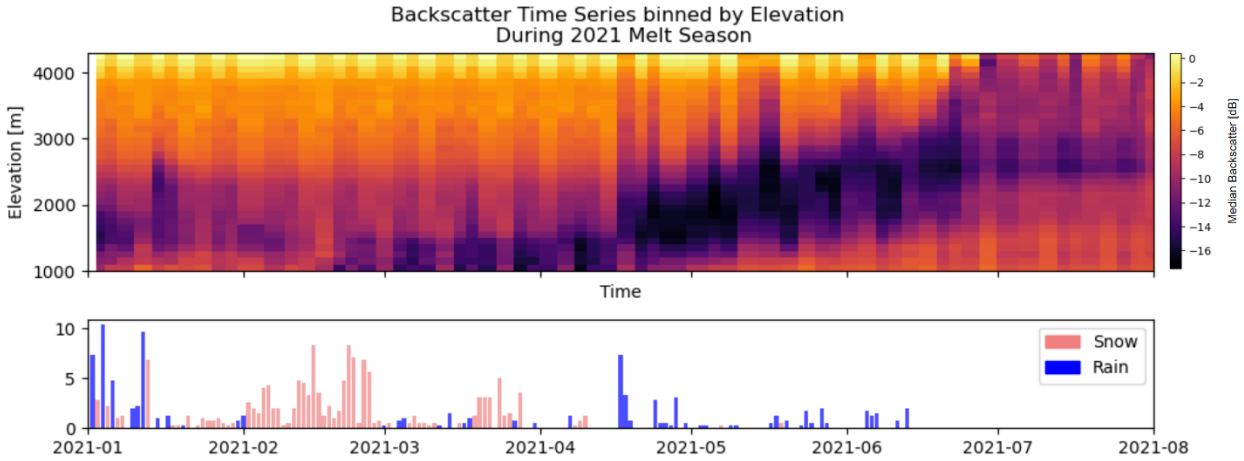

Figure A.4. Top row) Detailed RTC SAR backscatter time series for Mt. Rainier from January through August 2021. Bottom row) Precipitation recorded at Paradise SNOTEL station located at ~1563 m elevation (pink for snow, blue for rain, partitioned using SNOTEL daily average temperature with a threshold of 0°C). Note instances of rain-on-snow events, such as the multi-day precipitation event in mid-April (red box), with corresponding decrease in backscatter across all elevations, indicating snowpack saturation.

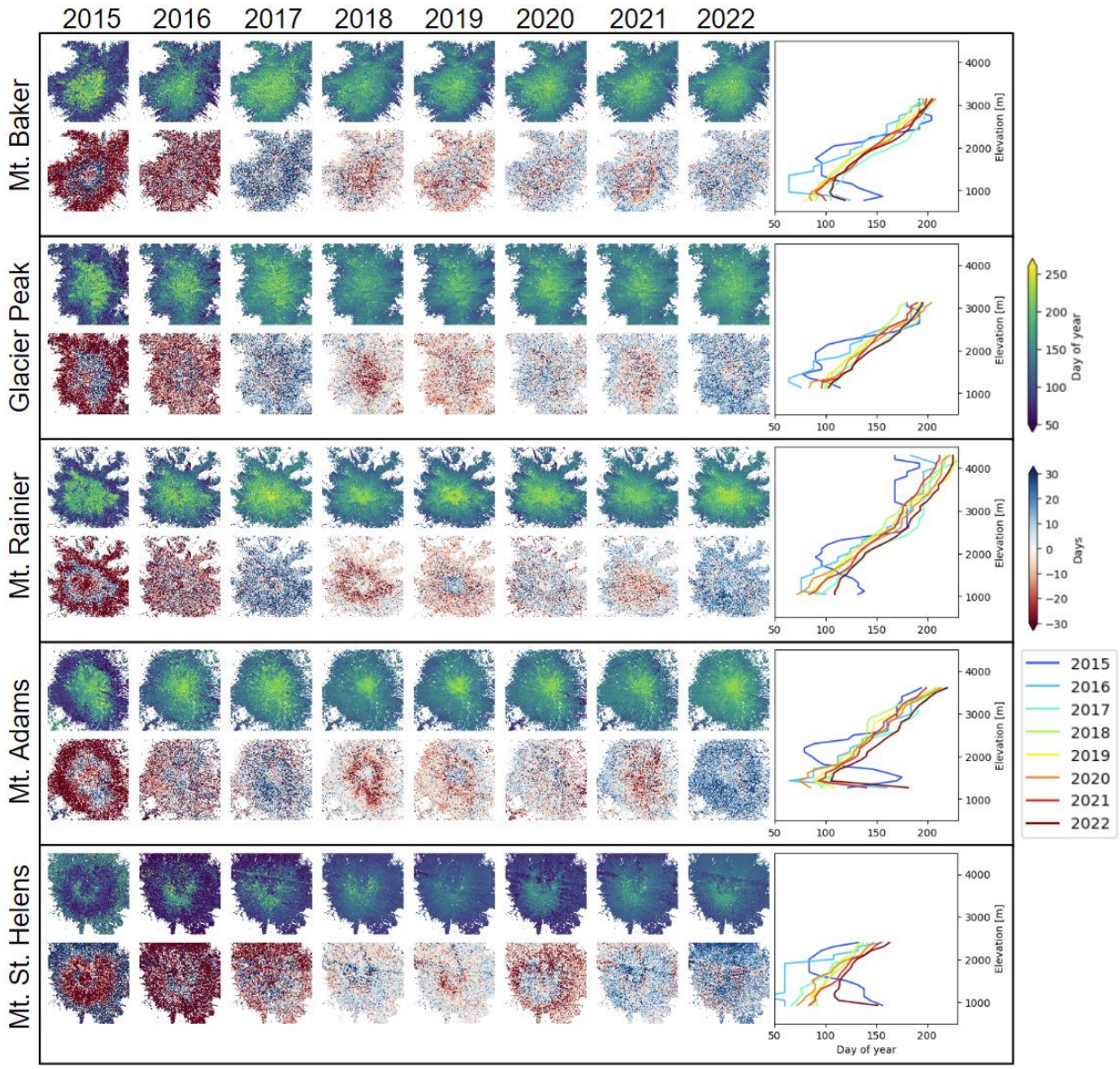
2015
2016
2017
2018
2019
2020
2021
2022
Mt. Baker
Glacier Peak
Mt. Rainier
Mt. Adams
Mt. St. Helens
Elevation [m]
Day of year
Days
2015
2016
2017
2018
2019
2020
2021
2022

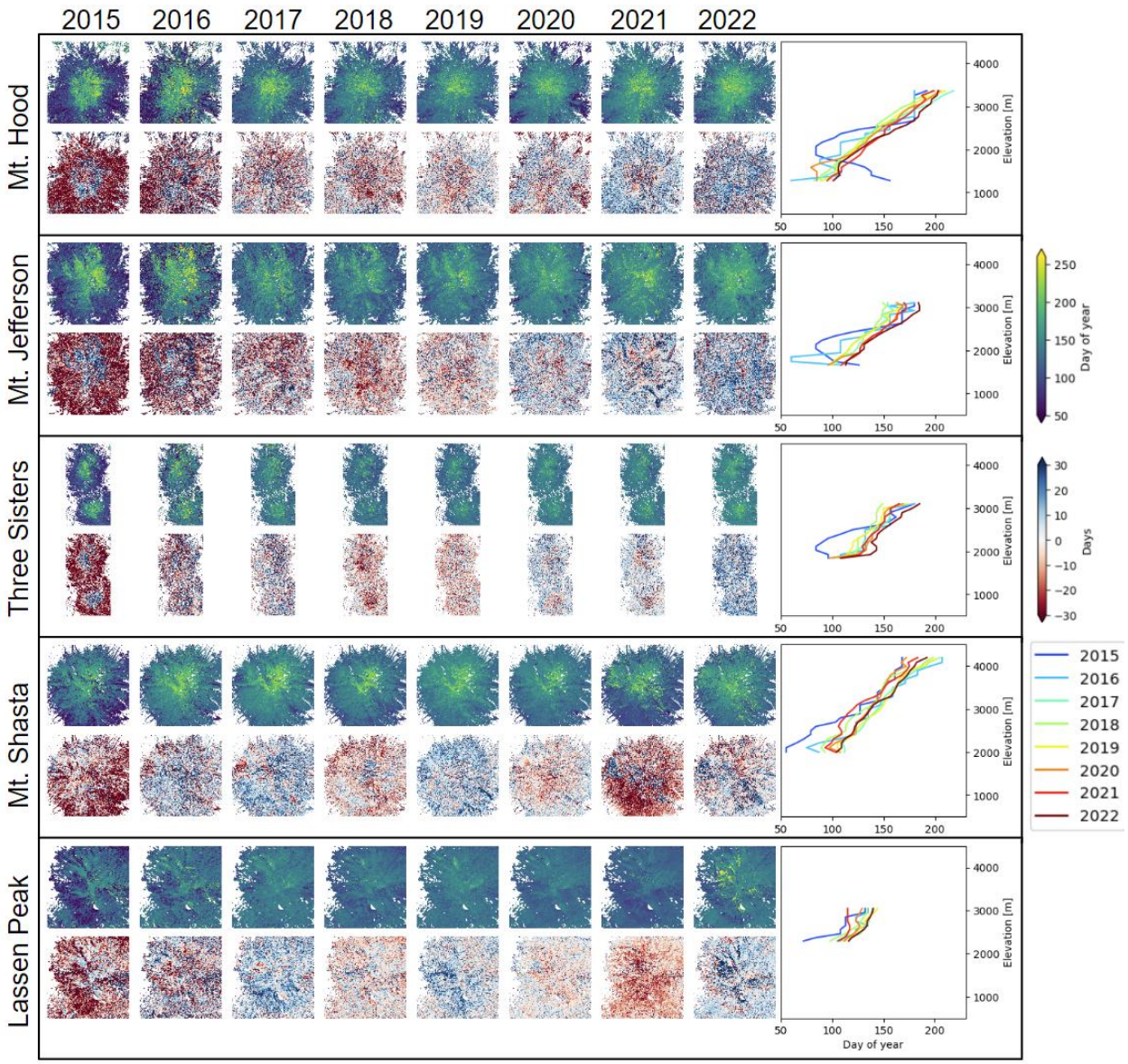

Figure A.5. Annual snowmelt runoff onset maps, snowmelt runoff onset anomaly maps, and annual snowmelt runoff onset vs elevation profiles for all Cascade stratovolcano study sites (see Figure 3B for context map).

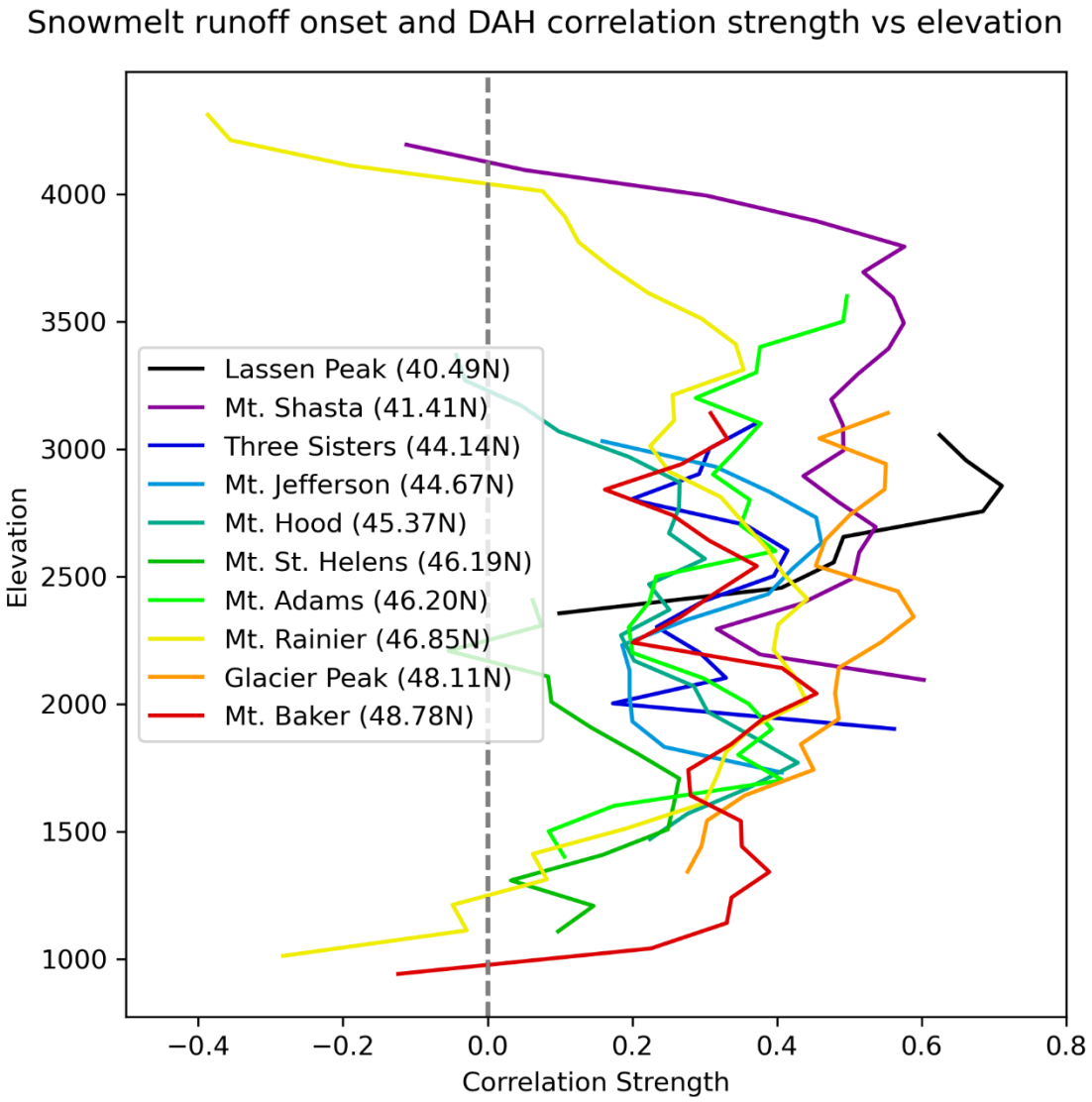

Figure A.6. Correlation strength between snowmelt runoff onset and DAH binned by elevation. Note greater DAH control at mid to high elevations (~2000-3000 m) compared to lower elevations. The upper elevation bins of many stratovolcanoes have lower correlation coefficients, which is consistent with limited DAH ranges at these elevations (e.g., relatively flat or dome-like summits).

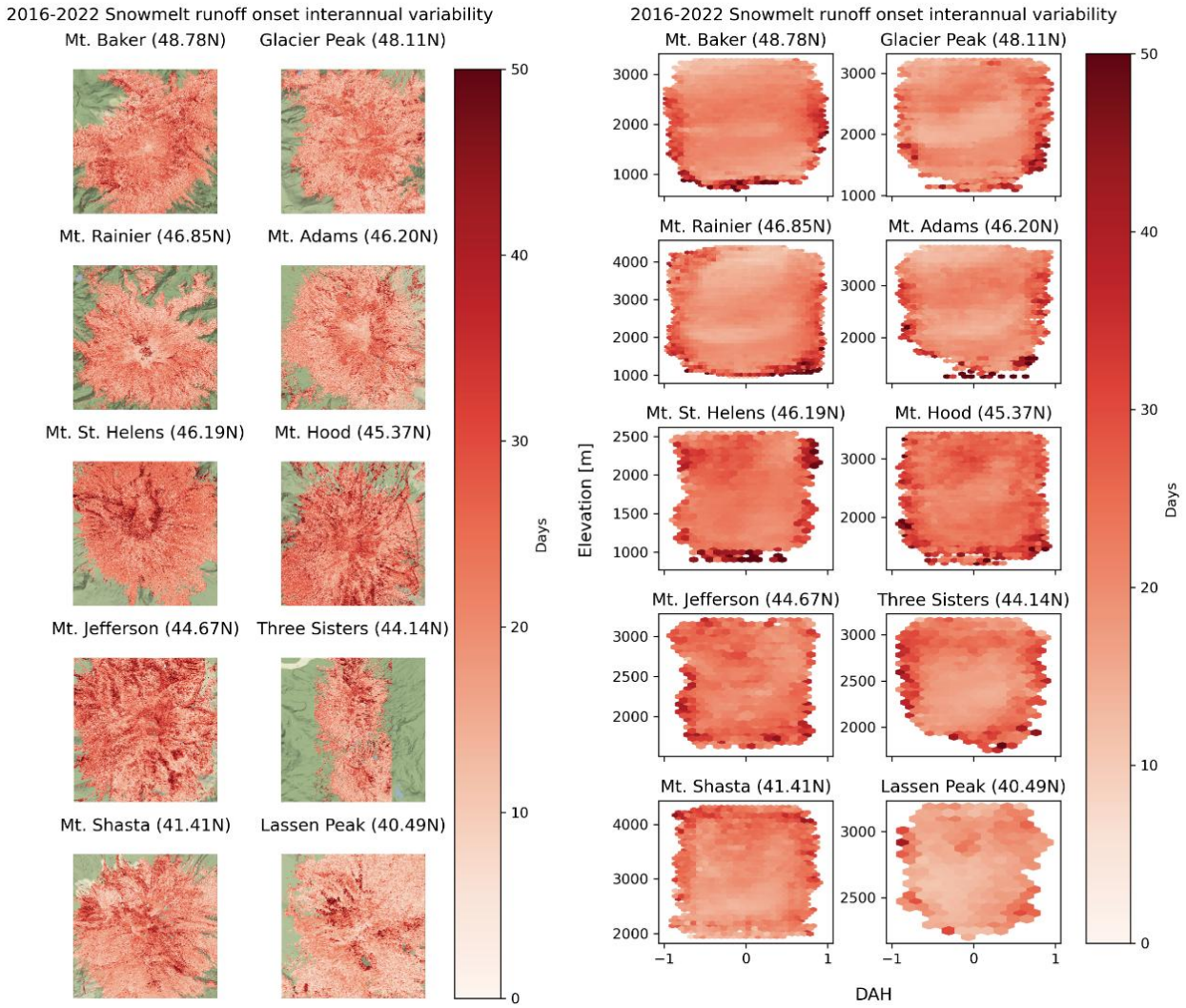

Figure A.7. Left) 2016-2022 snowmelt runoff onset interannual variability, showing the standard deviation of the annual runoff onset maps. Right) Accompanying 2D histograms showing the median of standard deviation values for each elevation and DAH bin. Aside from some limited variability over steep terrain, distribution of standard deviation values is relatively uniform.

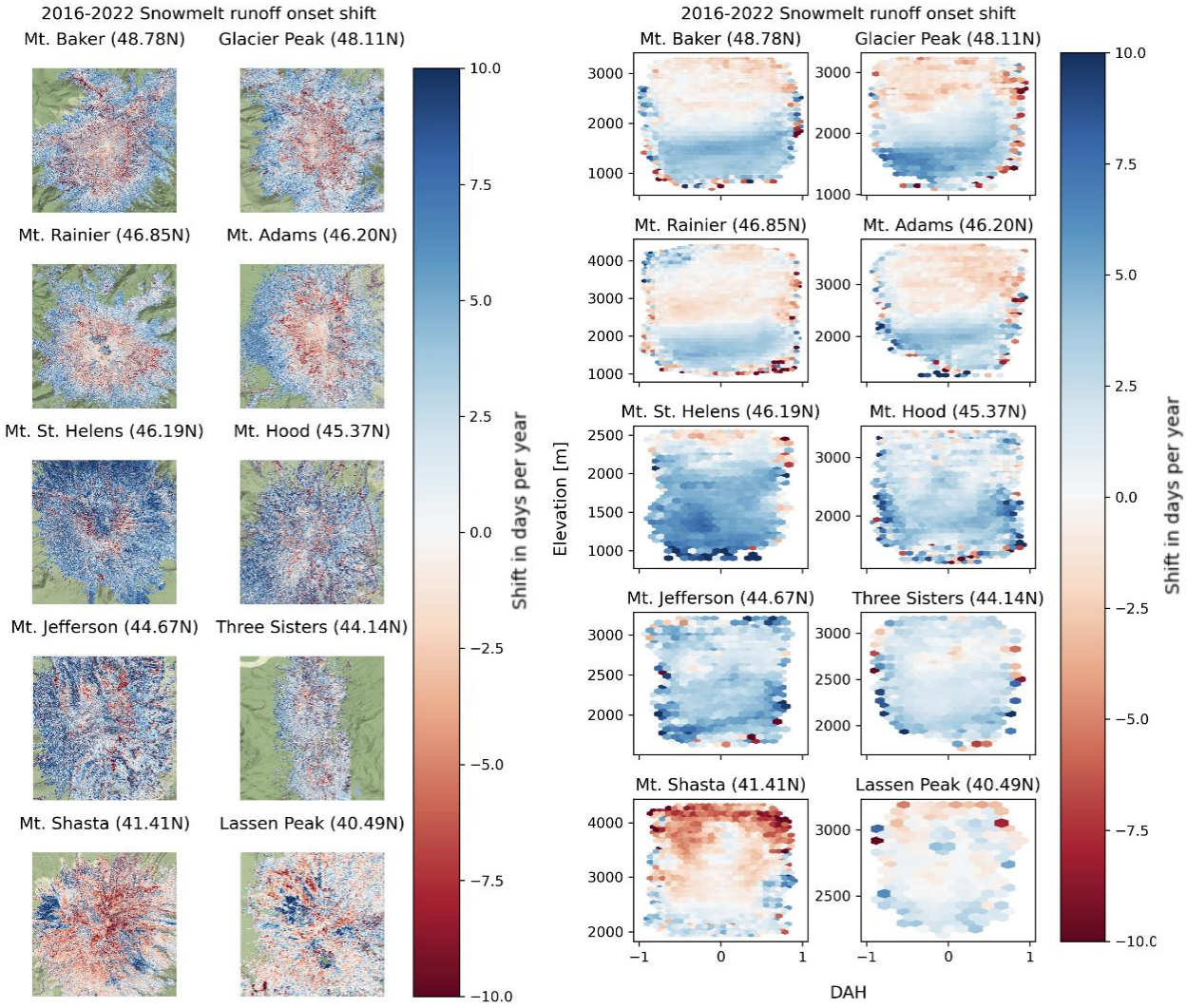

Figure A.8. Left) Snowmelt runoff onset shift (days) over the 2016-2022 period from linear regression analysis. Maps capture spatial variability in apparent short term trends, with negative values (red) indicating an earlier runoff onset, and positive values (blue) indicating a later runoff onset. Right) Accompanying 2D histograms showing the median shift for each elevation and DAH bin.

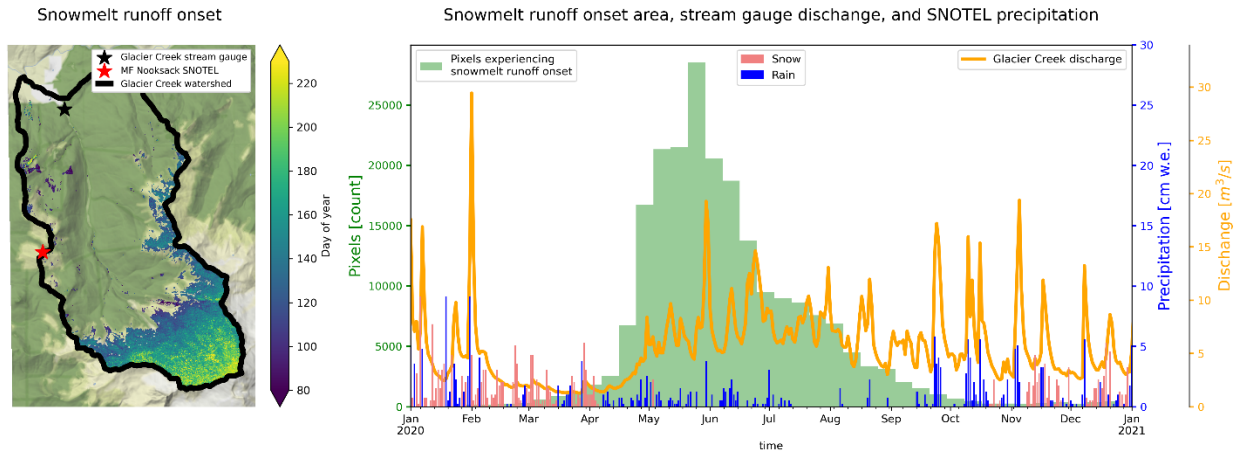

Figure A.9. Left) 2020 annual snowmelt runoff onset map cropped to the unregulated Glacier Creek watershed on the northwest side of Mt. Baker. The USGS Glacier Creek stream gauge (#12205245, elevation ~341 m) and MF Nooksack SNOTEL site (elevation ~1515 m) are shown with a black and red star, respectively. Right) Histogram of 2020 annual snowmelt runoff onset map dates (green), stream gauge discharge (U. S. Geological Survey, 1994), and precipitation (with approximate classification as either rain or snow using SNOTEL daily average temperature with a threshold of 0°C) for the MF Nooksack SNOTEL site. In general, we see elevated discharge during the spring and summer, when our annual snowmelt runoff onset maps indicate the greatest number of pixels are at their backscatter minima. There is an apparent lag between upper basin snowmelt runoff onset and stream gauge discharge, but establishing a direct relationship is challenging for this watershed due to frequent precipitation events, large elevation gradients, unknown subsurface conditions, and the large percentage of the watershed with dense tree cover.

APPENDIX B

Supporting Information for "A global high-resolution dataset of snowmelt runoff onset timing from Sentinel-1 SAR, 2015-2024"

This document includes supporting figures B.1 to B.6.

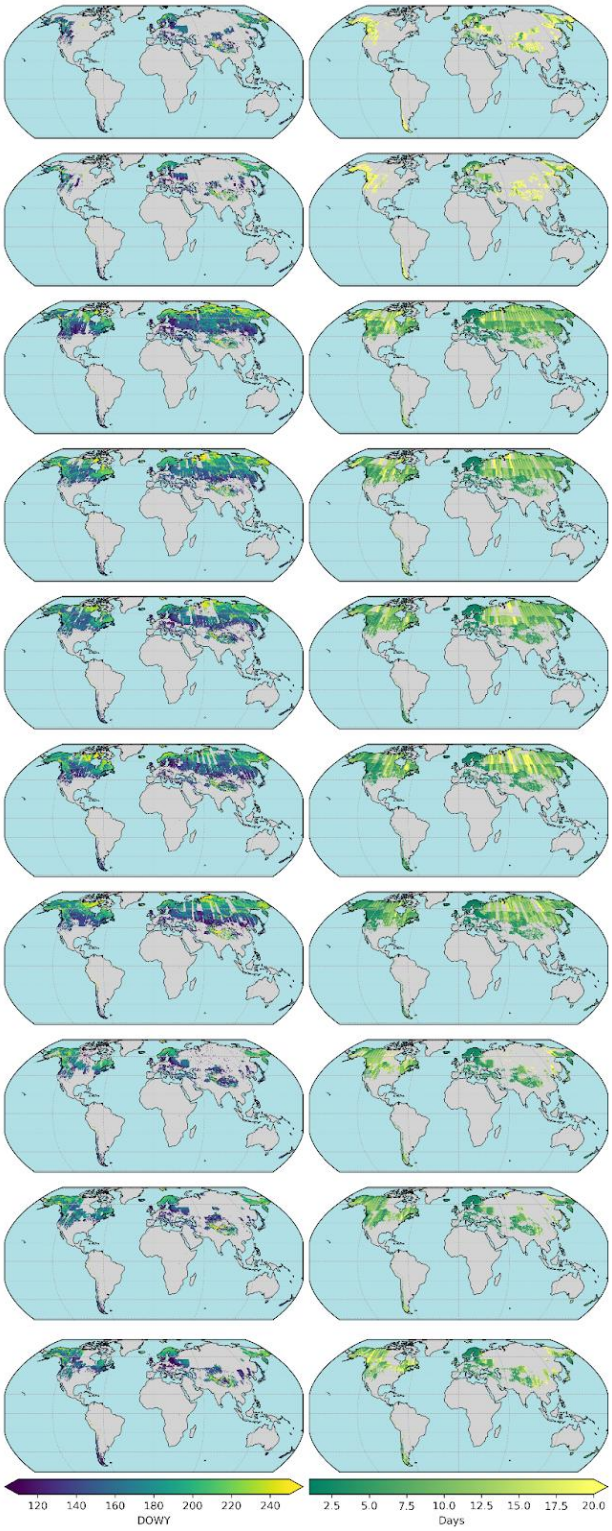

Figure B.1. Snowmelt runoff onset and temporal resolution for each water year.

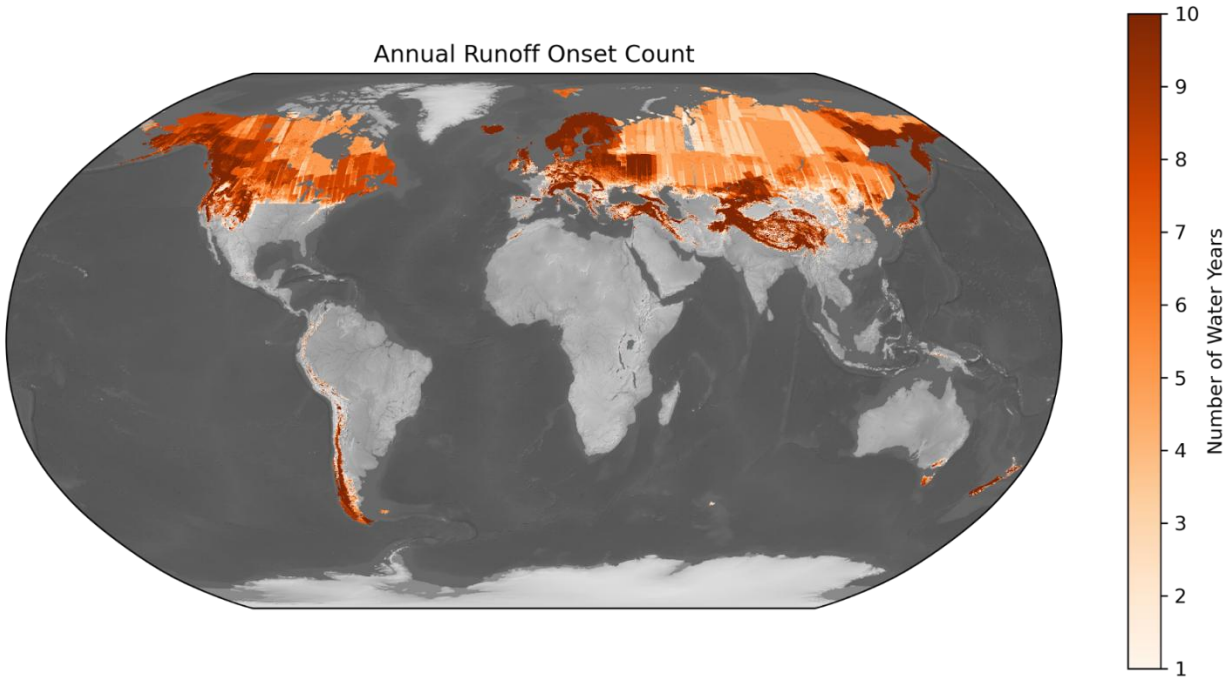

Figure B.2. Per-pixel number of water years with annual runoff onset estimates.

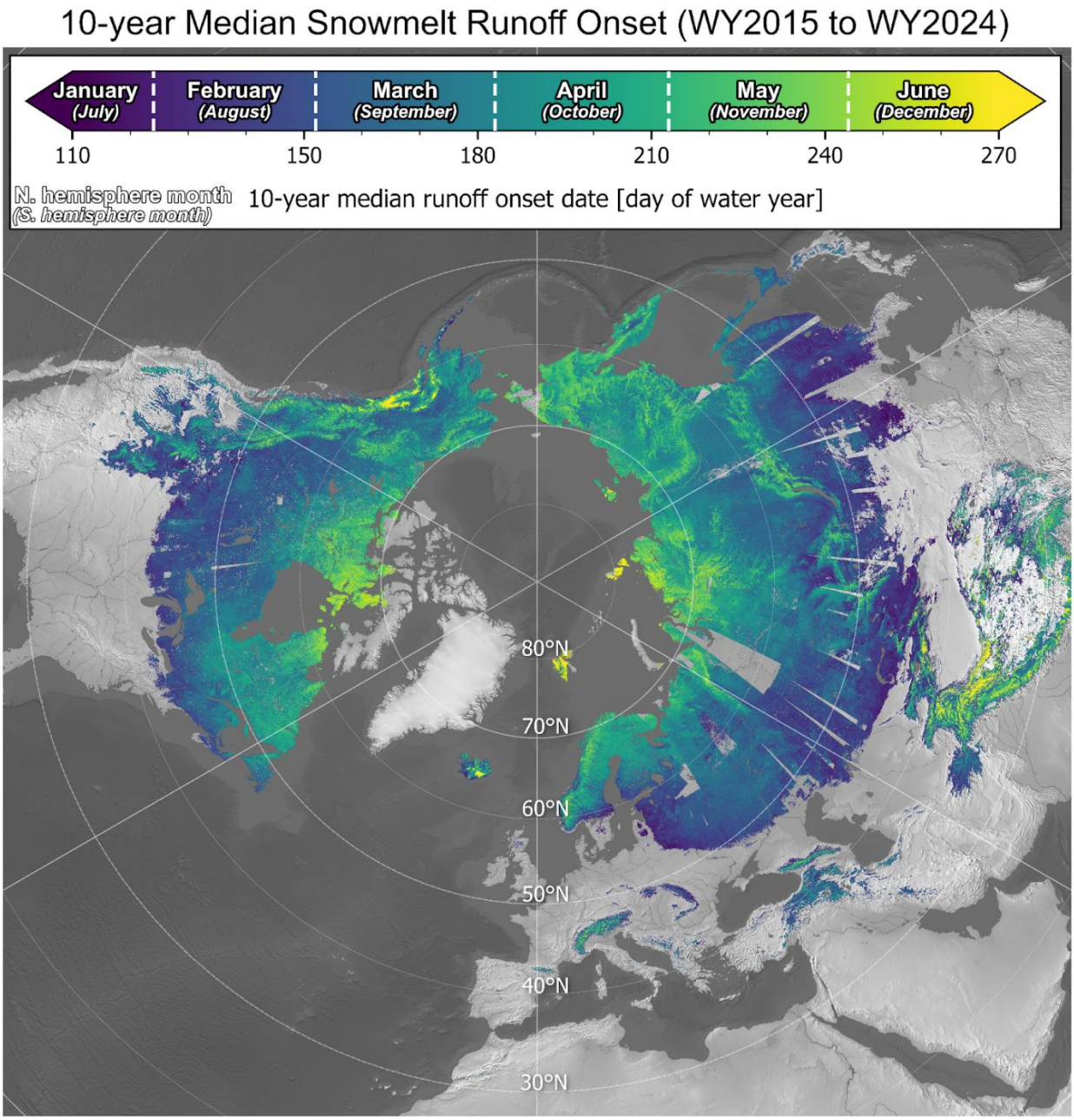

Figure B.3. Polar stereographic projection of 10-year median snowmelt runoff onset date.

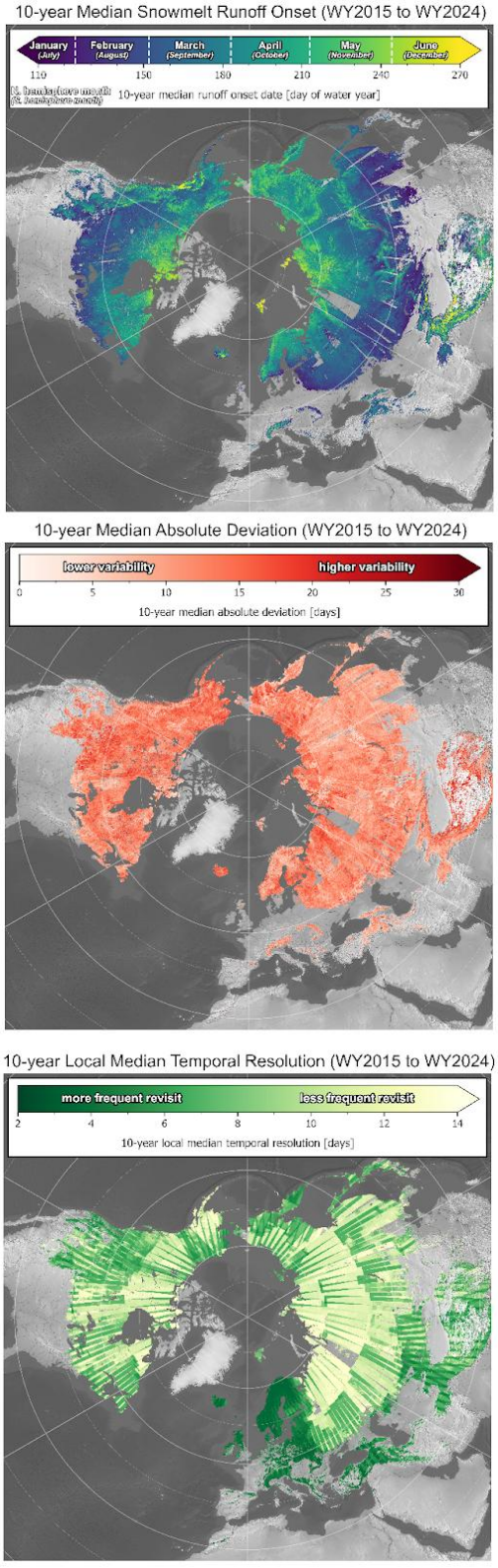

Figure B.4. Polar stereographic version of Figure 3.2.

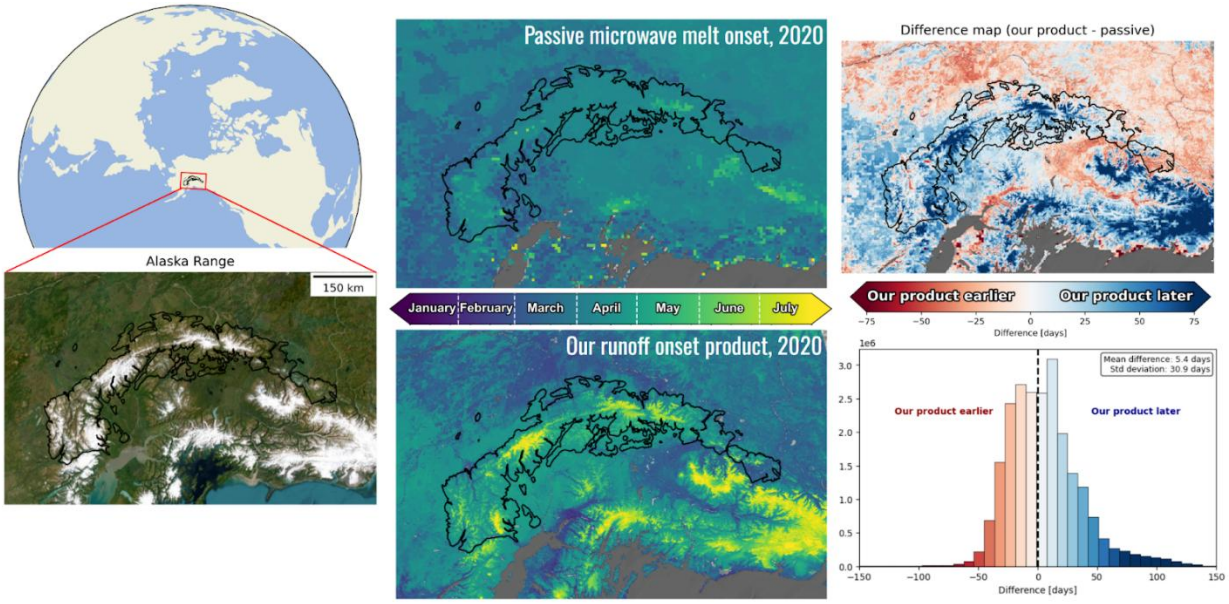

Figure B.5. Annual runoff onset product compared to passive microwave melt onset from (Pan et al., 2021) over the Alaska Range for 2020.

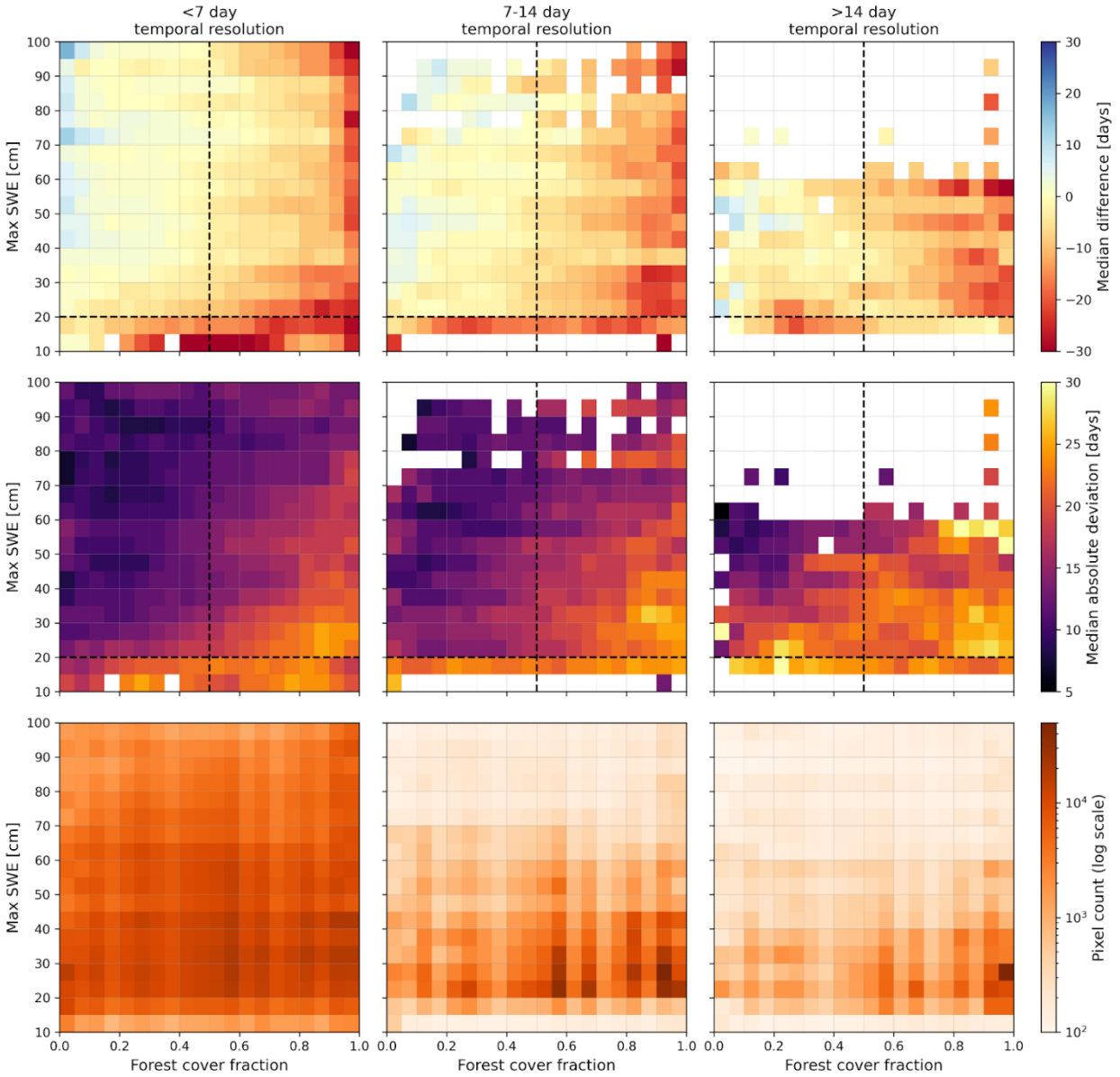

Figure B.6. Figure 3.3 with accompanying pixel count histogram.

VITA

Eric Gagliano grew up in Magnolia, Texas, far from the snow-covered regions of the world. He attended The University of Texas at Austin, receiving his Bachelor of Science in Computational Engineering and a certificate in Humanitarian Engineering in 2020. Despite growing up without snow, his fascination with earth science, the cryosphere, climate change impacts, and remote sensing blossomed at UT Austin, eventually leading him to pursue undergraduate research studying outlet glaciers in Greenland using satellite radar under the guidance of Dr. Ann Chen.

Alongside his research interests, Eric knew early on he wanted to become an educator. At UT Austin, he developed and taught STEM curriculum to middle school students through Student Engineers Educating Kids; he volunteered as a reading buddy for elementary school students through Students Expanding Austin Literacy; he worked as an undergraduate teaching assistant for a programming class; and he served as a first-year interest group mentor, mentoring dozens of freshmen over the course of four years.

Eric's interest in research and passion for teaching led him to join the Terrain Analysis and Cryosphere Observation Lab at the University of Washington, where he pursued doctoral studies under the supervision of Dr. David Shean. His research advanced satellite radar remote sensing methods to better understand the spatial and interannual variability of snowmelt timing across the Earth's diverse mountain ranges. At UW, Eric gained extensive teaching and curriculum development experience, serving as a teaching assistant for four classes, and serving as the instructor of the graduate Geospatial Data Analysis in Python class twice. Eric also served as a union steward representing the graduate students of the Department of Civil and Environmental Engineering, organizing with UAW 4121 on behalf of academic student employees.

Beyond his research, Eric has been an active camp counselor with Camp Kesem since 2017, working with children affected by a parent's cancer through both the UT Austin and UW chapters, where he is better known as "boombox". In his free time, Eric enjoys singing in choir, spending time with friends, and eating lots of soft serve ice cream.

Looking forward, Eric is passionate about science education and plans to pursue teaching at the high school level, where he hopes to develop engaging curriculum around earth science, climate change, remote sensing, and environmental justice.